Time-dependent diffusion MRI with free gradient waveforms: From theory development to initial applications

Chakwizira, Arthur

2025

Time-dependent diffusion MRI with free gradient waveforms

From theory development to initial applications

ARTHUR CHAKWIZIRA
MEDICAL RADIATION PHYSICS, LUND | FACULTY OF SCIENCE | LUND UNIVERSITY

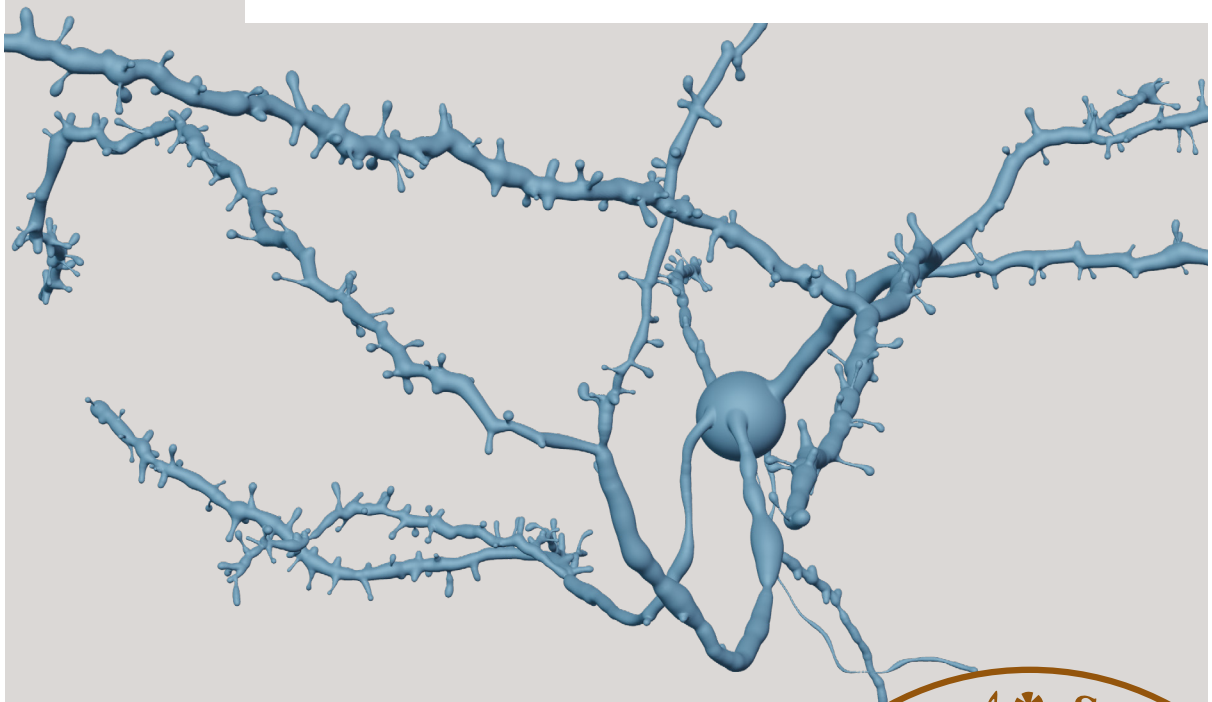

Printed by Media-Tryck, Lund 2025 NORDIC SWAN ECOLABEL 3041 0903

Time-dependent diffusion MRI with free gradient waveforms

From theory development to initial applications

Diffusion MRI is remarkably sensitive to tissue microstructure but generally lacks specificity. This thesis presents advanced time-dependent diffusion MRI techniques using free gradient waveforms to address this limitation and enable more reliable estimation of microstructural parameters—particularly water exchange. The methods developed here separate exchange from the effects of restricted diffusion, anisotropy, and intra-compartmental kurtosis. Initial applications in intracranial tumours demonstrate potential for clinical use. This work also opens exciting avenues for *in vivo* mapping of dendritic spine density using diffusion MRI—a development with significant implications for neuroscience, especially in the context of neurodegenerative and neuropsychiatric disorders. This thesis is timely, given the growing availability of high-performance MRI scanners from which the methods developed herein will greatly benefit.

ARTHUR CHAKWIZIRA is a licensed medical physicist who received his B.Sc. in Physics (2017) and M.Sc. in Medical Radiation Physics (2020) from Lund University.

Faculty of Science
Department of Medical Radiation Physics, Lund

ISBN 978-91-8104-447-8

Time-dependent diffusion MRI with free gradient waveforms

From theory development to initial applications

Time-dependent diffusion MRI with free gradient waveforms

From theory development to initial applications

Arthur Chakwizira

LUND
UNIVERSITY

DOCTORAL DISSERTATION

Doctoral dissertation for the degree of Doctor of Philosophy (PhD) at the Faculty of Science at Lund University to be publicly defended on 23 May 2025 at 09.00 in Belfragesalen, Biomedical Centre, Sölvegatan 19, 223 62 Lund.

Faculty opponent
Dr. Sune Jespersen, Department of Clinical Medicine; Department of Physics and Astronomy, Aarhus University, Aarhus, Denmark

Organization: LUND UNIVERSITY Department of Medical Radiation Physics Clinical Sciences, Lund Faculty of Science	**Document name:** DOCTORAL DISSERTATION **Date of disputation** 23 May 2025
Author: Arthur Chakwizira	**Sponsoring organization:**

Title and subtitle:

Time-dependent diffusion MRI with free gradient waveforms: From theory development to initial applications

Abstract:

Diffusion magnetic resonance imaging (dMRI) is a powerful non-invasive technique for probing tissue microstructure. While highly sensitive, conventional dMRI methods suffer from low specificity, due in part to experimental designs that conflate multiple contrast mechanisms. This thesis aims to address these limitations by developing advanced time-dependent dMRI techniques to disentangle competing sources of contrast—specifically restricted diffusion, intercompartmental exchange, anisotropy, and intra-compartmental kurtosis.

In Paper I, we developed a theoretical framework and experimental design using free gradient waveforms, termed Restriction-Exchange (ResEx), to disentangle restricted diffusion from exchange, and validated the approach using Monte Carlo simulations. In Paper II, we applied ResEx in the healthy human brain on a high-performance scanner (300 mT/m), and isolated distinct exchange- and restriction-driven signal contrasts. Furthermore, in Paper VI, we applied the ResEx framework in gliomas on a clinical scanner (80 mT/m) and observed substantial and spatially heterogeneous exchange-driven contrasts in tumour tissue, with potential implications for non-invasive tumour characterisation. Additionally, in Paper III, we used the framework to correct crusher gradient-induced bias in filter exchange imaging (FEXI), enabling more accurate estimation of the apparent exchange rate (AXR).

To enhance specificity further, we also developed a tensor-valued encoding approach in Paper IV to enable measurement of exchange in the presence of anisotropy and intra-compartmental kurtosis, using variable-mixing-time double diffusion encoding acquisitions.

Finally, in Paper V, we studied the interplay between dendritic spine-driven geometric exchange and permeative exchange in simulations, and used the framework from Paper IV to separate the two, offering a potential route for mapping spine density *in vivo* with dMRI.

Together, these contributions establish a set of theoretical and experimental tools to improve the specificity and interpretability of dMRI. They position advanced diffusion encoding—particularly when combined with ultra-strong gradient systems—as a promising avenue for non-invasive microstructure imaging in both clinical and research settings.

Key words:

Classification system and/or index terms (if any)

Supplementary bibliographical information	**Language:** English
ISSN and key title:	**ISBN:** 978-91-8104-447-8 (print) 978-91-8104-448-5 (electronic)
Recipient's notes	**Number of pages**: 98 / Price
	Security classification

Signature Date 2025-04-08

Time-dependent diffusion MRI with free gradient waveforms

From theory development to initial applications

Arthur Chakwizira

LUND
UNIVERSITY

Lund University

Faculty of Science

Department of Medical Radiation Physics, Lund

ISBN: 978-91-8104-447-8 (print)
978-91-8104-448-5 (electronic)

Printed in Sweden by Media-Tryck, Lund University

Lund 2025

Media-Tryck is a Nordic Swan Ecolabel certified provider of printed material. Read more about our environmental work at www.mediatryck.lu.se

MADE IN SWEDEN

For Amanda, Alicia and Alex Michael

Table of Contents

Populärvetenskaplig sammanfattning

Diffusions-magnetresonanstomografi (dMRI) är en kraftfull bildgivande teknik som är mycket känslig för mikroskopiska förändringar i vävnaden och kan upptäcka sjukdomar som stroke i ett mycket tidigt skede. Känsligheten kommer från att tekniken använder extremt starka magnetfält för att följa vattenmolekylers rörelser på mikroskopisk nivå. Trots denna höga känslighet är metoden tyvärr ganska ospecifik, vilket innebär att flera olika förändringar i vävnaden kan ge upphov till samma signal i dMRI-bilden. Det gör tolkningen svår och begränsar metodens diagnostiska potential, eftersom olika sjukdomstillstånd kan vara svåra att särskilja.

Denna avhandling syftar till att lösa detta problem genom att utveckla nya och mer avancerade dMRI-tekniker. De nya metoderna bygger på så kallad "tidsberoende dMRI", där vi istället för att ta en enda bild med en fast mättid, samlar in en serie bilder med varierande mättider. Dessutom använder vi så kallade "fria vågformer", vilket innebär att magnetfälten formas mer flexibelt för att maximera mängden information i varje mätning. För att tolka dessa mer komplexa data utvecklar vi nya teoretiska modeller som kopplar mätningarna till vävnadens mikroskopiska struktur.

Med detta verktyg, som är en kombination av nya mätmetoder och modeller, lyckas vi särskilja olika egenskaper i den friska hjärnan, som till exempel cellstorlek och genomsläpplighet. Dessa har tidigare varit svåra eller omöjliga att separera med traditionella tekniker. Vi tillämpar även våra nya metoder på hjärntumörer där de visar lovande resultat. Metoderna kan potentiellt särskilja både olika typer av tumörer och olika sjukdomsgrad inom en och samma tumör, vilket kan få betydelse för framtida diagnos och behandling. Avhandlingen visar också att de nya metoderna potentiellt kan användas för att mäta så kallade "dendritiska taggar", vilka är små utskott på nervceller som spelar en viktig roll i hjärnans funktion. Dessa strukturer påverkas vid många hjärnsjukdomar, som schizofreni och Alzheimers, men det finns idag inga pålitliga metoder för att studera dem utan att exponera patienten för joniserande strålning. Att kunna avbilda dendritiska taggar hos levande människor utan att använda joniserande strålning vore ett stort genombrott.

Sammanfattningsvis bidrar avhandlingen med både teoretiska och praktiska verktyg för att göra dMRI till en mer specifik och pålitlig metod. Resultaten pekar på att avancerad dMRI – särskilt i kombination med starka magnetsystem – är ett lovande sätt att studera hjärnans mikrostruktur, både i forskningssammanhang och i sjukvården.

Original papers

This thesis is based on six papers, which will be referred to by Roman numerals.

I. **Chakwizira, A.**, Westin, C.-F., Brabec, J., Lasič, S., Knutsson, L., Szczepankiewicz, F. & Nilsson, M. 2023. Diffusion MRI with pulsed and free gradient waveforms: Effects of restricted diffusion and exchange. NMR in Biomedicine. 36(1): e4827.

II. **Chakwizira, A.,** Zhu, A., Foo, T., Westin, C.-F., Szczepankiewicz, F. & Nilsson, M. 2023. Diffusion MRI with free gradient waveforms on a high-performance gradient system: Probing restriction and exchange in the human brain. NeuroImage. 283: 120409.

III. Lasič, S., **Chakwizira, A.**, Lundell, H., Westin, C.-F. & Nilsson, M. 2024. Tuned exchange imaging: Can the filter exchange imaging pulse sequence be adapted for applications with thin slices and restricted diffusion? NMR in Biomedicine. 37(11): e5208.

IV. **Chakwizira, A.**, Szczepankiewicz, F. & Nilsson, M. 2025. Diffusion MRI with double diffusion encoding and variable mixing times disentangles water exchange from transient kurtosis. Scientific Reports. 15(1): 8747.

V. **Chakwizira, A.,** Şimşek, K., Szczepankiewicz, F., Palombo, M. & Nilsson, M., 2025. The role of dendritic spines in water exchange measurements with diffusion MRI: Double Diffusion Encoding and free-waveform MRI. Manuscript.

VI. **Chakwizira, A.,** Szczepankiewicz, F., Westin, C.-F., Knutsson, L., Sundgren, P. & Nilsson, M., 2025. Characterising Water Exchange in Gliomas Using Diffusion MRI with Free Gradient Waveforms. Manuscript.

List of contributions

My contributions to each of the papers above are summarised below.

I. I participated in the study design and theory development, wrote code for waveform design, built Monte Carlo simulation frameworks for validating the theory, executed the simulations and analysed the data. I interpreted the results alongside the co-authors, and I was the main author of the paper. I presented the results at the ISMRM conference.

II. I took part in the conceptualisation of the study, designed the experiment, collaborated with Ante Zhu during data acquisition, processed and analysed the data. I was the main author of the paper. I presented the results at the ISMRM conference.

III. I designed and executed Monte Carlo simulations and took part in the analysis and interpretation of the data. I contributed to writing the paper and presented the results at the ISMRM conference.

IV. I contributed to the conceptualisation and design of the study as well as theory development. I designed and executed Monte Carlo simulations to validate the theory, and I analysed the data. I interpreted the results with the co-authors, and I was the main author of the paper. I also presented the results at the ISMRM conference.

V. I took part in the conceptualisation and design of the study, designed and executed Monte Carlo simulations for validation and analysed the data. I interpreted the results together with co-authors, and I was the main author of the manuscript. I presented preliminary results from this work at the ISMRM conference.

VI. I designed the experiment, collaborated with clinicians during data acquisition, processed and analysed the data. I interpreted the results together with the co-authors and was the main author of the manuscript.

Papers not included in this thesis

- **Chakwizira, A.,** Ahlstedt, J., Nittby Redebrandt, H. & Ceberg, C. 2018. Mathematical modelling of the synergistic combination of radiotherapy and indoleamine-2,3-dioxygenase (IDO) inhibitory immunotherapy against glioblastoma. The British Journal of Radiology. 91(1087): 20170857.

- **Chakwizira, A.,** Ahlgren, A., Knutsson, L. & Wirestam, R. 2022. Non-parametric deconvolution using Bézier curves for quantification of cerebral perfusion in dynamic susceptibility contrast MRI. Magnetic Resonance Materials in Physics, Biology and Medicine. 35(5): 791–804.

- Wirestam, R., Lundberg, A., **Chakwizira, A**., Westen, D. van, Knutsson, L. & Lind, E. 2022. Test-retest analysis of cerebral oxygen extraction estimates in healthy volunteers: comparison of methods based on quantitative susceptibility mapping and dynamic susceptibility contrast magnetic resonance imaging. Heliyon. 8(12): e12364.

- Wirestam, R., **Chakwizira, A**. & Reinstrup, P. 2025. Evaluation of parameters extracted from tissue residue functions in dynamic susceptibility contrast MRI: Healthy volunteers examined during normal breathing and spontaneous hyperventilation. Heliyon. 11(4): e42521.

Conference abstracts

- **Chakwizira, A.**, Szczepankiewicz, F., Knutsson, L., Sundgren, P., Nilsson, M. 2021. Cumulant expansions for measuring restricted diffusion and water exchange. Proceedings of the ISMRM.
- **Chakwizira, A.**, Szczepankiewicz, F., Knutsson, L., Nilsson, M. 2021. Probing restricted diffusion and water exchange with free gradient waveforms: Addressing the need for a compartment model. Proceedings of the ISMRM.
- **Chakwizira, A.**, Lasič, S., Reymbaut, A., Westin, C-F., Szczepankiewicz, F., Nilsson M. 2022. Characterisation of restricted diffusion and exchange using the velocity autocorrelation function. Proceedings of the ISMRM. London.
- **Chakwizira, A.**, Szczepankiewicz, F., Westin, C-F., Vis, G., Knutsson, L., Sundgren, P., Nilsson, M. 2022. Mapping water exchange in the human brain using diffusion MRI with free waveform encoding. Proceedings of the ISMRM. London.
- **Chakwizira, A.**, Szczepankiewicz, F., Nilsson, M. 2023. Diffusional exchange versus microscopic kurtosis from CTI: Two conflicting interpretations of the same data. Proceedings of the ISMRM. Toronto.
- **Chakwizira, A.**, Zhu, A., Foo, T., Westin, C-F., Szczepankiewicz, F., Nilsson, M. 2023. Probing restriction and exchange in the human brain using free waveforms on a high-performance gradient system. Proceedings of the ISMRM. Toronto.
- Testud, F., **Chakwizira, A.**, Nilsson, M. 2023. Whole Brain Simultaneous MultiSlice Filter Exchange Imaging in less than 15 minutes: Initial Results. Proceedings of the ISMRM. Toronto.
- **Chakwizira, A.**, Şimşek, K., Palombo, M., Szczepankiewicz, F., Knutsson, L., Nilsson, M. 2024. Water exchange as measured by diffusion MRI with free gradient waveforms: A potential biomarker of dendritic spine morphology. Proceedings of the ISMRM. Singapore.
- Nilsson, M., **Chakwizira, A.**, Szczepankiewicz, F., Lasič, S., Westin, C-F. 2024. Unifying b-tensor encoding with compartmental-exchange: A novel analysis framework applied to double diffusion encoding. Proceedings of the ISMRM. Singapore.

Abbreviations

ADC	Apparent Diffusion Coefficient
CTI	Correlation Tensor Imaging
DKI	Diffusion Kurtosis Imaging
dMRI	diffusion Magnetic Resonance Imaging
DTI	Diffusion Tensor Imaging
MRI	Magnetic Resonance Imaging
MGE	Multi-Gaussian Exchange
MSD	Mean Squared Displacement
QTI	Q-space Trajectory Imaging
ResEx	Restriction-Exchange
tMGE	Multi-Gaussian Exchange with transient kurtosis
VAF	Velocity Autocorrelation Function

1 Introduction

Diffusion magnetic resonance imaging (dMRI) is a non-invasive imaging modality that is remarkably sensitive to the microstructure of biological tissue. This sensitivity is achieved by applying spatial magnetic field gradients that encode the random displacements of water molecules at the micrometre scale—far below the millimetre resolution of MRI voxels (Hahn 1950; Torrey 1956; Stejskal and Tanner 1965; Le Bihan et al. 1986; Callaghan 1991; Jones 2010). Conventional dMRI acquires signal as a function of diffusion encoding strength. The initial slope of this signal, known as the apparent diffusion coefficient (ADC), is highly sensitive to microstructural changes such as variations in cell density (Chenevert et al. 2000; Le Bihan 2003; Chen et al. 2013). In anisotropic tissue, diffusion tensor imaging (DTI) (Basser et al. 1994) extends the scalar ADC to a tensor, enabling quantification of anisotropy and facilitating the reconstruction of fibre pathways in the brain (Mori and Barker 1999; Le Bihan et al. 2001; Beaulieu 2002; Catani et al. 2002; Jespersen et al. 2007). Diffusional kurtosis imaging (DKI), an extension of DTI, captures deviations from Gaussian diffusion, yielding additional sensitivity to tissue heterogeneity (Jensen et al. 2005). These methods have enabled widespread clinical applications, including early detection of ischemic stroke (Moseley et al. 1990; Albers 1999), cancer characterisation (Sundgren et al. 2004; Mabray and Cha 2016) and white matter connectivity mapping for neurosurgical planning (Mori and Barker 1999; Romano et al. 2009). They also play a key role in neuroscience and clinical research, providing insights into pathology, ageing, and neuroplasticity (Fieremans et al. 2011; Sagi et al. 2012; Hui et al. 2012; Goveas et al. 2015). However, while sensitive to microstructural tissue alterations, dMRI lacks specificity. Changes in the ADC and kurtosis reflect a plurality of underlying features, such as cell density, membrane permeability, myelination or relaxation rates, leading to ambiguous interpretations (Jespersen et al. 2010; Szczepankiewicz et al. 2016; Lampinen et al. 2017a; Ning et al. 2020; Brabec et al. 2023).

The limited specificity of dMRI largely stems from the limited information content of the signal. Fundamentally, the dMRI signal as a function of diffusion encoding strength is relatively featureless, rightfully described as “remarkably unremarkable” (Yablonskiy and Sukstanskii 2010). However, the problem is exacerbated by the experimental setup on which most dMRI applications are based: the single diffusion encoding (SDE)

developed by Stejskal and Tanner (1965) and named as such by Shemesh et al. (2016). While SDE is the main workhorse of the field, it is a poor probe of tissue because it conflates multiple microstructural features such as microscopic anisotropy, orientation dispersion and isotropic heterogeneity, leading to unreliable characterisation (Westin et al. 2016; Szczepankiewicz et al. 2021b). As a remedy for the shortcomings of SDE, the double diffusion encoding sequence, DDE, (Shemesh et al. 2016) was introduced in a pioneering work by Cory (1990). DDE acquisitions with parallel and orthogonal gradients were shown capable of measuring the local eccentricity of a sample macroscopically isotropic due to orientation dispersion (Cory 1990; Mitra 1995; Callaghan and Komlosh 2002; Özarslan and Basser 2008; Lawrenz et al. 2010; Shemesh et al. 2010; Koch and Finsterbusch 2011; Jespersen et al. 2013). The concept was later extended to tensor-valued encoding using free gradient waveforms (FWF) (Westin et al. 2014, 2016). Another avenue for improving the information content of the signal is time-dependent dMRI, which varies both the diffusion encoding strength and the diffusion time (Tanner 1978; Mitra et al. 1992; Horsfield et al. 1994; Price 1997; Does et al. 2003; Sen 2004; Nilsson et al. 2009; Burcaw et al. 2015; Fieremans et al. 2016; Reynaud 2017; Jespersen et al. 2018; Lee et al. 2018). Combined with biophysical modelling, time-dependent dMRI provides access to far more intricate information about tissue microstructure such as cell sizes (restricted diffusion) and membrane permeability (water exchange) (Pfeuffer et al. 1998; Assaf and Basser 2005; Assaf et al. 2008; Lätt et al. 2009; Alexander et al. 2010; Nilsson et al. 2013; Kiselev 2017; Novikov et al. 2018; Alexander et al. 2019; Novikov et al. 2019; Palombo et al. 2020b; Jelescu et al. 2020). Reliable *in vivo* estimation of these parameters advances dMRI towards being a "virtual microscope", capable of revealing cellular-scale information that was once only accessible through microscopy.

While time-dependent dMRI evidently brings benefits, it still faces challenges due to suboptimal acquisition strategies, model inaccuracy and degeneracy (Jelescu et al. 2016a; Novikov et al. 2018; Coelho et al. 2019; Lampinen et al. 2020a; Jelescu et al. 2020). A major limitation is the inability to disentangle competing contrast mechanisms, which reduces specificity and causes potential misinterpretation. A key example is the interplay between restricted diffusion and exchange, which have opposing effects on the diffusion-weighted signal: as the diffusion time increases, restriction elevates the signal, whereas exchange reduces it (Nilsson et al. 2009; Olesen et al. 2022). SDE-based approaches that rely solely on varying the diffusion time may conflate these effects, potentially biasing parameter estimates. Most methods for probing restricted diffusion with dMRI use SDE with variable diffusion times or oscillating gradients while neglecting exchange (Panagiotaki et al. 2014; Nilsson et al. 2017; Jiang et al. 2017; Veraart et al. 2020). Conversely, exchange measurements are

typically performed using SDE and the Kärger model, which neglects restricted diffusion (Kärger 1985). The interplay between restriction and exchange has been recognised for decades (Stanisz et al. 1997; Price et al. 1998; Meier et al. 2003; Nilsson et al. 2009), but only recently regained attention in modelling efforts (Jiang et al. 2022; Olesen et al. 2022; Jelescu et al. 2022; Lee et al. 2025). These newer methods, all based on SDE with varying diffusion time, either explicitly model both restriction and exchange (using the modified Kärger model) or strategically sample diffusion times to separate exchange-driven signal decrease from restriction-driven signal increase. However, a unified framework that explicitly integrates both effects into experimental design and modelling would further enhance specificity and improve the reliability of microstructural parameter estimates.

Exchange can be probed independently of restricted diffusion under some conditions using filter exchanging imaging (FEXI) (Lasič et al. 2011; Nilsson et al. 2013) which employs DDE acquisitions with variable mixing times. In FEXI, the first diffusion encoding block selectively attenuates the signal from fast-diffusing spins, after which the recovery toward equilibrium is monitored and occurs at a rate known as the apparent exchange rate (AXR). The AXR has been applied to measure exchange in the healthy human brain (Bai et al. 2020), in brain tumours (Lampinen et al. 2017b) and in breast cancer (Lasič et al. 2016). However, FEXI is susceptible to bias due to interactions with imaging gradients (Lasič et al. 2018). A solution to this problem was proposed in the case of free diffusion (Ohene et al. 2023), but not for restricted diffusion. It should be noted that this limitation is not unique to FEXI but also applies to related methods such as Diffusion Exchange Spectroscopy (DEXSY), which can also be used to isolate exchange from restriction effects (Cai et al. 2018, 2022).

Another important confounder for reliable and reproducible exchange estimation with dMRI is anisotropy. While the original Kärger model—the mainstay of all exchange estimation with dMRI—assumes exchange between isotropic Gaussian components, it was extended to account for anisotropy (Fieremans et al. 2010) and applied in recent grey matter microstructure models (Olesen et al. 2022; Jelescu et al. 2022). While these approaches exploit linear tensor encoding with SDE, recent work suggests that adding planar tensor encoding may have benefits (Ghazi et al. 2024). It has been shown previously that AXR from FEXI depends on measurement direction in systems featuring more than two orientationally dispersed compartments (Lasic et al. 2016). Previous studies applying FEXI have shown that AXR is directionally dependent in the monkey brain (Sønderby et al. 2014), in the human brain (Li et al. 2022; Shin et al. 2024) and in numerical simulations (Ludwig et al. 2021). These findings point towards the need for an exchange measurement framework incorporating anisotropy in both theory and experimental design.

All current methods for estimating exchange with dMRI neglect intra-compartmental diffusional kurtosis. Recent work has demonstrated that this kurtosis source can be measured using correlation tensor imaging (CTI) (Henriques et al. 2020, 2021). Studies applying CTI have shown that intra-compartmental kurtosis is non-negligible in both healthy and ischemic brain tissue (Alves et al. 2022; Novello et al. 2022). As noted in these studies, intra-compartmental kurtosis arises from multiple sources including restricted diffusion or cross-sectional variance. The signal contrast enabling estimation of intra-compartmental kurtosis is the difference between an SDE and a parallel DDE acquisition in the long-mixing time limit and at the same diffusion encoding strength (Henriques et al. 2021). Notably, this same contrast also gives maximal sensitivity to exchange (Ning et al. 2018). As such, CTI estimates of intra-compartmental kurtosis are inherently intertwined with intercompartmental exchange. Similarly, exchange estimation may be biased by the presence of intra-compartmental kurtosis. This underscores the need for a dMRI analysis framework that jointly considers both intercompartmental exchange and intra-compartmental kurtosis to disentangle their contributions and improve specificity.

Yet another challenge with time-dependent dMRI is the interpretation of what we measure in the living brain. While cell size estimates can be verified against histology, exchange is an active process that is severely disrupted by tissue extraction and histological preparation. Most studies interpret *in vivo* exchange estimates in terms of membrane permeability (Bai et al. 2020; Olesen et al. 2022; Jelescu et al. 2022), and this view aligns well with measurements in white matter, where there is consensus that exchange is slow and negligible at clinically accessible diffusion times. This notion is supported by the presence of myelin sheaths which impede water transport between the intra- and extra-axonal spaces (Badaut et al. 2011; Bai et al. 2018; Veraart et al. 2019; Brusini et al. 2019; Jelescu et al. 2020). In grey matter, there is strong evidence that exchange is non-negligible (Veraart et al. 2020; Jelescu et al. 2020; Olesen et al. 2022). However, literature values vary greatly, ranging from a few to hundreds of milliseconds (Olesen et al. 2022; Jelescu et al. 2022). Some studies have indicated that structural disorder along neurites (beading, irregularities) has a similar signature on the dMRI signal as permeative exchange (Novikov et al. 2014; Lee et al. 2020; Jelescu et al. 2022; Mougel et al. 2024). Additionally, non-permeative, geometric exchange has been highlighted recently in a simulation study using FEXI, showing that both permeative and non-permeative exchange bear a similar imprint (Khateri et al. 2022). Previous work has also shown that time-dependent dMRI is sensitive to dendritic spines, and that the geometric exchange between dendritic shafts and spines manifests in the same way as permeative exchange (Palombo et al. 2018, 2020a; Chakwizira et al. 2024; Palombo and Şimşek 2024; Şimşek and Palombo 2024). Understanding the dominant

mechanism of exchange in grey matter is important because it informs modelling and experimental design leading to more reliable estimation.

Insights on the processes driving exchange in grey matter could also unlock new dMRI applications in pathology. Take dendritic spines—small protrusions on dendrites that connect to axons and play a central role in information transfer in the brain (Cajal 1924). They are implicated in numerous neuropsychiatric and neurodegenerative diseases (Penzes et al. 2011), yet their *in vivo* estimation remains highly challenging (Howes et al. 2023). The current state-of-the-art method, positron emission tomography, requires exposure to ionising radiation. If dendritic spines drive exchange in grey matter, dMRI exchange measurements could serve as a non-invasive proxy for dendritic spine density, which would bring tremendous value to both neuroscience and clinical care. More broadly, accurate mapping of brain microstructure could also benefit other neuropathologies, such as high-grade gliomas, which remain among the deadliest brain tumours (Ostrom et al. 2014; Nayak and Reardon 2017). Diagnosis still hinges on morphological MRI and invasive biopsies (Jackson et al. 2001; Scott et al. 2002) but dMRI offers a path towards non-invasive histology, with sensitivity to cellularity, heterogeneity, and membrane permeability (Nilsson et al. 2018; Jelescu et al. 2020). Conventional dMRI has shown promise in tumour differentiation and treatment monitoring (Szczepankiewicz et al. 2016; Galbán et al. 2017; Nilsson et al. 2018), while microstructure models have been explored for cell size (Assaf et al. 2008; Alexander et al. 2010) and exchange (Lampinen et al. 2017b) estimation. However, inconsistencies remain, and a lack of clinical studies prevents these model-based approaches from becoming standard.

This thesis aims to address several key gaps in knowledge in dMRI as outlined above. Operating around the central theme of dissociating entangled contrasts, it strives to improve the reliability and interpretation of microstructural measurements with dMRI. The general strategy involves leveraging free gradient waveforms to design multidimensional experiments that elevate the information content of the signal, enabling the inversion of otherwise degenerate signal models. The methods are validated using extensive numerical simulations and their utility is demonstrated in both the healthy human brain and in intracranial tumours.

Finally, it is worth noting that the field of dMRI is currently in a transformative period. The emergence of MRI scanners with ultra-strong gradients marks the beginning of a new era, enabling experiments that were previously impossible (Setsompop et al. 2013; Fan et al. 2014, 2022; Foo et al. 2020; Huang et al. 2021). The methods developed in this thesis stand to benefit greatly from these advancements, paving the way for more reliable and biologically meaningful dMRI studies.

2 Aims

The overarching goal of this thesis was to develop novel MRI contrasts using time-dependent dMRI. It describes a journey starting from theory development to dissociate entangled contrast mechanisms, through experimental design to support the theory and ending with initial applications in both the healthy human brain and in gliomas. The specific aims of the work were to:

1. Disentangle restricted diffusion and exchange, by developing theory and an optimised experimental design accounting for both effects, and test this restriction-exchange framework with Monte Carlo simulations and in the healthy human brain (Paper I, Paper II)
2. Correct crusher gradient-induced bias in FEXI using the restriction-exchange framework above (Paper III)
3. Separate exchange and anisotropy by developing theory and an experimental approach for measurement of both effects (Paper IV)
4. Disentangle exchange from intra-compartmental kurtosis by developing theory and an experimental approach for measurement of both (Paper IV)
5. Investigate the impact of dendritic spines on exchange estimation with dMRI (Paper V)
6. Explore the utility of exchange estimation with free waveforms in gliomas (Paper VI)

3 The microstructure of brain tissue

An understanding of the cellular architecture of neural tissue is essential for interpreting dMRI contrasts. This chapter provides an overview of brain tissue microstructure with a focus on the key components of neurons and glial cells, the organization of grey and white matter, the cerebellar anatomy, and cell membrane permeability to water—all of which contribute to the diffusion-weighted signal and inform the interpretations presented in this thesis.

3.1 Brain tissue composition

Neural tissue comprises two main constituents: neurons which are responsible for information transfer and glia which provide support and protection for the neurons (Purves et al. 2001; Clark et al. 2010; Allen and Lyons 2018). This section provides an overview of both.

3.1.1 The neuron

The neuron is the fundamental signalling unit of the nervous system (Purves et al. 2001; Clark et al. 2010). It is highly specialised for receiving and transmitting electrical and chemical signals. A typical neuron (illustrated in Fig. 1) comprises three main parts: a cell body (soma) which contains the cell nucleus, dendrites (membranous processes that receive input from other neurons) and an axon (a long nerve fibre which conducts nerve impulses to other neurons) (Purves et al. 2001). Neurons occur in two varieties: stellate (bearing short axons for short-range connections) and pyramidal (featuring long axons for long-range connections).

Somas have varying diameters ranging from a few to one hundred micrometres (Braitenberg and Schüz 1998). Dendrites have diameters ranging from 10 μm at the origin, tapering down to 0.5 μm at the distal end. Axons have variable diameters, with the majority in the human brain falling in the range 0.5–2 μm (Aboitiz et al. 1992; Liewald et al. 2014). They are usually covered in myelin sheaths that wrap around the

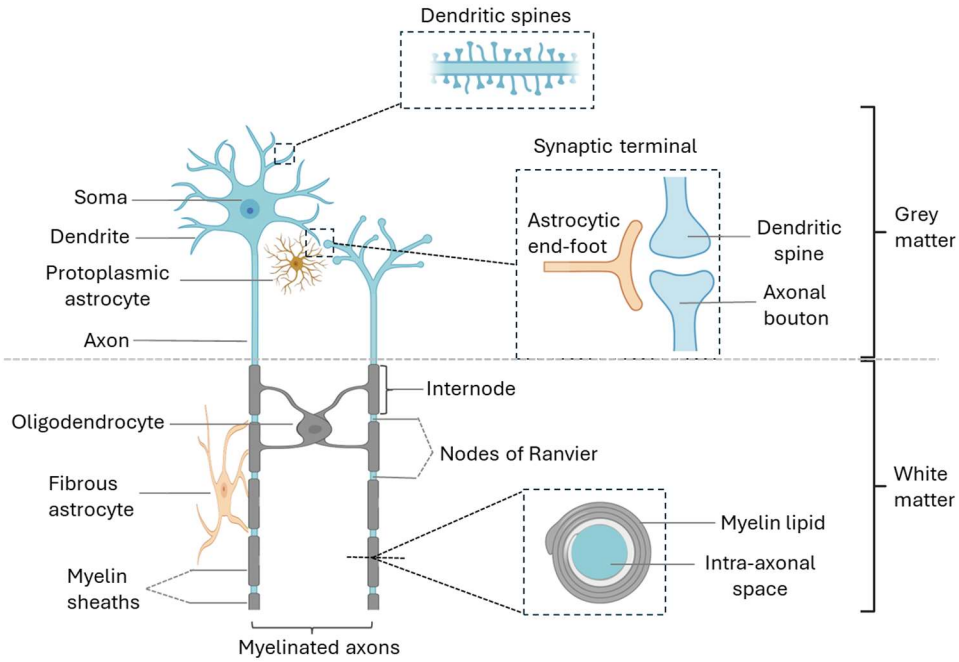

Figure 1. Constituents of neuronal tissue. Grey matter consists primarily of neuronal cell bodies (somas), unmyelinated axons, and glial cells such as protoplasmic astrocytes. Dendrites extend from somas and are studded with dendritic spines that form synaptic contacts with other neurons. White matter is composed mainly of myelinated axons and supporting glial cells, including oligodendrocytes (which produce myelin) and fibrous astrocytes (which provide support for the neurons). Myelin comprises lipid layers separated by water-filled spaces and occurs in internodes separated by nodes of Ranvier.

axon more than a hundred times and function as electric insulators that increase the signal conduction speed by over ten-fold for axons of similar diameter (Trapp and Kidd 2004). Myelin sheaths occur in intervals (internodes) of up to nearly 2 mm, separated by nodes of Ranvier which are up to 5 µm in length (Hildebrand et al. 1993; Trapp and Kidd 2004). Myelin sheaths are made up of membranous lipid concentric layers separated by narrow water-filled spaces.

Glial cells (glia) are non-neuronal cells whose function is to maintain homeostasis and support neuron function (Purves et al. 2001; Allen and Lyons 2018). They provide structural support, nutrition, insulation and other regulatory functions necessary for neural activity. Glia are extremely abundant, making up about half of all cells in the human central nervous system. The most common glial cells are oligodendrocytes and astrocytes (Purves et al. 2001). Oligodendrocytes are responsible for producing myelin and have cell body diameters of between 6 and 8 µm (Edgar and Griffiths 2009).

Astrocytes are star-shaped cells that provide metabolic and structural support to neurons and have cell body diameters of about 10–12 μm (Edgar and Griffiths 2009).

3.1.2 Synaptic terminals

Dendrites feature many small protrusions on their surfaces, called dendritic spines (Fig. 1), whose function is to form functional contacts with the axons of other neurons (Purves et al. 2001). Spines connect to the synaptic boutons found at the distal end of axons, forming the synaptic terminal where information transfer occurs. They were first observed in 1888 by Ramon y Cajal (Cajal 1924) and are now recognised as the primary site of excitatory synapses in the mammalian brain (Runge et al. 2020). Spines exhibit high plasticity and occur in a variety of shapes depending on their level of maturity, where bulbous, mushroom-shaped variants are the most stable (Bączyńska et al. 2021). They have head diameters ranging from 0.5 to 1.2 μm, neck diameters of 0.05–0.5 μm and neck lengths of 0.5–2 μm (Li et al. 2023b).

3.1.3 Grey and white matter constituents

Grey matter consists mainly of somas (the nuclei of which give it its characteristic dark hue), dendrites, unmyelinated axons and glial cells (Kandel 2013). It is found predominantly near the surface of the brain where it forms the cerebral cortex whose thickness varies between 2 and 5 mm (Kandel 2013). It is also found more sparsely in regions such as thalamus and basal ganglia. Human cortical grey matter is primarily made up of neurites (dendrites and unmyelinated axons, 60%). The remainder of the volume is taken up by somas (8%) and extracellular space (18%) while glia, synapses and capillaries occupy the rest (Howes et al. 2023).

White matter consists primarily of myelinated axons and supporting glial cells. The axons are arranged in bundles known as tracts. By volume, white matter comprises 68% intra-axonal space and myelin, and the rest is taken up by cell bodies of glia, intra-axonal space of unmyelinated axons, extracellular space and blood vessels (Perge et al. 2009; Jelescu et al. 2016b). The abundance of myelin, and its high lipid content, give white matter its characteristic pale appearance.

3.1.4 Cerebellar anatomy

The cerebellar grey matter has a highly complex microstructure when compared to the cerebral cortex. It features three layers (molecular, Purkinje and granular) overlying a central white matter core (Voogd and Glickstein 1998; Tax et al. 2020; Consalez et al.

2021; Nguyen et al. 2021). The granular layer is densely packed with granule cells—the most abundant neuron in the central nervous system—with somas about 7 μm in diameter. Axons of the granule cells are unmyelinated, and they ascend towards the molecular layer where they bifurcate into two branches, forming parallel fibres (Voogd and Glickstein 1998). The Purkinje layer is narrow (single-cell-thick) and contains the large cell bodies of Purkinje cells, with diameters of 25–40 μm. Purkinje cells have elaborate dendritic trees that fan out into the molecular layer. Their axons—the only output from the cerebellar cortex—are myelinated and descend towards the cerebellar nuclei in the white matter core (Voogd and Glickstein 1998).

3.2 The cell membrane

Cell membranes are the biological component responsible for confining molecules to the intracellular space. They are semipermeable and selectively admit water molecules. The permeability of the cell membrane to water molecules is a crucial property for regulation of cell function and maintenance of homeostasis (Phillips et al. 2012). Water transport across the bilipid layer of the cell membrane can either be passive or facilitated by membrane channel proteins.

Passive permeability refers to the direct diffusion of water molecules through the lipid bilayer and is typically much slower than facilitated transport (Verkman et al. 2008). Cells overcome the limited rate of passive transport by expressing aquaporins, which are a family of membrane proteins that function as water-selective channels (Borgnia et al. 1999; Agre and Kozono 2003; Reuss 2012). Aquaporins are remarkably selective, allowing a very high throughput of water molecules while blocking out other solutes. Their dramatic effectiveness at transporting water across the membrane has been observed in red blood cells, which exhibit high permeability due to abundant expression of the aquaporin AQP1 (Preston et al. 1992). In brain tissue, AQP4 is the predominant water channel (Verkman et al. 2008), primarily localised to astrocytic endfeet at the blood–brain and CSF–brain interfaces. In conditions such as stroke, cerebral oedema and hydrocephalus, AQP4 is responsible for moving water into and out of brain tissue.

4 Diffusion: principles and encoding

This chapter provides a summarised description of the basic principles of diffusion and how they relate to the MRI signal. Concretely, it delves into the diffusion equation and propagator formalism and provides solutions in simple environments where the problem is tractable.

4.1 Principles of diffusion

4.1.1 The diffusion equation and the propagator formalism

Diffusion refers to the random translational motion of particles driven by thermal fluctuations in the medium (Price 2009). The physics of diffusion is encapsulated by the diffusion equation, which reads (Fick 1855; Duffy 2001; Price 2009; Callaghan 2011a) [1]

$$\frac{\partial P(\mathbf{r}_0, \mathbf{r}_1, t)}{\partial t} = D\nabla^2 P(\mathbf{r}_0, \mathbf{r}_1, t), \tag{1}$$

with the initial condition $P(\mathbf{r}_0, \mathbf{r}_1, 0) = \delta(\mathbf{r}_1 - \mathbf{r}_0)$, where δ is the Dirac delta function, D is the diffusion coefficient and $P(\mathbf{r}_0, \mathbf{r}_1, t)$ is the so-called diffusion propagator, which describes the probability that a particle initially at position $\mathbf{r}_0$ is found at position $\mathbf{r}_1$ after time t.

For free diffusion, Eq. 1 is readily solved, yielding the Gaussian

$$P(\mathbf{r}_0, \mathbf{r}_1, t) = \frac{1}{(4\pi D t)^{\frac{3}{2}}} \exp\left(-\frac{(\mathbf{r}_1 - \mathbf{r}_0)^2}{4Dt}\right). \tag{2}$$

[1] This equation comes from combining Fick's first law $\mathbf{J}(\mathbf{r}, t) = -D\nabla c(\mathbf{r}, t)$ with the continuity equation $\partial c(\boldsymbol{r}, t)/\partial t = -\nabla \cdot \mathbf{J}(\mathbf{r}, t)$ and replacing the concentration c with the propagator.

For cases other than free diffusion, this local propagator is rich in information about the diffusion process, and thus the diffusion environment, around $\mathbf{r}_0$. However, it is inaccessible in practical experiments. A more useful quantity is the ensemble-averaged or mean propagator, $\bar{P}(\mathbf{R}, t)$ where $\mathbf{R} = \mathbf{r}_1 - \mathbf{r}_0$, which is obtained by integrating over all starting positions $\mathbf{r}_0$.[2]

4.1.2 Anisotropic diffusion

Worth noting is that the notion of a scalar diffusion coefficient as used above is only meaningful when diffusion is isotropic. In anisotropic media, the diffusion coefficient has dependence on direction and is more appropriately treated as a tensor with the matrix representation (Crank 1975; Basser et al. 1994; Price 2009; Jones 2010)

$$\mathbf{D} = \begin{pmatrix} D_{\mathrm{xx}} & D_{\mathrm{xy}} & D_{\mathrm{xz}} \\ D_{\mathrm{yx}} & D_{\mathrm{yy}} & D_{\mathrm{yz}} \\ D_{\mathrm{zx}} & D_{\mathrm{zy}} & D_{\mathrm{zz}} \end{pmatrix}. \tag{3}$$

The matrix $\mathbf{D}$ is symmetric and positive definite and therefore has six independent elements. In the principal axis system, off-diagonal elements are zero and the diagonal elements give the eigenvalues of the tensor corresponding to three eigenvectors.

4.1.3 Correlation functions and time-dependent diffusion

The propagator formalism allows the definition of useful statistical metrics such as the mean squared displacement (MSD) given by the second moment of the propagator (Price 2009; Callaghan 2011a). A hallmark of Gaussian diffusion is that the MSD grows linearly with time

$$\langle [\mathbf{r}(t) - \mathbf{r}(0)]^{\otimes 2} \rangle = 2\mathbf{D}t, \tag{4}$$

where "$\otimes$" denotes the outer tensor product. Non-Gaussian diffusion is associated with time-dependent diffusion coefficients, which can be defined via the MSD as

$$\mathbf{D}(t) = \frac{\langle [\mathbf{r}(t) - \mathbf{r}(0)]^{\otimes 2} \rangle}{2t}. \tag{5}$$

[2] The medium averaged propagator is given by $\bar{P}(\mathbf{R}, t) = \int \rho(\mathbf{r}_0) P(\mathbf{r}_0, \mathbf{r}_0 + \mathbf{R}, t)\, \mathrm{d}\mathbf{r}_0$, where $\rho(\mathbf{r}_0)$ is the equilibrium particle density that depends on the diffusion environment.

4.2 Diffusion encoding in MRI

4.2.1 The Stejskal-Tanner experiment

The focus now turns to the interaction between the diffusion process described in the previous section and the MRI experiment. This coupling was described by Torrey who combined the Bloch equations with the diffusion equation to yield the Bloch-Torrey equation (Torrey 1956)

$$\frac{\partial \mathbf{M}}{\partial t} = \gamma \mathbf{M} \times \mathbf{B} - \frac{M_x \mathbf{i} + M_y \mathbf{j}}{T_2} - \frac{M_z - M_0}{T_1}\mathbf{k} - \nabla \cdot (D \nabla \mathbf{M}), \qquad (6)$$

where $\mathbf{M}$ is the magnetisation with three orthogonal components (M_x, M_y and M_z), M_0 is the equilibrium magnetisation due to a static magnetic field along z, $\mathbf{B}$ is an inhomogeneous magnetic field and T_2 and T_1 are the transverse and longitudinal relaxation times, respectively. Equation 6 describes a source-sink process, where the magnetisation created by the field dissipates due to both relaxation and diffusion.

The classic way of sensitising the MRI signal to diffusion is the Stejskal-Tanner experiment (Stejskal and Tanner 1965) which adds a gradient pulse on either side of the refocusing pulse in a spin-echo pulse sequence (Fig. 2). The essence of the experiment is that incoherent motion between the first and second gradient pulses leads to a net phase change and a consequent signal decrease.

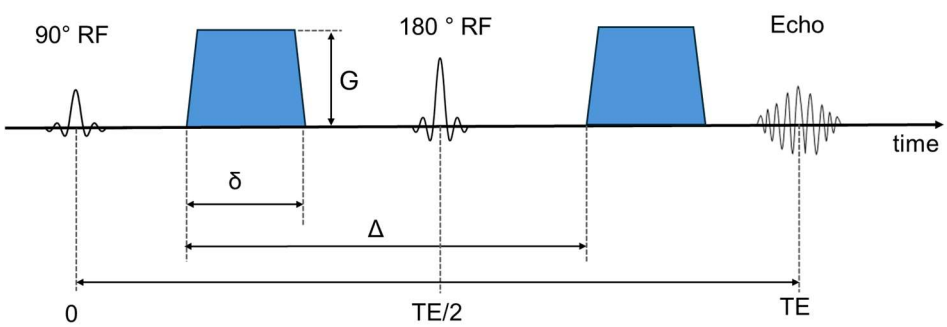

Figure 2. The Stejskal-Tanner experiment. The diffusion encoding gradient pulses (blue blocks of amplitude G) are applied on either side of the 180° refocusing pulse in a spin-echo sequence. The times δ and Δ denote the duration and spacing of the diffusion-encoding gradients and TE is the echo time. Incoherent spin motion between the two gradients results in a net phase change and a consequent signal attenuation.

The accumulated phase due to the application of the diffusion-sensitising gradients is given by (Callaghan 2011a)

$$\phi = \gamma \int_0^T \mathbf{g}(t) \cdot \mathbf{r}(t) \mathrm{d}t \tag{7}$$

where "·" denotes the scalar product, γ is the gyromagnetic ratio, $\mathbf{g}(t)$ is the diffusion-encoding gradient waveform with total duration T and $\mathbf{r}(t)$ is the spin trajectory. Already at this stage, the coupling between the dMRI experiment, $\mathbf{g}(t)$, and the microstructure, $\mathbf{r}(t)$, is evident. In fact, much of the work presented in this thesis can be summarised as efforts to design $\mathbf{g}(t)$ to extract as much independent information as possible from correlations of $\mathbf{r}(t)$.

Since $\mathbf{r}(t)$ is stochastic, ϕ is described by a probability distribution $P(\phi)$, and the diffusion-weighted signal is obtained by averaging over the phase factors of all contributing spins

$$S(\mathbf{q}, T)/S_0 = \int e^{-i\phi} P(\phi) \mathrm{d}\phi = \langle e^{-i\phi} \rangle , \tag{8}$$

where S_0 is the signal in the absence of diffusion-sensitising gradients. Given any gradient waveform, Eq. (8) predicts the diffusion-weighted signal provided $\mathbf{r}(t)$ is also known. However, since $\mathbf{r}(t)$ is inaccessible, it is instructive to consider simplifying cases to gain insight into what information about the diffusion process *can* be accessed with MRI. One such simplifying case is the narrow-pulse regime discussed in the following.

4.2.2 Diffusion-weighted signal with narrow pulses

Assuming that the gradient pulses in Fig. 2 are narrow, the accumulated phase evaluates to (Callaghan 2011a)

$$\phi = \gamma \delta \mathbf{g} \cdot \mathbf{R} = \mathbf{q} \cdot \mathbf{R} , \tag{9}$$

where δ is the pulse duration, $\mathbf{R} = [\mathbf{r}(\Delta) - \mathbf{r}(0)]$ is the displacement over the diffusion time (Δ) and $\mathbf{q} = \gamma \delta \mathbf{g}$ is the dephasing q-vector. The signal equation can then be expressed

$$S(\mathbf{q}, T)/S_0 = \langle \mathrm{e}^{i\mathbf{q}\cdot\mathbf{R}} \rangle = \int \bar{P}(\mathbf{R}, \Delta)\, \mathrm{e}^{i\mathbf{q}\cdot\mathbf{R}} \mathrm{d}\mathbf{R} , \tag{10}$$

where $\bar{P}(\mathbf{R}, \Delta)$ is the medium-averaged propagator introduced earlier. Notice that, in the narrow-pulse regime, the dMRI experiment accesses the average propagator via the Fourier transform (Callaghan 1991; Grebenkov 2007). This is an important result since it reveals the link between the dMRI experiment and measurable parameters that quantify or characterise the diffusion process. To clarify this point, consider again the simple case of a Gaussian propagator, where Eq. 11 evaluates to

$$S(\mathbf{q}, T)/S_0 = \exp\left(-\mathbf{q}^{\otimes 2}\Delta : \mathbf{D}\right) = \exp(-\mathbf{B} : \mathbf{D}) \,, \tag{12}$$

where ":" denotes the Frobenius inner product, $\mathbf{B} = \mathbf{q}^{\otimes 2}\Delta$ is called the b-tensor (or b-matrix) (Mattiello et al. 1997; Westin et al. 2014, 2016) and its trace ($b = |\mathbf{q}|^2\Delta$) is called the b-value and measures the strength of the diffusion weighting . A more general definition of the b-value incorporating pulses of finite duration is (Stejskal and Tanner 1965)

$$b = q^2 t_d = q^2 \left(\Delta - \frac{\delta}{3}\right) \,, \tag{13}$$

where $q = |\mathbf{q}|$ and $t_d = \Delta - \frac{\delta}{3}$ is the diffusion time. Equation (12) presents the well-known result that, given a Gaussian propagator, dMRI probes diffusivity via the b-value.

4.2.3 Beyond narrow pulses: multiple propagator formalism

Although the narrow pulse approximation simplifies modelling, it is rarely achievable in practice due to hardware constraints. Diffusion encoding with gradient pulses of finite duration or, generally, gradients for which $\mathbf{q}$ is a non-constant function of time, cannot be described by Eq. 10. One solution to the problem is the multiple propagator approach (Caprihan et al. 1996; Callaghan 1997) which involves approximating the gradient waveform with a series of impulses and applying the narrow pulse approximation (Eq. 10) in each time interval. However, in practice, this approach often results in a time-consuming signal evaluation that is also prone to errors due to discretisation.

4.2.4 The cumulant expansion

An alternative, and appreciably more convenient, approach for describing the diffusion-weighted signal under realistic gradients is to restrict the measurement to low b-values and adopt the cumulant expansion of the phase distribution (van Kampen 2007; Price

2009; Kiselev 2010). This expansion expresses the logarithm of the signal (Eq. 8) as a Taylor series, where each term corresponds to a statistical cumulant of the phase distribution

$$\ln\langle \mathrm{e}^{-i\phi}\rangle = -ic_1 - \frac{1}{2!}c_2 + \frac{i}{3!}c_3 + \frac{1}{4!}c_4 + \cdots, \tag{14}$$

where the cumulants c_i are related to the moments of $P(\phi)$ via

$$\begin{aligned} c_1 &= \langle\phi\rangle \\ c_2 &= \langle\phi^2\rangle - \langle\phi\rangle^2 \\ c_3 &= \langle\phi^3\rangle - 3\langle\phi\rangle\langle\phi^2\rangle + 2\langle\phi\rangle^3 \\ c_4 &= \langle\phi^4\rangle - 4\langle\phi\rangle\langle\phi^3\rangle + 12\langle\phi\rangle^2\langle\phi\rangle^2 - 3\langle\phi^2\rangle^2 - 6\langle\phi\rangle^4 \\ &\vdots \end{aligned} \tag{15}$$

In the absence of bulk flow (an assumption made throughout this thesis), all odd-order moments are zero, and thus, to fourth order, Eq. 14 can be written

$$\ln S/S_0 \approx -\frac{1}{2}\langle\phi^2\rangle + \frac{1}{24}(\langle\phi^4\rangle - 3\langle\phi^2\rangle^2)\,. \tag{16}$$

It is worth noting that diffusion in a single Gaussian environment is fully described by the second cumulant and all cumulants of order higher than 2 are zero.

4.2.5 Correlation functions and encoding properties

The cumulant expansion introduced in the preceding section is a powerful tool for understanding how different diffusion processes are encoded into the MRI signal. To demonstrate, recall the definition of the phase given in Eq. 7, which allows the second moment in Eq. 16 to be written

$$\langle\phi^2\rangle = \gamma^2 \int_0^T \int_0^T \mathbf{g}(t_1)\otimes\mathbf{g}(t_2) : \langle\mathbf{r}(t_1)\otimes\mathbf{r}(t_2)\rangle \,\mathrm{d}t_1\mathrm{d}t_2\,. \tag{17}$$

Eq. 17 shows that the position autocorrelation function is weighted by the gradient autocorrelation $\widehat{\mathbf{G}}(t) = \int_0^T \mathbf{g}(\tau)\otimes\mathbf{g}(t+\tau)\,d\tau$. It is, however, often more convenient

to describe diffusion in terms of particle velocities instead of positions. Integration by parts can be used to redefine the phase in terms of spin velocities, $\mathbf{v}(t)$,

$$\phi = -\int_0^T \mathbf{q}(t)\cdot\mathbf{v}(t)\mathrm{d}t\,, \tag{18}$$

leading to the following expression for the second moment

$$\langle\phi^2\rangle = \int_0^T\int_0^T \mathbf{q}(t_1)\otimes\mathbf{q}(t_2) : \langle\mathbf{v}(t_1)\otimes\mathbf{v}(t_2)\rangle\,\mathrm{d}t_1\mathrm{d}t_2\,, \tag{19}$$

illustrating that the velocity autocorrelation function (VAF) is weighted by the autocorrelation function of the q-vector, $\widehat{\mathbf{Q}}(t) = \int_0^T \mathbf{q}(\tau)\otimes\mathbf{q}(t+\tau)\,d\tau$. The second-order VAF contains information about the time-dependence of the diffusivity, and this is made apparent by highlighting its relation to the diffusion spectrum via the inverse Fourier transform (Callaghan 2011b)

$$\langle\mathbf{v}(t_1)\otimes\mathbf{v}(t_2)\rangle = \frac{1}{\pi}\int_{-\infty}^{\infty}\mathbf{D}(\omega)\mathrm{e}^{i\omega|t_2-t_1|}d\omega. \tag{20}$$

Note that the second-order VAF does not depend on the absolute values of t_1 or t_2, but rather the difference between them, much like the MSD. In fact, the second order VAF, the MSD and the diffusion spectrum all contain the same information as they can be computed from each other. However, as later chapters will illustrate, targeting the diffusion spectrum in the frequency domain provides a convenient way to understand what part of this information is accessible. In terms of the diffusion spectrum, the second moment can be written

$$\langle\phi^2\rangle = \frac{1}{\pi}\int_{-\infty}^{\infty}|\mathbf{Q}(\omega)|^{\otimes 2} :\, \mathbf{D}(\omega)\mathrm{d}\omega\ , \tag{21}$$

where $\mathbf{Q}(\omega)$ is the diffusion encoding spectrum given by the Fourier transform of $\mathbf{q}(t)$. For the case of diffusion in a single Gaussian environment (where $\mathbf{D}(\omega)$ is constant), the second-order VAF is given by

$$\langle\mathbf{v}(t_1)\otimes\mathbf{v}(t_2)\rangle = \frac{1}{\pi}\int_{-\infty}^{\infty}\mathbf{D}\mathrm{e}^{i\omega|t_2-t_1|}d\omega = 2\mathbf{D}\delta(t_2-t_1), \tag{22}$$

where δ is the Dirac delta function. The result presented in Eq. 12 (signal attenuation driven by the b- and diffusion tensors) can be recovered by combining Eq. 21 and 22, yielding the second cumulant

$$\langle \phi^2 \rangle = \int_0^T \int_0^T \mathbf{q}(t_1) \otimes \mathbf{q}(t_2) : 2\mathbf{D}\delta(t_2 - t_1)\, \mathrm{d}t_1 \mathrm{d}t_2 = 2\mathbf{B}:\mathbf{D}, \tag{23}$$

where

$$\mathbf{B} = \int_0^T \mathbf{q}(t) \otimes \mathbf{q}(t) \mathrm{d}t \tag{24}$$

is the b-tensor introduced for narrow pulses earlier but defined more generally here. The above discussion illustrates the versatility of the cumulant expansion: no demands are made on the shape of the gradient waveform. Of course, the caveat is that the expansion is valid only at low b-values.

Given the insights provided by the second-order VAF, it is only instructive to also introduce the fourth-order VAF, which is contained in the fourth moment of the phase distribution via the cumbersome expression

$$\begin{aligned} \langle \phi^4 \rangle = \int_0^T \int_0^T \int_0^T \int_0^T \mathbf{q}(t_1) \otimes \mathbf{q}(t_2) \otimes \mathbf{q}(t_3) \otimes \mathbf{q}(t_4) : \\ \langle \mathbf{v}(t_1) \otimes \mathbf{v}(t_2) \otimes \mathbf{v}(t_3) \otimes \mathbf{v}(t_4) \rangle \, \mathrm{d}t_1 \mathrm{d}t_2 \mathrm{d}t_3 \mathrm{d}t_4. \end{aligned} \tag{25}$$

As is evident from the above, the fourth order VAF is a high-dimensional object—a fourth order tensor dependent on spin dynamics at four different time-points. For simplicity—and without loss of generality—the rest of this chapter will drop the tensorial description.

It turns out, as we have shown in previous work (Chakwizira et al. 2022), that insights about restricted diffusion and exchange can be gleaned from the fourth-order VAF via a temporal decomposition analysis. For clarity, we represent the temporal arguments as subscripts such that $v(t_1) = v_a$, $v(t_2) = v_b$, and so forth. The fourth-order cumulant features the fourth-order VAF and products of second-order terms as given by

$$C_{abcd} = \langle v_a v_b v_c v_d \rangle - \langle v_a v_b \rangle \langle v_c v_d \rangle - \langle v_a v_c \rangle \langle v_b v_d \rangle - \langle v_a v_d \rangle \langle v_b v_c \rangle \tag{26}$$

With this formalism, we define the weighting function in Eq. 25 as

$$Q_{abcd} = q_a q_b q_c q_d \tag{27}$$

where the fourth cumulant is then given by $o_4 = C_{abcd} : Q_{abcd}$ where ":" now denotes integration over all four time points.

As shown in previous work (Chakwizira et al. 2022), independent information contained in the fourth order velocity autocorrelation function can be revealed by defining distinct temporal decompositions such as

$$o_4^{aaaa} = C_{abcd} : Q_{abcd}\delta_{ab}\delta_{bc}\delta_{cd} \tag{28}$$

and

$$o_4^{aabb} = C_{abcd} : Q_{abcd}\delta_{ab}\delta_{cd}(1 - \delta_{ac}) \tag{29}$$

where δ_{nm} is the Kronecker delta which takes the value 1 when $n = m$ and is otherwise zero. With this formalism, the fourth-order cumulant can be written

$$o_4^{total} = o_4^{aaaa} + 3 \cdot o_4^{aabb} + o_4^{rest} \tag{30}$$

where the factor of 3 accounts for three different combinations of the *aabb* terms and "rest" denotes all contributions not included in the first two terms. As illustrated in Fig. 3A, this decomposition reveals distinct signatures of different microstructures, with the first two terms on the right-hand-side being related to Gaussian diffusion and exchange, while the third term is non-zero only in the presence of restricted/hindered diffusion. Such insights can also guide the design of experiments to probe exchange. For example, as Fig. 3B shows, DDE is a more specific probe of exchange than SDE because it has its encoding power concentrated along the *aabb* axis where exchange manifests.

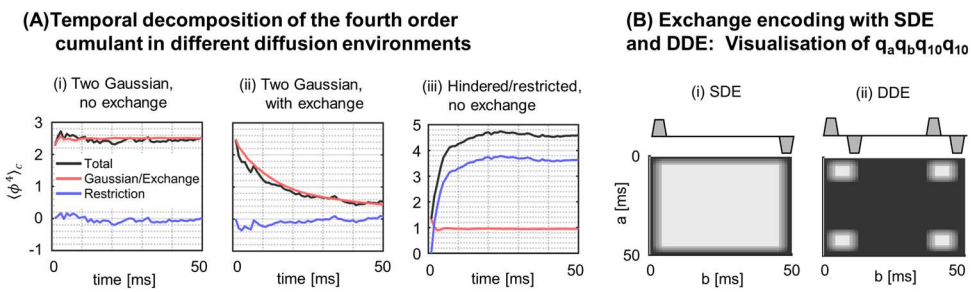

Figure 3. Temporal decomposition of the fourth-order cumulant. Panel A shows three components of the fourth order cumulant obtained by a temporal decomposition of the velocity autocorrelation function (Eq. 30), plotted against the diffusion time in a narrow-pulse SDE experiment. The restriction component is zero for multi-Gaussian diffusion, as expected, and rises with the diffusion time for restricted/hindered diffusion. In a multi-Gaussian setting, exchange causes a temporal decline in the Gaussian/Exchange contribution but has no effect on the restriction component. Panel B shows the decomposition of the weighting function in Eq. 27 along the Gaussian/Exchange axis, for SDE and DDE. Unlike SDE, the encoding power in DDE is focused along the *aabb* axis, illustrating that DDE is a more specific probe of exchange than SDE. Figure adapted, with permission, from (Chakwizira et al. 2022), published by the ISMRM.

5 The forward problem: signal representations and models

This chapter reviews the forward problem of dMRI, which involves deriving analytical expressions to predict the diffusion-weighted signal under given measurement settings. Prominent approaches are outlined, and they all fall into two broad categories: signal representations and microstructure models (Novikov et al. 2018). Models are often built on strong assumptions about the source of the signal (the tissue microstructure), while representations are more parsimonious and make no assumptions about the microstructure. Models, when correctly specified such that they capture the salient features influencing the diffusion process, yield parameter estimates more specific to tissue changes. Representations, on the other hand, provide indices highly sensitive to tissue changes but generally exhibit low specificity. In the following, signal representations including DTI, DKI, QTI and CTI will be discussed alongside the widely used Kärger model of exchange as well as common models of restricted diffusion.

5.1 Non-exchanging Gaussian environments

This section presents common dMRI models and signal representations describing diffusion in ensembles of non-exchanging Gaussian environments (DTI, DKI, QTI), ending with a novel extension capturing intra-compartmental non-Gaussian diffusion (CTI).

The overarching signal representation governing the approaches outlined herein considers a diffusion environment featuring multiple distinct components, each having its own set of second and fourth-order cumulants o_2 and o_4. Averaging over these components provides (Jespersen et al. 2019)

$$\ln S/S_0 \approx -\frac{1}{2}\langle o_2\rangle + \frac{1}{24}\Big(\langle o_4\rangle + 3(\langle o_2^2\rangle - \langle o_2\rangle^2)\Big) \tag{31}$$

That is, the second cumulant is merely the average of the individual second cumulants while the fourth cumulant contains an average of the individual fourth cumulants (the intra-compartmental, microscopic or intrinsic contribution) plus the dispersion in second cumulants (the intercompartmental contribution). An expression for o_2 was derived in previous chapters: $o_2 = 2\mathbf{B}{:}\,\mathbf{D}$.

5.1.1 Diffusion tensor imaging

Diffusion tensor imaging has become a cornerstone technique in neuroimaging, finding widespread application in studies of normal brain development and ageing(Moseley 2002; Scholz et al. 2009; Lebel and Deoni 2018) as well as in pathologies such as stroke (Sotak 2002) and cancer (Jiang et al. 2014). DTI considers measurements at low b-values where the signal is adequately described by only the second-order cumulant, giving the representation (Basser et al. 1994)

$$\ln S/S_0 \approx -\mathbf{B}{:}\,\langle\mathbf{D}\rangle \tag{32}$$

where $\langle\mathbf{D}\rangle$ is the average diffusion tensor in an environment characterised by a distribution of diffusion tensors. Estimation of this tensor allows the definition of metrics such as the mean diffusivity, MD, proportional to its trace, and the fractional anisotropy (FA) quantifying its anisotropy.

5.1.2 Diffusion kurtosis imaging

Diffusion kurtosis imaging (Jensen et al. 2005; Jensen and Helpern 2010) is an extension of DTI that captures tissue heterogeneity and has been shown to outperform DTI in tumour grading (Raab et al. 2010; Van Cauter et al. 2012). DKI relies on measurements at higher b-values which provide access to the fourth cumulant in Eq. 16, giving the signal representation (Jensen et al. 2005)

$$\ln S/S_0 \approx -\mathbf{B}{:}\,\langle\mathbf{D}\rangle + \frac{1}{6}\mathbf{B}^{\otimes 2}\overline{D}^2{:}\,\mathbb{W}, \tag{33}$$

where $\mathbb{W}$ is a fourth-order total kurtosis tensor quantifying deviation from Gaussian diffusion and $\overline{D} = \frac{1}{3}\mathrm{trace}(\langle\mathbf{D}\rangle)$. The term "total" is used to indicate that the tensor incorporates all kurtosis sources such as isotropic and anisotropic and microscopic. Taking the powder average of Eq. 33 provides the familiar DKI signal representation

$$\ln S/S_0 \approx -b\overline{D} + \frac{1}{6}b^2\overline{D}K_T, \tag{34}$$

where K_T is the mean total kurtosis (note that this is generally different from the average of kurtosis measured in different directions).

5.1.3 Q-space trajectory imaging

Diffusion kurtosis imaging, owing to its reliance on SDE acquisitions, is inherently incapable of resolving the isotropic and anisotropic components of the kurtosis tensor. Isotropic heterogeneity and microscopic anisotropy can be teased apart by varying the shape of the b-tensor, which demands going beyond the canonical SDE and using, for example, a combination of planar and orthogonal DDE (Cory 1990; Shemesh et al. 2010; Jespersen et al. 2013), or more generally using free waveforms and the q-space trajectory imaging (QTI) framework (Westin et al. 2016). Dissociating isotropic heterogeneity and microscopic anisotropy has been shown to improve tissue characterisation in conditions such as cancer (Szczepankiewicz et al. 2016), epilepsy (Lampinen et al. 2020b) and multiple sclerosis (Andersen et al. 2020). QTI is founded on the multiple Gaussian components premise where $\langle o_4 \rangle$ is assumed to be zero. The signal representation reads (Jensen et al. 2005; Westin et al. 2014, 2016)

$$\ln S/S_0 \approx -\mathbf{B}\colon\langle\mathbf{D}\rangle + \frac{1}{2}\mathbf{B}^{\otimes 2}\colon\mathbb{C}, \tag{35}$$

where $\mathbb{C}$ is a fourth-order covariance tensor given by

$$\mathbb{C} = \left\langle\mathbf{D}^{\otimes 2}\right\rangle - \langle\mathbf{D}\rangle^{\otimes 2}. \tag{36}$$

The role of the b-tensor shape can be appreciated by considering the powder average of Eq. 35,

$$\ln S/S_0 \approx -b\overline{D} + \frac{1}{2}b^2\left(V_I + b_\Delta^2 V_A\right), \tag{37}$$

where $\overline{D} = \langle\mathbf{D}\rangle\colon\mathbf{I}_I$ is the mean diffusivity with $\mathbf{I}_I$ being an isotropic tensor, V_I and V_A are the isotropic and anisotropic variances defined through $V_I = \mathbb{C}\colon\mathbb{I}_I$ and $V_A = \mathbb{C}\colon\mathbb{I}_A$ where $\mathbb{I}_I$ and $\mathbb{I}_\mathrm{A}$ are fourth-order isotropic tensors, respectively, (Basser and Pajevic 2003; Eriksson et al. 2015; Westin et al. 2016; Nilsson et al. 2020) and b_Δ is the shape of the b-tensor given for axisymmetric tensors by $b_\Delta = \frac{(\lambda_{||} - \lambda_\perp)}{b}$ where $\lambda_{||}$ and $\lambda_\perp$ are

the axial and radial eigenvalues (Eriksson et al. 2015). For linear, planar and spherical tensor encoding, b_Δ takes the values 1, -1/2 and 0, respectively. SDE acquisitions yield linear tensors which probe the total variance given by $V_T = V_I + V_A$.

5.1.4 Correlation tensor imaging

Correlation tensor imaging (CTI) extends the QTI framework outlined above to enable estimation of, in addition to isotropic and anisotropic, microscopic kurtosis (Jespersen et al. 2019; Henriques et al. 2020, 2021). Microscopic kurtosis can stem from, for example, restricted diffusion or cross-sectional variation and has been shown to be important both in the healthy human brain (Novello et al. 2022) and in stroke (Alves et al. 2022). CTI uses a combination of SDE and parallel and orthogonal DDE acquisitions in the long mixing time regime to resolve the three kurtosis sources. The powder-averaged CTI signal representation (Henriques et al. 2021), written to align with the notation of the discussion above (Paper IV), is given by

$$\ln S\left(b, b_\Delta^2, b_\mu^2\right)/S_0 \approx -b\overline{D} + \frac{1}{6}b^2\,\overline{D}^2\left(K_I + b_\Delta^2 K_A + b_\mu^2 K_\mu\right), \tag{38}$$

where $b = b_1 + b_2$ is the total b-value, b_Δ^2 and b_μ^2 are given by

$$b_\Delta^2 = \frac{b_1^2 + b_2^2 + b_1 b_2(3\cos^2\theta - 1)}{(b_1 + b_2)^2} = \begin{cases} 1; & \text{SDE or parallel DDE} \\ \frac{1}{4}; & \text{orthogonal DDE if } b_1 = b_2 \end{cases}, \tag{39}$$

which is in line with the preceding section, and

$$b_\mu^2 = \frac{b_1^2 + b_2^2}{(b_1 + b_2)^2} = \begin{cases} 1; & \text{SDE} \\ \frac{1}{2}; & \text{DDE if } b_1 = b_2 \end{cases}. \tag{40}$$

Thus, K_A is accessed by contrasting parallel and orthogonal DDE acquisitions while K_μ is obtained by contrasting an SDE and a parallel DDE acquisition at the same b-value.

Assuming $b_1 = b_2$, the contrast giving rise to microscopic kurtosis is given by

$$\ln\left(S(b,1,1)\right) - \ln\left(S\left(b,1,\tfrac{1}{2}\right)\right) = \frac{1}{12}b^2\overline{D}^2 K_\mu. \tag{41}$$

The functional form of this contrast is significant for later chapters that will discuss the role of intercompartmental exchange in microscopic kurtosis estimation.

5.2 Restricted and hindered diffusion

The microstructure of biological tissues can be probed with dMRI because the time scales for water molecules to diffuse across typical restriction lengths in tissue are commensurate with the time scales for typical dMRI experiments (10-100 ms) (Price 2009; Reynaud 2017). The relevant timescale for restricted diffusion is set by

$$\zeta = \frac{R^2}{D_0}, \tag{42}$$

where R is the typical restriction length and D_0 is the bulk diffusivity. In complex media such as biological tissue, there is generally no analytical solution for the diffusion equation and thus for the diffusion time-dependence. The diffusion problem simplifies in only two regimes: (i) the short time regime ($t_d \ll \zeta$) where time dependence is governed by the surface-to-volume ratio (Mitra et al. 1993) and (ii) the tortuosity limit ($t_d \gg \zeta$) where diffusion is no longer time-dependent and can be described by a constant diffusion coefficient D_∞ (Price 2009; Callaghan 2011b; Reynaud 2017).

5.2.1 Geometric models and the Gaussian phase approximation

Restricted diffusion is typically described using geometrical models that depict tissue as comprising regular structures such as spheres or cylinders, to facilitate analytical solutions for the diffusion equation. The signal evolution can be described using the multiple propagator formalism introduced earlier (Caprihan et al. 1996; Callaghan 1997; Drobnjak et al. 2010), but such expressions are computationally demanding especially for arbitrary gradient waveforms. More practical models of restricted diffusion are based on the Gaussian Phase Approximation, where they assume that the signal is described fully by the second cumulant (Douglass and McCall 1958; Neuman 1974; Topgaard 2025). Geometric models of restricted diffusion have been used extensively for axon diameter mapping and cell size estimation in both health and disease (Stanisz et al. 1997; Assaf et al. 2004, 2008; Assaf and Basser 2005; Barazany et al. 2009; Alexander et al. 2010; Panagiotaki et al. 2014; Jiang et al. 2016; Reynaud et al. 2016; Veraart et al. 2020; Palombo et al. 2020b).

The general solution for the diffusion equation in bounded media can be written in terms of the eigenfunction expansion (Stepišnik 1993; Callaghan 1995)

$$P(\mathbf{r}_0, \mathbf{r}_1, t) = \sum_k u_k(\mathbf{r}_0) u_k(\mathbf{r}_1) \exp(-a_k D_0 |t|), \tag{43}$$

where u_k are a set of orthogonal spatial eigenfunctions determined by the geometry and a_k are the corresponding eigenvalues. This enables analytical expressions for the diffusion spectrum which facilitates evaluation of the second cumulant according to Eq. 21. For example, for diffusion perpendicular to a cylinder, the diffusion spectrum is given by (Mitra et al. 1992; Stepišnik 1993)

$$D(\omega) = \sum_k B_k \frac{a_k D_0 \omega^2}{a_k^2 D_0^2 + \omega^2} \ , \tag{44}$$

where $B_k = \frac{d^2}{2\mu_k^2(\mu_k^2-1)}$, $a_k = \left(\frac{2\mu_k}{d}\right)^2$ and μ_k is the k$^{\text{th}}$ root of $J_1'(\mu) = 0$ where J_1 is the Bessel function of the first order and kind.

5.2.2 Low-frequency approximation of the diffusion spectrum

The diffusion spectrum in Eq. 44—described by a sum of Lorentzians—can be represented by its low-frequency Taylor series expansion (Stepišnik 1993; Lundell et al. 2019)

$$D(\omega) \approx R\omega^2, \tag{45}$$

where R, referred to as the restriction coefficient (Nilsson et al. 2017) is defined through $R = cd^4/D_0$,where d is the compartment size and c is a constant. The utility of this representation is that it provides a signal equation that factorises the microstructure from the encoding. To illustrate, with the spectrum given in Eq. 45, the signal evaluates to

$$\ln S/S_0 \approx -\frac{1}{2\pi}\int_{-\infty}^{\infty} |Q(\omega)|^2 : R\omega^2 \mathrm{d}\omega = -RbV_\omega \ , \tag{46}$$

where

$$V_\omega = \frac{1}{2\pi b}\int_{-\infty}^{\infty} |Q(\omega)|^2 \, \omega^2 d\omega = \frac{\gamma^2}{b}\int_0^T g^2(t)\mathrm{d}t \, . \tag{47}$$

Notice that while R contains microstructural information, V_ω describes the diffusion encoding—that is, the experiment used to access R. This separation between microstructure and encoding provides insights into how to design the experiment to maximise sensitivity to the microstructure and will be treated in more detail in later chapters.

5.2.3 Hindered diffusion and structural disorder

Hindered diffusion is associated with irregular geometries which makes analytical solutions difficult to derive. A solution, as alluded to earlier in this section, is to resort to extremes where enough coarse-graining has occurred such that global similarity emerges between complex environments that are structurally distinct (Novikov et al. 2014). In a regime approaching the long-time limit, hindered diffusion is described in terms of structural disorder and the diffusion spectrum follows a power law scaling according to (Novikov et al. 2014, 2019; Burcaw et al. 2015; Lee et al. 2020)

$$D(\omega) \approx D_{\infty} + C \cdot Re(i\omega)^{\theta} \quad , \tag{48}$$

where C is a constant, Re denotes real part, and θ is a dynamical exponent reflecting the degree of disorder in the system. Knowledge of the dynamical exponent sheds light on the relevant mesoscopic structures influencing the diffusion-weighted signal. Short-range disorder ($\theta = 1$) is the most common disorder class and gives a linear dependence on frequency (Novikov et al. 2019)

$$D(\omega) \approx D_{\infty} + C \cdot |\omega|. \tag{49}$$

5.3 Exchange

The diffusion problem describing a multicomponent system in exchange is intractable in all but the simplest geometries. Early models of exchange by Tanner (Tanner 1978), von Meerwall and Ferguson (von Meerwall and Ferguson 1981) and later Kuchel and Durrant (Kuchel and Durrant 1999) focused on diffusion restricted by permeable planar layers. Following a different approach, Jiang et al (Jiang et al. 2001) proposed a two-phase exchange model where both pores and the space between them were modelled with spheres and the exchange mechanism was based on the pore-hoping formalism of Callaghan (Callaghan et al. 1992). However, the most well-adopted model of exchange in dMRI—fundamentally different from the above as it is not based on geometrical considerations—was developed by Kärger (Kärger 1985; Kärger et al. 1988) based on a combination of the diffusion equation and the Chapman-Kolmogorov equations for Markov chains. The remainder of this chapter presents the principles of the Kärger model and outlines its prominent derivatives.

5.3.1 The Kärger model

The Kärger model underpins all exchange estimation with dMRI (Fieremans et al. 2010; Nilsson et al. 2010; Moutal et al. 2018; Jelescu et al. 2020, 2022; Olesen et al. 2022; Uhl et al. 2024; Chan et al. 2025). In its basic form, it describes the continuous exchange between two well-mixed isotropic pools of freely diffusing spins (Kärger 1985). The evolution of the signals from the two pools (denoted 1 and 2) is given by the coupled system of differential equations

$$\frac{\partial}{\partial t}\begin{pmatrix} S_1 \\ S_2 \end{pmatrix} = [K - Dq(t)^2]\begin{pmatrix} S_1 \\ S_2 \end{pmatrix}, \tag{50}$$

where K is the matrix of exchange rates given by

$$K = \begin{bmatrix} -k_{12} & k_{21} \\ k_{12} & -k_{21} \end{bmatrix}, \tag{51}$$

where k_{12} is the exchange rate from pool 1 to 2 and vice versa, and D is a diagonal matrix of diffusion coefficients in both environments

$$D = \begin{bmatrix} D_1 & 0 \\ 0 & D_2 \end{bmatrix}. \tag{52}$$

Note that exchange is modelled here as a Poisson process described by a constant rate matrix and the exchange rates obey the detailed balance

$$f_1 k_{12} = f_2 k_{21}, \tag{53}$$

where f_i is the equilibrium fraction of spins in pool i such that $f_1 + f_2 = 1$.

When $q(t)$ is constant in time (which is the case for single diffusion encoding with narrow pulses), the Kärger equations (Eq. 50) can be solved analytically to yield the solution

$$S(q,T)/\mathrm{S}_0 = \mathbf{1} \cdot \exp([K - Dq^2]T) \cdot F, \tag{54}$$

where $\mathbf{1} = [1\ \ 1]$, $F = [f_1\ \ f_2]'$ and T is the total duration of the diffusion encoding gradients. For non-constant $q(t)$, the Kärger equations cannot be solved analytically in closed form and require the multiple propagator approach, as we presented previously (Chakwizira et al. 2021)

$$S(q_i,\ \Delta t, N)/S_0 = \mathbb{1} \cdot \prod_{i=1}^{N} \exp\left(\left[K - Dq_i^2\right]\Delta t\right) \cdot F, \tag{55}$$

where $q(t)$ is discretised into N steps such that $T = N\Delta t$. This equation predicts the effects of exchange on the signal acquired using arbitrary gradient waveforms. However, as noted earlier, the flexibility afforded by this type of discretised solution comes at a cost. Using a coarse temporal resolution (large Δt) introduces numerical errors. A finer resolution gives higher accuracy but drastically increases the computation time due to the large number of matrix exponentials required to evaluate the signal evolution, making the equation impractical for model fitting.

5.3.2 Cumulant expansions for measuring exchange

An alternative, and arguably more intuitive, way of describing the diffusion-weighted signal in exchanging Gaussian pools is based on the cumulant expansion of Eq.54, valid at low b-values (Jensen et al. 2005)

$$\ln(S/S_0) \approx -b \cdot \overline{D} + \frac{1}{2} b^2 \cdot V_D \cdot f(k, \Delta), \tag{56}$$

where $\overline{D} = f_1 D_1 + f_2 D_2$ is the mean diffusivity, $V_D = f_1 f_2 (D_1 - D_2)^2$ is the variance in diffusivities, $k = k_{12} + k_{21}$ is the sum of the forward and reverse exchange rates and

$$f(k, \Delta) = \frac{2}{k\Delta} - \frac{2}{(k\Delta)^2} + \frac{2}{(k\Delta)^2} \mathrm{e}^{-k\Delta} \tag{57}$$

describes the temporal decline in variance due to exchange. The equation above is valid for SDE with narrow pulses. It was generalised by Ning et al. (Ning et al. 2018) to arbitrary gradient waveforms, yielding

$$\ln(S/S_0) \approx -b \cdot \overline{D} + \frac{1}{2} b^2 \cdot V_D \cdot h(k), \tag{58}$$

where $h(k)$ is the generalised exchange-weighting function given by

$$h(k) = 2 \int_0^T \widetilde{q_4}(t) \cdot \exp(-kt)\, \mathrm{d}t, \tag{59}$$

where $\widetilde{q_4}(t) = q_4(t)/b^2$ and

$$q_4(t) = \int_0^T q^2(t')q^2(t'+t)\mathrm{d}t' \tag{60}$$

is the fourth-order autocorrelation function of the dephasing q-vector. If the value of kt is small enough to permit the approximation $\exp(-kt) \approx 1 - kt$, the exchange-weighting function $h(k)$ can be written

$$h(k) \approx (1 - k\Gamma), \tag{61}$$

where

$$\Gamma = 2\int_0^T t\,\widetilde{q_4}(t)\,\mathrm{d}t \tag{62}$$

is the exchange-weighting time. The quantity Γ is, to first order, a measure of the exchange weighting performed by the gradient waveform $g(t)$.

Since the CTI framework discussed in the preceding chapter exploits the contrast between SDE and DDE at a fixed b-value, it is worth noting that the exchange-weighting function for narrow-pulse DDE evaluates to (Ning et al. 2018)

$$h_{DDE}(k, \Delta, t_m) = \frac{1}{2}h_{SDE}(k, \Delta) + \frac{1}{2(k\Delta)^2}\left(\mathrm{e}^{-kt_m} + \mathrm{e}^{-k(2\Delta+t_m)} - 2\mathrm{e}^{-k(\Delta+t_m)}\right). \tag{63}$$

Eq. 58 predicts that, for any given exchange rate, the signal contrast

$$\ln S(b, h_{SDE}) - \ln S(b, h_{DDE}) = \frac{1}{6}b^2\overline{D}^2K_T \cdot (h_{SDE} - h_{DDE}), \tag{64}$$

where $h_{SDE} = f(k, \Delta)$, gives the maximum attainable signal attenuation. That is, exchange sensitivity is driven by the SDE-DDE signal difference at a fixed b-value.

5.3.3 Filter-exchange imaging

Another derivative of the Kärger model is filter-exchange imaging (FEXI) which uses DDE with multiple mixing times to measure exchange (Callaghan and Furó 2004; Åslund et al. 2009; Lasič et al. 2011) (Fig. 4). FEXI has been applied to measure exchange in both the healthy human brain (Nilsson et al. 2013; Bai et al. 2020), in brain tumours (Lampinen et al. 2017b) and with modifications to assess blood-brain

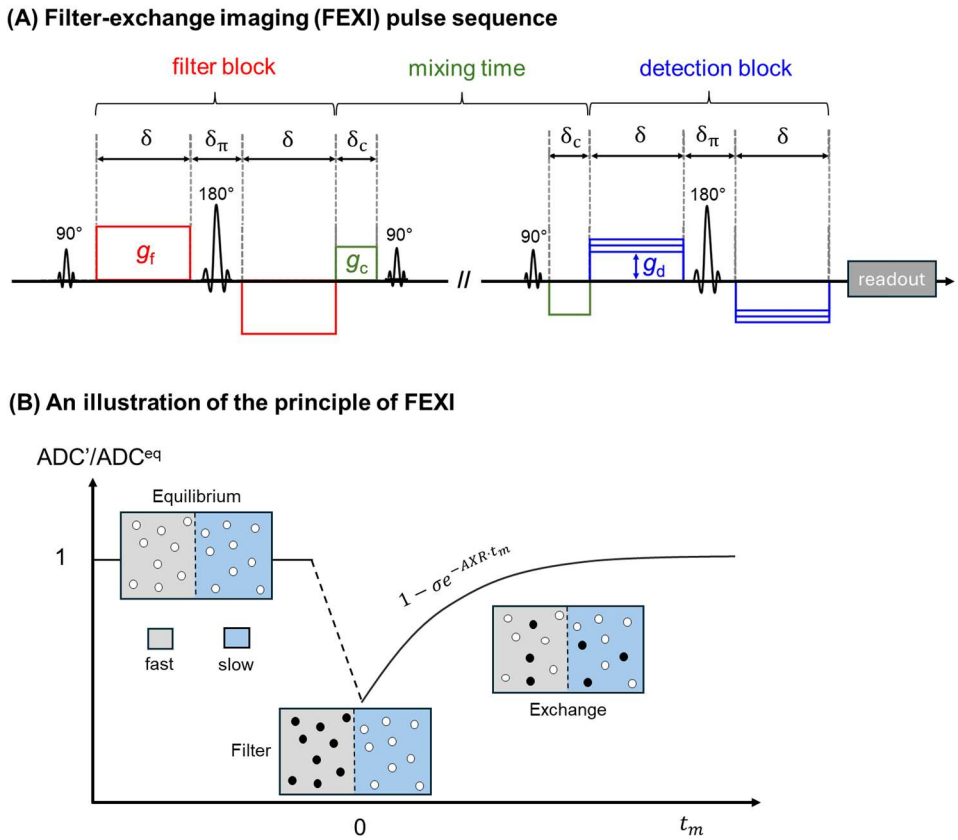

Figure 4. Filter-Exchange Imaging (FEXI). Panel (A) shows the pulse sequence and (B) illustrates the principle. The filter block (red in panel A) perturbs the equilibrium signal fractions by attenuating fast-diffusing spins (panel B), leading to a reduction in the ADC. During the mixing time (t_m), the fractions return to equilibrium at a rate called the apparent exchange rate (AXR). The detection block (blue) is applied with multiple b-values to enable ADC estimation at each mixing time. The AXR is then obtained using Eq. 68. Crusher gradients (green in panel A) are used to eliminate unwanted signal pathways. Note that panel (A) displays the effective gradient waveform incorporating effects of the RF pulses. Subscripts "f", "c" and "d" denote filter, crusher and detection, respectively. δ is the pulse duration in the encoding and filter blocks, δ_π is the pause time and δ_c is the crusher gradient duration. Figure adapted from Paper III, published by John Wiley & Sons Ltd.

barrier permeability in neurodegenerative diseases (Zhang et al. 2023). It considers two tissue components: a slow and a fast, associated with fractions f_S and $f_F = 1 - f_S$ and diffisivities D_S and $D_F > D_S$, respectively. The component fractions are at their equilibrium values (f_S^{eq} and f_F^{eq}) at time zero. The signal at equilibrium is given by

$$S(b) = S_0\left(f_S^{eq} e^{-bD_S} + f_F^{eq} e^{-bD_F}\right) \approx S_0 e^{-b \cdot ADC^{eq}}, \qquad (65)$$

where $ADC^{eq} = f_S^{eq} D_S + f_F^{eq} D_F$. Application of the filter block causes greater signal attenuation in the fast-diffusing pool than in the slow (Fig. 4B), leading to perturbed signal fractions (f_S' and f_F') and a reduction in the ADC. With increasing mixing time, the fractions return to equilibrium following (Lasič et al. 2011)

$$f_S(t_m) = f_S^{eq} + \left(f_S' - f_S^{eq}\right)e^{-AXR \cdot t_m}; \quad f_F(t_m) = 1 - f_S(t_m), \tag{66}$$

where $AXR \approx k$ from the previous chapter. In accordance with Eq. 65 above, the dependence of the signal on the mixing time is given by

$$S(b, t_m) = S_f(t_m)\left(f_S(t_m)e^{-bD_S} + f_F(t_m)e^{-bD_F}\right) \approx S_f(t_m)\mathrm{e}^{-b \cdot ADC'(t_m)}, \tag{67}$$

where $S_f(t_m)$ is the signal in the absence of diffusion encoding gradients (different from S_0 due to diffusion and T2 relaxation in the filter block, as well as T1 relaxation during the mixing time) and

$$ADC'(t_m) = ADC^{eq}[1 - \sigma e^{-AXR \cdot t_m}], \tag{68}$$

where σ is the filter efficiency defined as

$$\sigma = 1 - \frac{ADC'(0)}{ADC^{eq}}, \tag{69}$$

which quantifies the relative ADC reduction at a mixing time of zero.

6 The inverse problem: dissociating entangled contrasts

The diffusion MRI experiment produces signal intensities. The previous chapter elaborated on a plethora of forward modelling approaches that predict the signal given prior knowledge of the microstructure and the experimental setup. The real challenge concerns the inverse problem where, given the signal and the experimental setup, information about the microstructure must be inferred by fitting the model to the signal. A long-standing hardship in this context is that the signal arises from more sources than are captured by the theory, or that the experimental approach conflates multiple sources of contrast. The result is biased estimation and misinterpretation, which hinders dMRI from realising its ambition of becoming a tool for virtual biopsy. Entangled contrasts are commonplace in the field, and this thesis makes no attempt at an exhaustive overview of all. Instead, emphasis is placed on those deemed relevant to most time-dependent dMRI studies, yet still lack an established remedy. Specifically, this chapter will highlight the entanglement between exchange and three other microstructural features: restricted diffusion, anisotropy and intra-compartmental kurtosis.

6.1 Exchange and restricted diffusion

It has been shown previously that restricted diffusion and exchange are entangled in an SDE experiment varying the diffusion time (Nilsson et al. 2009; Olesen et al. 2022). As the diffusion time increases, restrictions cause a reduction in the diffusivity and an increase in kurtosis, leading to an elevated signal. On the contrary, exchange causes an increase in diffusivity (if fast) and a decrease in kurtosis, leading to a decrease in signal. As a result, fast (or non-barrier-limited) exchange which manifests already in the second-order cumulant will bias size estimation if not modelled. Furthermore, restricted diffusion, especially in large confinements, leads to biased exchange estimates by introducing unmodelled time-dependence in the fourth cumulant. This problem was recognised in the past and many solutions have been proposed.

Aiming to account for restricted diffusion, modifications of the Kärger model have been suggested (Pfeuffer et al. 1998; Price et al. 1998; Meier et al. 2003). All are based on replacing the constant diffusion coefficient in one of the spin pools in the Kärger model with a time-dependent variant obtained from analytical solutions for restricted diffusion in impermeable regular geometries (or simply setting the diffusivity to zero under the assumption of long diffusion times). While this solves the problem in the case of narrow pulses where q is constant in time, more general gradient waveforms require signal evaluation via the multiple propagator formalism, where the value of the intracellular diffusivity at every time-point must be considered. A solution to this problem can be obtained via the position autocorrelation function for regular geometries (Chakwizira et al. 2022)

$$\frac{1}{2}\langle\phi^2\rangle = \frac{1}{2}\iint_0^T g(t_1)g(t_2)\,\langle x(t_1)x(t_2)\rangle \mathrm{d}t_1\mathrm{d}t_2 = -b\cdot D_1(\cdot), \qquad (70)$$

where, for example, for a cylindrical geometry, the autocorrelation function is given by (Stepišnik 1993) $\langle x(t_1)x(t_2)\rangle = \sum_{k=0}^{\infty} B_k e^{-a_k D_0|t_1-t_2|}$ where B_k and a_k are as defined earlier (Eq. 44). Discretising Eq. 70 allows the definition of a time-dependent diffusivity compatible with Eq. 55

$$D_1(i) = \frac{1}{2b}\sum_{n=0}^{i} g_n \sum_{m=0}^{i} g_m \sum_{k=0}^{\infty} B_k e^{-a_k D_0|m-n|\Delta t}\,\Delta t\Delta t. \qquad (71)$$

This provides a model predicting the effects of exchange and restricted diffusion on the signal acquired with any gradient waveform. However, the challenges discussed in connection with Eq. 55 for Gaussian diffusion (errors due to coarse discretisation grids and high computational demand for fine grids) apply here as well, if not to a worse degree.

Another approach for separating restricted diffusion and exchange relies on the now well-appreciated phenomenon that the diffusional kurtosis as a function of diffusion time has a non-monotonic behaviour, undergoing a restriction-driven increase at short diffusion times and an exchange-driven decline at longer times. The approach involves collecting dMRI data with multiple diffusion times and fitting the DKI signal representation at each time-point. The Kärger model kurtosis time-dependence (Eq. 57) is then fitted to the kurtosis-vs-diffusion time data to obtain an exchange rate. To minimise the effects of restricted diffusion, the analysis is restricted to a subset of the data for which the mean diffusivity is constant in time and the kurtosis monotonically decreases (Jensen et al. 2005; Li et al. 2023a, 2025; Jensen 2024; Uhl et al. 2024). More

recent work circumvents this sampling approach and derives semi-empirical expressions based on Monte Carlo simulations to describe both the restriction- and exchange-driven temporal dynamics of the kurtosis (Lee et al. 2025).

Effects of restricted diffusion also confound exchange signatures in DEXSY, where joint probability density functions of apparent diffusivities are typically obtained via inverse Laplace transforms under the assumption of Gaussian diffusion (Cai et al. 2018, 2022; Williamson et al. 2020). Solutions to this degeneracy have been proposed by Cai et al. (2022) based on a careful subsampling of DEXSY data, with the most recent approach defining a so-called "Diffusion-Exchange Ratio" enabling joint estimation of both exchange rates and compartment radii (Cai et al. 2024). As will become evident in the next section, their work can be viewed as a special case within the more general framework presented in this thesis.

All contemporary approaches outlined above are based on narrow-pulse SDE or DDE and therefore lack the flexibility of experimental design that is afforded by methods compatible with arbitrary gradient waveforms.

6.1.1 The utility of free gradient waveforms

In Paper I, we used the cumulant expansion to develop a theoretical framework that provides insights on how to design an experiment to maximally separate time-dependent contrasts due to restricted diffusion and exchange. Consider a voxel featuring multiple restricted environments in exchange with an extracellular medium in which diffusion is free. We represent the average diffusion spectrum in each environment by the low-frequency approximation

$$D(\omega) \approx D + R\omega^2, \tag{72}$$

where D and R are constants capturing the time-independent and the time-dependent components of the spectrum, and R is the restriction coefficient defined earlier. Eq. 72 allows the second cumulant to be written

$$\frac{1}{2}o_2 = \frac{1}{2\pi}\int_{-\infty}^{\infty} |Q(\omega)|^2 \, (D + R\omega^2)\mathrm{d}\omega = bD + \, bV_\omega R, \tag{73}$$

where V_ω is the restriction weighting performed by the gradient waveform $g(t)$, as defined earlier (Eq. 47). Averaging over multiple such environments, as done for the Gaussian case in Eq. 31, provides

$$\frac{1}{2}c_2 = \frac{1}{2}\langle o_2 \rangle = bE_D + \, bV_\omega E_R, \tag{74}$$

where "E" denotes average. In the fourth order case, the average cumulant is given by

$$c_4 = \langle o_4 \rangle + 3(\langle o_2^2 \rangle - \langle o_2 \rangle^2) \approx 12b^2\left[V_D + 2V_\omega C_{D,R} + V_\omega^2 V_R\right] \cdot (1 - k\Gamma), \quad (75)$$

where V denotes variance, C denotes covariance, k is the exchange rate and we have assumed that the intra-compartmental term $\langle o_4 \rangle$ is zero. The full signal equation reads

$$\ln(\mathrm{S}/\mathrm{S}_0) \approx -b[E_D + V_\omega E_R] + \frac{1}{2}b^2\left[V_D + 2V_\omega C_{D,R} + V_\omega^2 V_R\right] \cdot (1 - k\Gamma). \quad (76)$$

Eq. 76 describes the dMRI signal in the presence of restricted diffusion and exchange and is compatible with arbitrary gradient waveforms. Notably, as opposed to merely varying the diffusion time in an SDE experiment, this theory provides a way to design a two-dimensional restriction-exchange experiment. We term this framework ResEx (Restriction-Exchange).

As shown in Fig. 5A-B, for a given set of hardware constraints, gradient waveforms span a compact region when plotting the restriction sensitivity against the exchange sensitivity. This region defines the measurement space and is highly governed by the available hardware. In this regard, free waveforms provide a wider measurement space than standard pulsed designs. Numerical simulations from Paper I (Fig. 5C-D) demonstrate the ability of ResEx to separate restriction-driven from exchange-driven signal contrasts. Up to a size of 12 μm, size variations give contrast in the restriction-encoding (3 and 4) but not the exchange-encoding waveforms (1 and 2). Variations in exchange rate give contrast in the exchange-encoding but not the restriction-encoding waveforms.

The ResEx framework also sheds light on the restriction- and exchange-weighting properties of other dMRI methods (Fig. 5II). FEXI—as expected—predominantly encodes exchange. However, note that this is assuming the absence of imaging gradients which may alter the restriction sensitivity of the protocol, as will be discussed in more detail in the next section. OGSE mainly encodes restriction but also exhibits exchange sensitivity. Finally, CTI which leverages the contrast between SDE and DDE to estimate intra-compartmental kurtosis, also bears sensitivity to exchange. This result suggests an interplay between exchange and intra-compartmental kurtosis and will be explored in more detail in a later section.

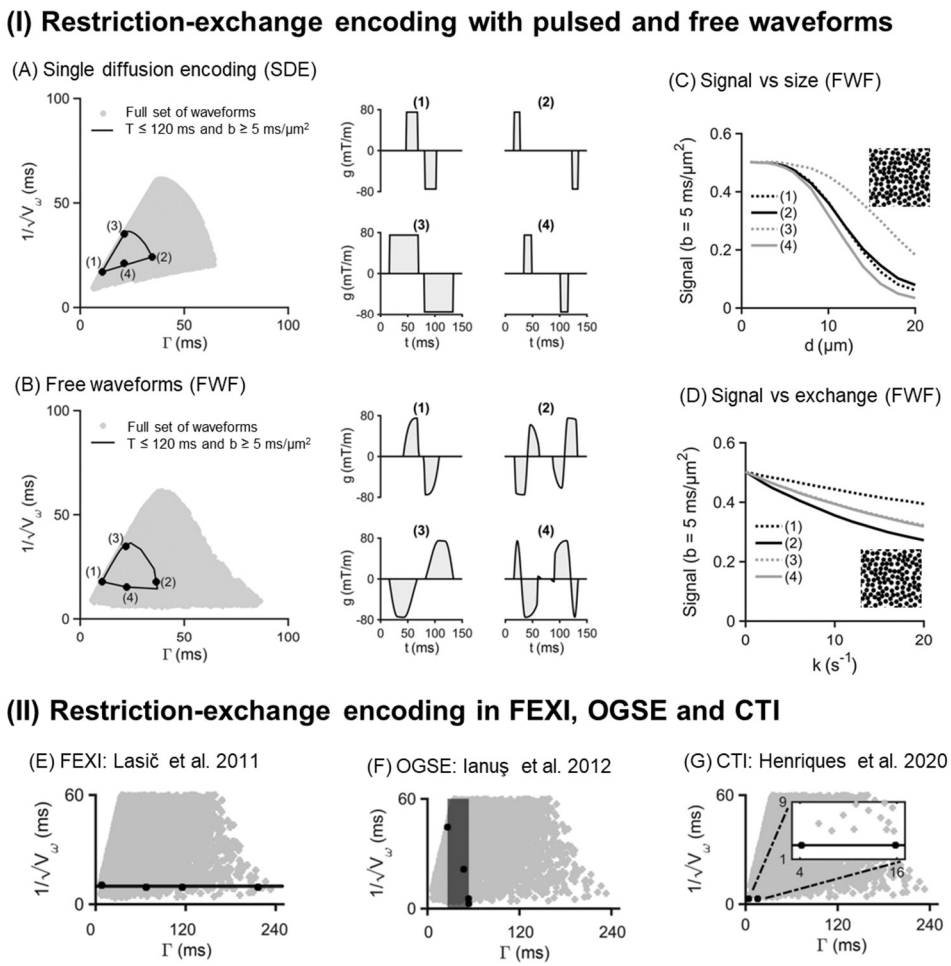

Figure 5. Principle of the ResEx framework. Panels A and B show the restriction-exchange landscape at 80 mT/m and the available measurement space with free waveforms (FWF) and single diffusion encoding (SDE) given constraints of maximum encoding time of 120 ms and minimum b-value of 5 ms/μm^2. FWF gives a wider space than SDE. Monte Carlo simulations (panel C and D) illustrate that the restriction-encoding waveforms (3 and 4) respond to size but not exchange variations, while the opposite is true of the exchange-encoding waveforms (1 and 2). Panel (II) shows the restriction-exchange encoding properties of previous frameworks, where FEXI encodes exchange (panel E), OGSE encodes mainly restriction but also has some exchange sensitivity (panel F) and CTI encodes exchange (panel G). Figure adapted from Paper I, published by John Wiley & Sons Ltd.

In Papers II and VI, we applied the ResEx framework to develop acquisition protocols aimed at probing exchange and restriction in the human brain. The protocol used in Paper VI (Fig. 6A) was tailored for a clinical MRI scanner with a maximum gradient strength of 80 mT/m, and included two waveforms designed to encode exchange (1 and 2), and two to encode restriction (3 and 4). Monte Carlo simulations were used to

verify the ability of the protocol to disentangle signal contrasts arising from exchange and restricted diffusion (Fig. 6B).

For Paper II, we leveraged a high-performance MRI scanner featuring 300 mT/m gradients, enabling the design of a more advanced protocol comprising 150 distinct waveforms with varied sensitivities to restriction and exchange (Fig. 7A). This so-called discovery protocol enabled visualisation of the signal at a fixed b-value in the restriction–exchange landscape. The rationale was that signal variation along the restriction axis would indicate restricted diffusion as the dominant mechanism of time dependence, while variation along the exchange axis would point to exchange as the dominant mechanism. Monte Carlo simulations across a range of substrate sizes and exchange rates (Fig. 7C i and ii) confirmed this hypothesis. Finally, we developed a third protocol for the 300 mT/m system, featuring six waveforms for exchange encoding and six for restriction encoding, specifically designed to enable inversion of the ResEx signal representation (Fig. 7B). This protocol was also validated using numerical simulations where it showed the ability to distinguish exchange- from restriction-driven time-dependence (Fig. 7C iii and iv).

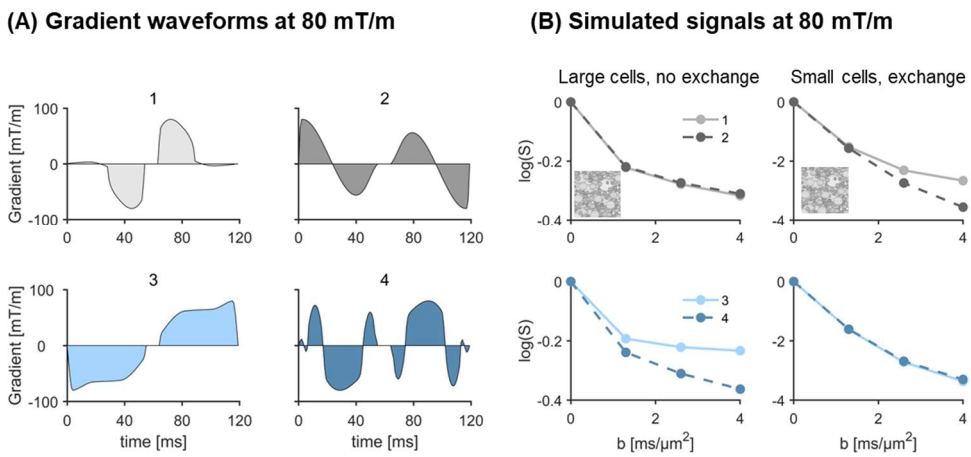

Figure 6. ResEx protocol for in vivo studies at 80 mT/m. Panel (A) shows four waveforms designed for an 80 mT/m scanner, where two are exchange-encoding (1 and 2) and two are restriction-encoding (3 and 4). Simulation results in panel B show—as expected—that the first two waveforms are sensitive to exchange while the other two to restricted diffusion (cell size changes). Figure adapted from Paper VI.

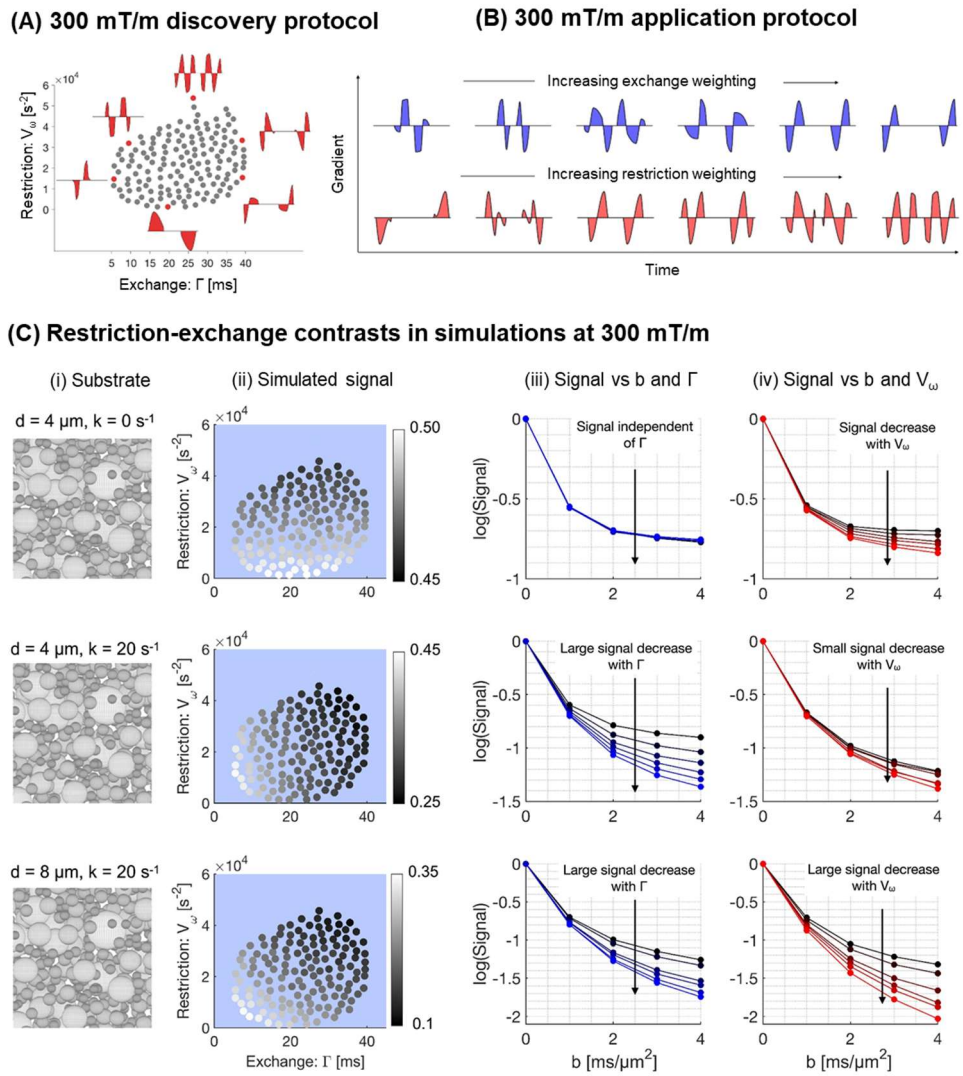

Figure 7. ResEx protocols for in vivo studies at 300 mT/m. Panel A shows the 300 mT/m discovery protocol featuring 150 waveforms spanning the restriction-exchange space. (B) shows waveforms for the 300 mT/m application protocol featuring six exchange-encoding (blue) and six restriction-encoding (red) waveforms. Panel C shows results of numerical simulations using both protocols, in substrates of varying size and exchange rate. For the discovery protocol (ii), visualisation of signals at a fixed b-value in the restriction-exchange landscape shows distinct time-dependence patterns in the different substrates. Restricted diffusion gives signal variation along y-axis, exchange along x-axis and both restriction and exchange give signal variation along the diagonal of the landscape. Note that, to enhance visual appreciation of the trends, five extreme points protruding from the landscape at high restriction weightings are excluded in Panel C (ii). Signal-vs-b curves for the application protocol (iii-iv) also indicate the ability to separate independent contrasts driven by restricted diffusion and exchange. Figure adapted from Paper II, published by Elsevier Inc.

6.1.2 Resolving crusher-induced bias in filter-exchange imaging

As illustrated in the previous section, FEXI, which combines SDE and DDE acquisitions at a fixed diffusion time, isolates effects of exchange from restricted diffusion (Fig. 5E). However, this is true when only the diffusion-encoding gradients are taken into consideration. As shown in Fig. 4, a realistic FEXI pulse sequence also includes crusher gradients meant to eliminate unwanted signal pathways (Lasič et al. 2011). When imaging with thin slices, strong crushers are typically used, and they perform additional diffusion encoding that is not accounted for by the FEXI signal equation. This problem has been solved previously for the case of Gaussian diffusion using matrix exponentials (Lasič et al. 2018; Ohene et al. 2023). However, there was no solution in the case of restricted diffusion until we, in Paper III, proposed a modification of the FEXI pulse sequence to consider the entire gradient waveform (filter, crushers and detection) as a triple diffusion encoding sequence (Fig. 8A). Note that the concept of filter and detection blocks is no longer meaningful in this new approach, and the two blocks are instead collectively referred to as "transverse encoding", to distinguish them from the longitudinal encoding performed by the crushers. Note also that the term "crusher" in this context jointly refers to slice-selective and crusher gradients.

The idea of the new approach was to, when varying the mixing time, increase the exchange weighting (Γ) while keeping the b-value and the restriction weighting (V_ω) fixed. This was achieved by varying both the amplitude and durations of the transverse encoding gradient pulses when the mixing time was changed. The resulting data, no longer compatible with the original FEXI signal equation, were analysed using Eq. 58 with the generalised exchange weighting from (Ning et al. 2018) (equivalently, the ResEx representation without restriction-driven time-dependence). This study is an excellent demonstration of the power and utility of signal equations compatible with arbitrary experimental designs.

We validated the modified FEXI approach (termed "Tuned Exchange Imaging", TEXI) using Monte Carlo simulations in regular structures (spheres and cylinders) in exchange with the extracellular space (Paper III). Figure 8B shows that TEXI performs considerably better than the original FEXI in exchange estimation in the presence of restricted diffusion with strong crusher gradients. TEXI largely removed the dependence of exchange estimates on slice width (crusher gradient strength), yielding more reliable estimates.

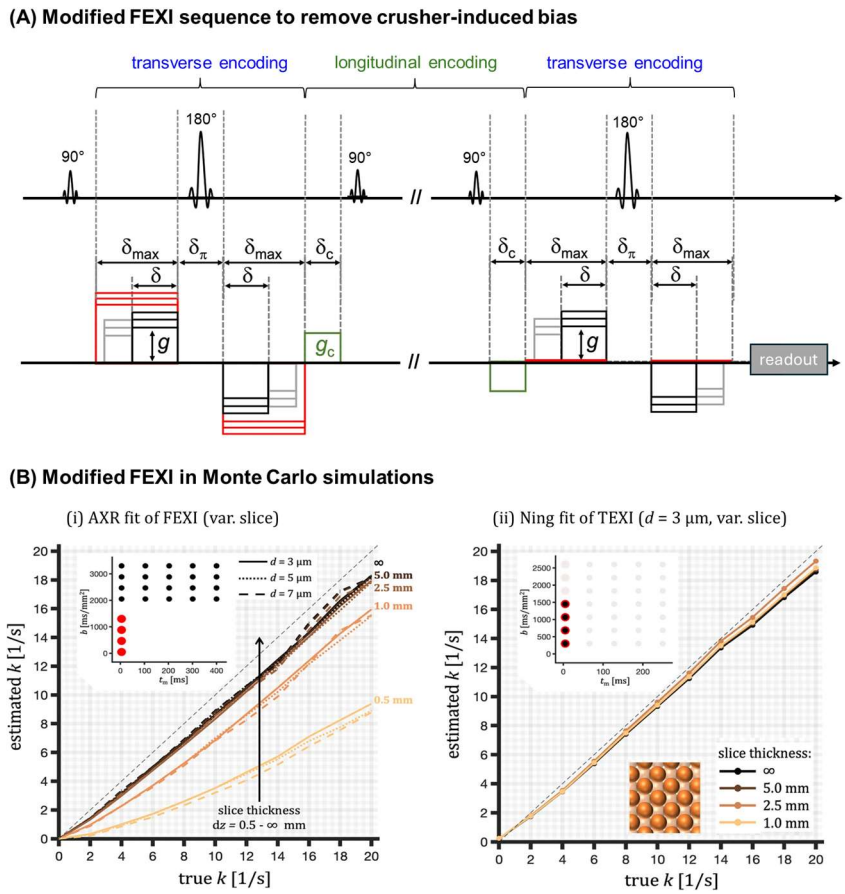

Figure 8. The Tuned Exchange Imaging (TEXI) pulse sequence. Panel A shows the FEXI sequence modified to incorporate the effect of crusher gradients. TEXI uses the same set of RF pulses as FEXI. However, when varying the mixing time, the timing and amplitude of the filter and detection blocks are also varied to keep the restriction sensitivity fixed while increasing the exchange sensitivity. Panel B shows AXR estimates in the original FEXI (i) showing a strong dependence on slice thickness (or crusher strength). TEXI (ii) provides more accurate exchange estimates that are independent of slice thickness. Inserts show b-values and mixing times used for signal generation. Figure adapted from Paper III, published by John Wiley & Sons Ltd.

6.2 Exchange and anisotropy

The directional dependence of exchange in anisotropic brain tissue has been reported in several studies (Sønderby et al. 2014; Ludwig et al. 2021; Li et al. 2022; Shin et al. 2024). This adds a source of variability which increases the challenge of reproducibility and interpretation of *in vivo* exchange estimates with dMRI. Previous work has proposed ways to incorporate anisotropy into exchange estimation. Fieremans et al.

(2010) presented the anisotropic Kärger model based on a tissue model of randomly packed parallel cylinders. Notably, the diffusivity according to the Kärger model remained independent of exchange even in the presence of anisotropy, with anisotropy effects manifesting in higher orders. This anisotropic Kärger model was recently adopted in Neurite Exchange Imaging (Jelescu et al. 2022). More recent work extending the Kärger model to anisotropic diffusion in the Standard Model with Exchange (SMEX) model (Ghazi et al. 2024) reports that incorporating planar tensor encoding in the form of orthogonal DDE adds additional information and removes degeneracies in the model fitting. However, the general knowledge of how to design experiments to disentangle anisotropy from exchange is still limited.

6.2.1 Tensor-valued exchange encoding

In Paper IV, we approached the problem of exchange and anisotropy from a favourite angle—free waveforms. We developed theory that describes exchange between anisotropic Gaussian domains and is compatible with arbitrary gradient waveforms, permitting flexibility of experimental design. This was achieved by extending the 1D multi-Gaussian exchange theory (Eq. 58-62) to a tensorial formulation

$$\ln E \approx -\mathbf{B} : \mathbf{D} + \frac{1}{2}\mathbb{H}(k) : \mathbb{C}^0, \tag{77}$$

where $E = S/S_0$, $\mathbf{D}$ and $\mathbb{C}^0$ are the average diffusion tensor and diffusion tensor covariance of exchanging systems, $\mathbb{H}(k)$ is the exchange-sensitised "square of the b-tensor" defined through

$$\mathbb{H}(k) = 2\int_0^T \mathbb{Q}_4(t)\exp(-kt)\,\mathrm{d}t\,, \tag{78}$$

where $\mathbb{Q}_4(t)$ is the fourth-order autocorrelation tensor of the dephasing q-vector defined through

$$\mathbb{Q}_4(t) = \int_0^T \mathbf{q}^{\otimes 2}(t') \otimes \mathbf{q}^{\otimes 2}(t'+t)\mathrm{d}t'\,. \tag{79}$$

Equation 77 states that, at long enough times, there will be no covariance left. However, a voxel may feature some non-exchanging compartments or comprise a collection of pairwise exchanging components with the pairs themselves not being in exchange with each other. In that case, Eq. 77 reads

$$\ln E \approx -\mathbf{B} : \langle \mathbf{D} \rangle + \frac{1}{2}\mathbb{H}(k) : \mathbb{C}^0 + \tfrac{1}{2}\mathbf{B}^{\otimes 2} : \mathbb{C}^\infty, \tag{80}$$

where $\mathbb{C}^\infty = \langle \mathbf{D}^{\otimes 2} \rangle - \langle \mathbf{D} \rangle^{\otimes 2}$ is the residual covariance that persists despite continuous local exchange. Under the rather strong assumption that all exchanging systems share the same exchange rate, permitting the factorisation $\langle \mathbb{H}(k) : \mathbb{C}^0 \rangle = \mathbb{H}(k) : \langle \mathbb{C}^0 \rangle$, the powder average of Eq. 80 can be expressed

$$\ln E \approx -b\bar{D} + \frac{1}{2}b^2 h(k)\left[V_I^0 + h_\Delta^2(k) V_A^0\right] + \frac{1}{2}b^2\left[V_I^\infty + b_\Delta^2 V_A^\infty\right], \tag{81}$$

where $h(k)$ and $h_\Delta(k)$ are the isotropic and anisotropic projections of $\mathbb{H}(k)$ given by

$$h(k) = (\mathbb{H}(k) : 9\,\mathbb{I}_\mathrm{I})/b^2, \tag{82}$$

and

$$h_\Delta^2(k) = \left(\mathbb{H}(k) : \frac{9}{2}\mathbb{I}_A\right)/b^2 h(k). \tag{83}$$

Eq. 81 can be re-expressed in terms of kurtosis to obtain

$$\ln E \approx -b\bar{D} + \frac{1}{6}b^2 h(k)\bar{D}^2\left[K_I^0 + h_\Delta^2(k) K_A^0\right] + \frac{1}{6}b^2\bar{D}^2\left[K_I^\infty + b_\Delta^2 K_A^\infty\right], \tag{84}$$

which we term MGE (Multi-Gaussian Exchange). This theory is compatible with arbitrary gradient waveforms and does not only account for anisotropy but in fact quantifies it alongside the exchange rate. Noteworthy is that the long-time kurtosis terms, in addition to the mechanisms described earlier, can arise from residual voxel anisotropy due to powder averaging. Neglecting this, as we did in Papers I and II, will lead to a negative bias in the estimated exchange rates. Finally, as with all other dMRI methods that incorporate these terms (Zhang et al. 2021; Jelescu et al. 2022), the ability to estimate them relies on the presence of a temporal dynamic in the kurtosis, that is, exchange must be non-zero.

We evaluated MGE in Paper IV using Monte Carlo simulations in isotropic and anisotropic Gaussian components in exchange (Fig. 9). Signals were generated using the DDE protocol shown in the figure, with variable mixing times from 4 to 300 ms for both parallel and orthogonal DDE. All acquisitions used b-values ranging from 0.25 to 2.5 ms/μm^2. Rician noise was added to all signals at SNR = 200 prior to fitting.

Figure 9 highlights that, despite some bias in the estimation of the isotropic kurtosis, the MGE framework successfully disentangles exchange from anisotropy, and captures the correct exchange rate despite the presence of anisotropy. The fact that all kurtosis sources are largely independent of the exchange rate implies that MGE correctly probes the temporal dynamics of both isotropic and anisotropic components, capturing both

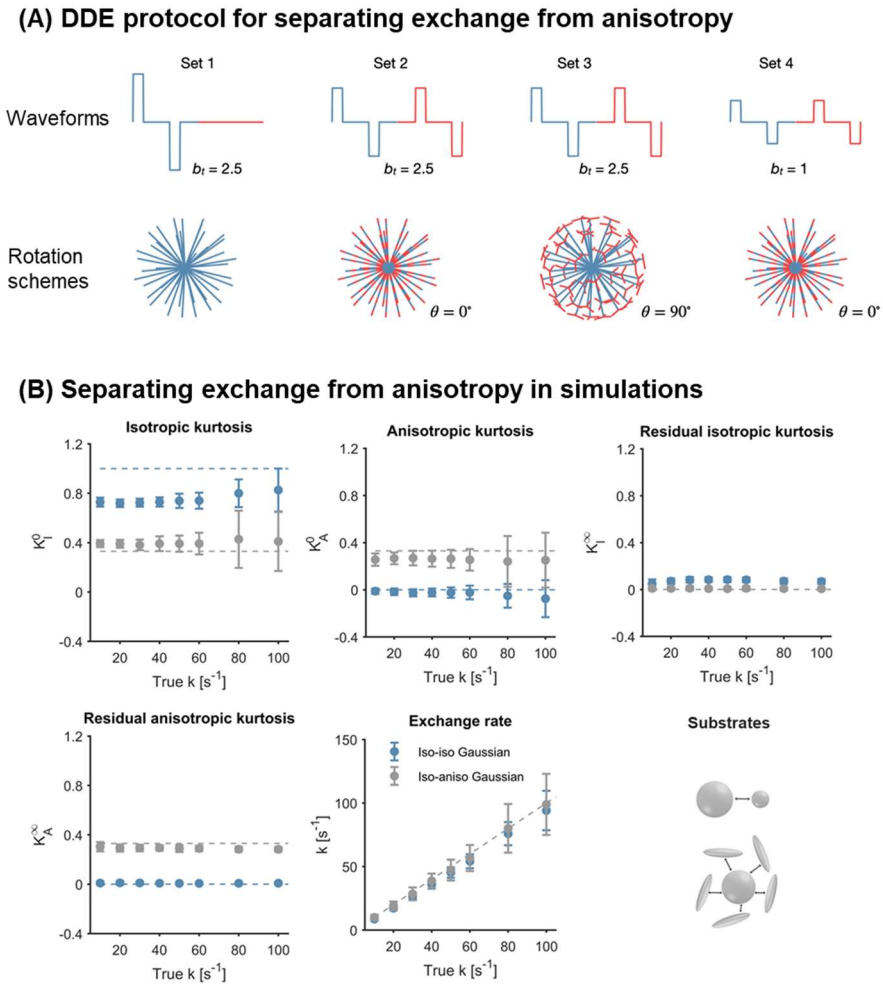

Figure 9. Evaluation of MGE with Monte Carlo simulations. Panel A shows a DDE protocol featuring multiple b-values and rotation schemes. Both parallel and orthogonal DDE acquisitions were performed with varying mixing times from 4 to 300 ms. Panel B shows MGE kurtosis and exchange estimates in substrates of exchanging isotropic and anisotropic Gaussian components. Kurtosis estimates are largely independent of the underlying exchange rate—as expected. Despite the bias in estimation of the isotropic component, kurtosis estimates generally agree with the ground truth. The exchange estimates also show good agreement with ground truth. Overall, MGE enables accurate exchange measurement in the presence of anisotropy. Figure adapted from Paper IV, published by Springer Nature.

the initial kurtosis and the long-time values. While the example shown here used DDE, MGE can be used with any set of gradient waveforms. A theoretical framework incorporating tensor-valued encoding for dissociating isotropic from anisotropic heterogeneity as well as the exchange rate is a powerful tool that we expect to be adopted in future studies.

6.3 Exchange and intra-compartmental kurtosis

Having addressed the problem of exchange in the presence of anisotropy, we proceed to the next hurdle: exchange in the presence of intra-compartmental (or microscopic) kurtosis. None of the exchange theories discussed so far account for this source of kurtosis. In systems well-described by the multi-Gaussian assumption, this is not a concern. However, as has become increasingly evident in recent years, diffusion in heterogeneous media such as biological tissue carries a non-negligible microscopic kurtosis (Henriques et al. 2020, 2021; Alves et al. 2022; Novello et al. 2022). The correlation tensor imaging (CTI) technique enables simultaneous estimation of isotropic, anisotropic, and microscopic kurtoses using a set of SDE and DDE acquisitions in the long mixing time regime. Microscopic kurtosis estimation—a novel contribution of CTI—is achieved using the signal contrast between an SDE and a parallel DDE acquisition at the same b-value (Henriques et al. 2021). In the exchange theories described above, maximum exchange sensitivity comes from this same contrast. This is not in itself a problem from the perspective of CTI, where microscopic kurtosis may have multiple origins, including exchange. However, reliable exchange estimation demands accounting for the additional unmodelled source of diffusional kurtosis. As will become evident in later sections, disentangling exchange from other sources of microscopic kurtosis may also have benefits for microstructure mapping.

The relationship between exchange and microscopic kurtosis can be illustrated by comparing the signal contrasts used to quantify each phenomenon. Equating Eq. 41 and 64 exposes this relationship in the multi-Gaussian setting

$$K_\mu = 2K_T \cdot [h_{SDE}(k, \Delta) - h_{DDE}(k, \Delta, t_m)]. \tag{85}$$

At finite mixing times, Taylor-expanding the right-hand-side of Eq. 85 provides

$$K_\mu = K_T \left(\frac{2}{3}\Delta + t_m\right) k, \tag{86}$$

revealing that microscopic kurtosis outside the long mixing time regime is a growing function of the mixing time, exchange rate and diffusion time. At long mixing times, which is the domain of validity of CTI, one obtains

$$K_\mu(t_m \to \infty) = K_T \cdot h_{SDE}(k, \Delta) \approx K_T \cdot \left(1 - \frac{k\Delta}{3}\right), \tag{87}$$

showing that microscopic kurtosis is a decreasing function of the exchange rate and diffusion time. In the following, we present an approach for dissociating exchange from microscopic kurtosis, as developed in Paper IV.

6.3.1 Dissociating exchange from intra-compartmental kurtosis

We begin by clarifying terminology. The terms "microscopic kurtosis", "intrinsic kurtosis" and "intra-compartmental kurtosis" all refer to the same CTI metric, K_μ, which encompasses effects of intercompartmental exchange as well as an exchange-independent kurtosis component. We refer to this exchange-independent component as "transient kurtosis", alluding to the fact that it is likely short-lived.

Consider a set of non-Gaussian, non-exchanging compartments, each with its individual diffusion and transient kurtosis tensor $\mathbf{D}_j$ and $\mathbf{W}_j$. The powder-averaged signal from one such compartment is given by

$$\ln E \approx -bD_j + \frac{1}{6}b^2{D_j}^2 b_\mu^2 W_j. \tag{88}$$

Taking an average over all such compartments yields the signal equation

$$\ln E \approx -b\overline{D} + \frac{1}{6}b^2\overline{D}^2 b_\epsilon^2 K_\epsilon + \frac{1}{6}b^2\overline{D}^2\left[K_I + b_\Delta^2 K_A\right], \tag{89}$$

where $\overline{D} = \langle D_j \rangle$ is the mean diffusivity, $K_\epsilon = \frac{\langle D_j^2 W_j \rangle}{\overline{D}^2}$ is the average transient kurtosis, $K_I = \frac{3\left(\langle D_j^2 \rangle - \langle D_j \rangle^2\right)}{\overline{D}^2}$ is the isotropic kurtosis and $K_A = \frac{6}{5}\frac{\langle V_\lambda(\mathbf{D}_j)\rangle}{\overline{D}^2}$ is the anisotropic kurtosis. Equation 89 aligns fully with CTI, after setting $K_\epsilon = K_\mu$ and $b_\epsilon = b_\mu$. Consider now slow exchange between the compartments, slow enough for the diffusing spins to spend most of the diffusion encoding time in the same compartment. In other words, barrier-limited exchange. It can be argued that, despite occasional spin migrations between compartments, the picture of distinct compartments remains a good approximation of the system, which entails that the quantity K_ϵ continues to exist, independent of the exchange. The effect of exchange instead manifests in the

intercompartmental kurtosis sources, where it causes a temporal decline described by the rate k according to the MGE framework:

$$\ln E \approx -b\bar{D} + \frac{1}{6}b^2\bar{D}^2 b_\epsilon^2 K_\epsilon + \frac{1}{6}b^2\bar{D}^2 h(k,\Delta,t_m)\left[K_I^0 + h_\Delta^2(k,\Delta,t_m)K_A^0\right]. \quad (90)$$

As discussed in earlier sections, the presence of non-exchanging compartments or residual kurtosis due to powder averaging can be dealt with by incorporating long-time kurtosis sources to obtain

$$\ln E \approx -b\bar{D} + \frac{1}{6}b^2\bar{D}^2 h(k,\Delta,t_m)\left[K_I^0 + h_\Delta^2(k,\Delta,t_m)K_A^0\right] + \frac{1}{6}b^2\bar{D}^2\left[K_I^\infty + b_\Delta^2 K_A^\infty + b_\epsilon^2 K_\epsilon\right]. \quad (91)$$

The signal representation in Eq. 91 is called tMGE (Multi-Gaussian Exchange with transient kurtosis). Inversion of this equation demands data acquired with multiple mixing times for both parallel and orthogonal DDE. The transient kurtosis, K_ϵ, as described above, arises from a process that rapidly reaches the long mixing time regime and is independent of the intercompartmental exchange rate.

In Paper IV, we evaluated tMGE using Monte Carlo simulations. We initially designed a simulation substrate to mimic the premise of tMGE, that is, a transient process that is exchange-independent and a slower exchange-dependent process (Fig. 10). The substate comprised two Gaussian components in rapid exchange with each other (100 s^{-1}, the transient process). The two components were jointly in much slower exchange (1–10 s^{-1}) with a third compartment. Signals were generated using the same DDE protocol used to evaluate MGE (Fig. 9A).

One would anticipate that K_ϵ from tMGE would respond to the fast exchange process while the estimated k responds to the slow exchange process. These trends are precisely what we observed in simulations (Fig. 10). K_ϵ is non-zero and invariant to the 'intercompartmental' exchange while the estimated k grows monotonically. The simulations show that K_μ from CTI is non-zero when k is zero, suggesting that it is sensitive to the fast exchange process. However, as k grows, so does K_μ, indicating that it is also sensitive to the slower process. Note that the isotropic kurtosis from CTI is a function of k, whereas that from tMGE maintains its initial value even as k increases.

We also performed microstructure simulations in substrates of spheres, cylinders and beading structures in exchange with the extracellular space (Fig. 11). While CTI measures a high K_μ as the exchange rate grows, tMGE detects no change in the transient kurtosis, in alignment with the theoretical discussion above.

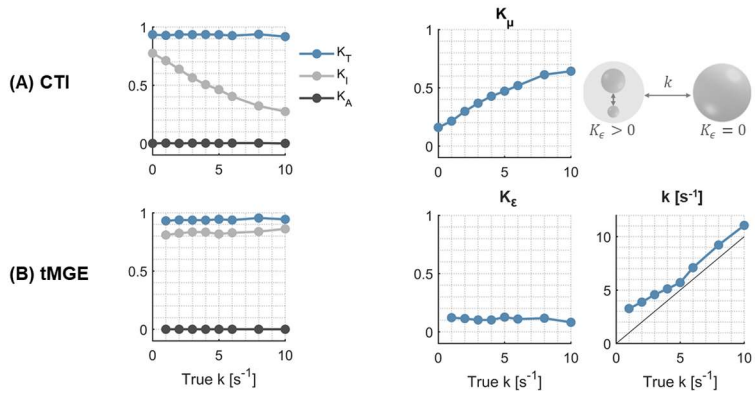

Figure 10. Evaluation of tMGE with Monte Carlo simulations. In a substrate specifically designed to display transient kurtosis, increasing the intercompartmental exchange rate leads to a reduction in isotropic kurtosis estimated with CTI (panel A), accompanied by a corresponding increase in microscopic kurtosis. In contrast, tMGE (panel B) reports a non-zero transient kurtosis that is independent of exchange and captures intercompartmental exchange directly through the exchange rate *k*. Figure adapted from Paper IV, published by Springer Nature.

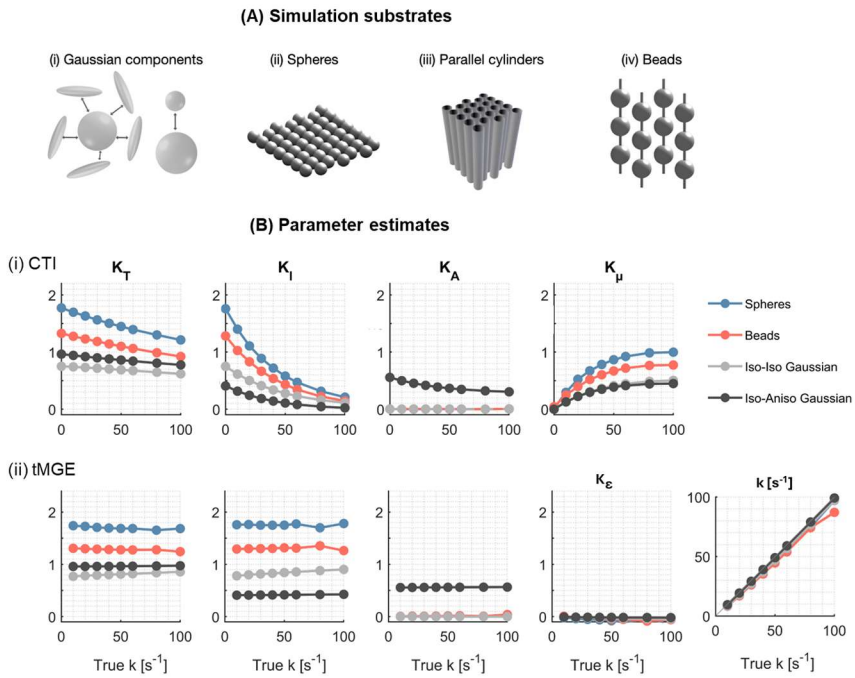

Figure 11. Evaluation of tMGE and CTI with Monte Carlo simulations. Panel A: simulation substrates used: exchanging Gaussian components and spheres, cylinders and beads in exchange with the extracellular space. B(i) CTI parameter estimates, where the total, isotropic and anisotropic kurtosis sources decrease with the underlying exchange rate while the microscopic kurtosis increases. For tMGE (ii), the total, isotropic and anisotropic kurtoses are independent of the exchange rate. The transient kurtosis is invariant to the exchange rate. tMGE exchange estimates agree with the ground truth. Figure adapted from Paper IV, published by Springer Nature.

6.4 Limitations

A critical reflection on the methods presented in this chapter is warranted. A common plague of all three (ResEx, MGE and tMGE) is their foundation in the cumulant expansion, which potentially introduces bias in parameter estimates due to the influence of higher order terms. Remedies for this have been proposed in other contexts (Ianuş et al. 2018), but have not been explored in this work.

Furthermore, the ResEx protocols used in this work are an inefficient probe of restricted diffusion because they require that all waveforms in a protocol attain a set high b-value to probe the time-dependence of the fourth cumulant. However, this significantly reduces the maximum attainable V_ω (since high-V_ω waveforms are oscillatory and thus less efficient), disadvantaging restriction coefficient mapping in the second cumulant. Access to high-performance MRI scanners featuring strong gradients resolves this problem, increasing the maximum attainable V_ω at a given b-value. However, another problem arises. The restriction sensitivity, V_ω, is based on a low-frequency approximation of the diffusion spectrum, which becomes inaccurate at high frequencies, especially when combined with large compartment sizes. The restriction-weighting properties of the gradient waveform are no longer adequately described by V_ω, the so-called "exchange-weighting" waveforms with fixed V_ω begin to exhibit restriction sensitivity and the ResEx framework becomes invalid. Restricted diffusion is best probed by restricting the analysis to the second cumulant and fitting the full diffusion spectrum to circumvent V_ω-related limitations. Note, however, that in using the full spectrum, the factorisation between encoding and microstructure which gives insights on experimental design is lost.

Yet another challenge with ResEx is that it represents the diffusion time-dependence of the second cumulant as driven solely by $V_\omega R$, which is strictly true in a substrate of cells embedded in an MR-invisible medium. In complex media such as biological tissue, time-dependence may also arise from the extracellular space, which is associated with non-quadratic or even non-analytical spectra in the low frequency regime (Novikov et al. 2014). The presence of this unmodelled source of time-dependence complicates the interpretation of R as a "restriction coefficient" and may also propagate errors to the other parameters of the representation.

The weaknesses of ResEx are not restricted to V_ω, but also manifest in the exchange-weighting time Γ, which was defined assuming that $kt \ll 1$. This approximation fails at high exchange rates such as those reported in recent work (Olesen et al. 2022; Uhl et al. 2024; Chan et al. 2025), where ResEx would likely predict a negative diffusional variance. Under these conditions, Γ is no longer enough to describe the exchange-

weighting properties of a given gradient waveform. In analogy to the restriction case, this problem can be solved by fitting the full exchange-weighting function (Eq. 59) and dropping the Γ approximation. Even then, it should be noted that the foundation for the exchange formalism of ResEx is the Kärger model and as such, ResEx is valid for barrier-limited exchange that has no influence on the second cumulant. Non-barrier-limited exchange voids this assumption, possibly leading to biased estimates.

Some limitations unique to the tMGE and MGE frameworks are also worth highlighting. First, like the MGE approach of which it is an extension, tMGE becomes degenerate as the intercompartmental exchange rate k approaches zero, since then the initial kurtosis values become inseparable from their long-time variants (Eq. 91). Furthermore, tMGE successfully separates transient kurtosis from intercompartmental exchange only when the two processes have different correlation times. When this condition is violated, the approach becomes degenerate. Note also that, unlike the MGE theory which is applicable to measurements with arbitrary gradient waveforms, tMGE is currently limited to DDE with narrow pulses. It also remains an open question whether tMGE produces meaningful results in biological tissue under realistic acquisition protocols and SNR.

Finally, as indicated in the opening of this chapter, the methods presented in this thesis address a few entangled contrasts in dMRI but are by no means exhaustive. Other dimensions such as relaxation and flow remain to be explored. Previous work using FEXI or related methods has reported differences in transverse relaxation times between intra- and extracellular compartments as a source of bias in exchange estimation, and some propose solutions based on multi-echo-time acquisitions to enable separation of the two sources of contrast (Eriksson et al. 2017; Powell et al. 2023; Wu et al. 2024). Gradient waveforms used in the methods presented herein, especially ResEx, generally have varying sensitivities to flow, which becomes relevant especially for applications in pathologies that disrupt the blood-brain-barrier (Ahlgren et al. 2016; Szczepankiewicz et al. 2021a; Jalnefjord and Björkman-Burtscher 2024). These avenues will be explored in future work.

7 Interpretation and implications

Previous chapters presented a collection of theoretical and experimental innovations to increase the specificity of time-dependent dMRI by dissociating entangled sources of contrast. In keeping with the overall goal of this thesis work—developing new MRI contrasts based on time-dependent dMRI—this chapter will present initial applications of some of the developed methods in the healthy human brain and in gliomas. The results focus on separating contrasts from exchange and restricted diffusion using free gradient waveforms. The chapter concludes by exploring a promising application: the potential for *in vivo* mapping of dendritic spine density using dMRI.

7.1 Disentangling restriction and exchange in the healthy brain

In Papers I, II and VI, we demonstrated using Monte Carlo simulations that free waveforms designed for selective sensitivity to restricted diffusion and exchange exhibit independent contrasts when cell size and permeability vary. Biological tissue presents an exceedingly more complex substrate than spheres and cylinders. In Paper II, we implemented the discovery and application protocols (Fig. 7) on a high-performance scanner and applied them in four healthy volunteers. The goal was to test if the same contrast patterns observed in simulations (Fig. 7) would also be seen in the brain.

7.1.1 Distinct time-dependence signatures revealed in vivo

The discovery experiment—featuring 150 distinct waveforms—provided a unique tool to probe brain tissue. In the cerebellar cortex (Fig.12) where both restricted diffusion and exchange are expected due to the abundant granule cells, the discovery protocol showed signal variation along both exchange and restriction axes. The internal capsule is predominantly white matter, where restriction effects are expected and limited exchange due to the presence of myelin. Indeed, the discovery protocol showed a signal variation along the restriction axis in this brain region. These trends were corroborated

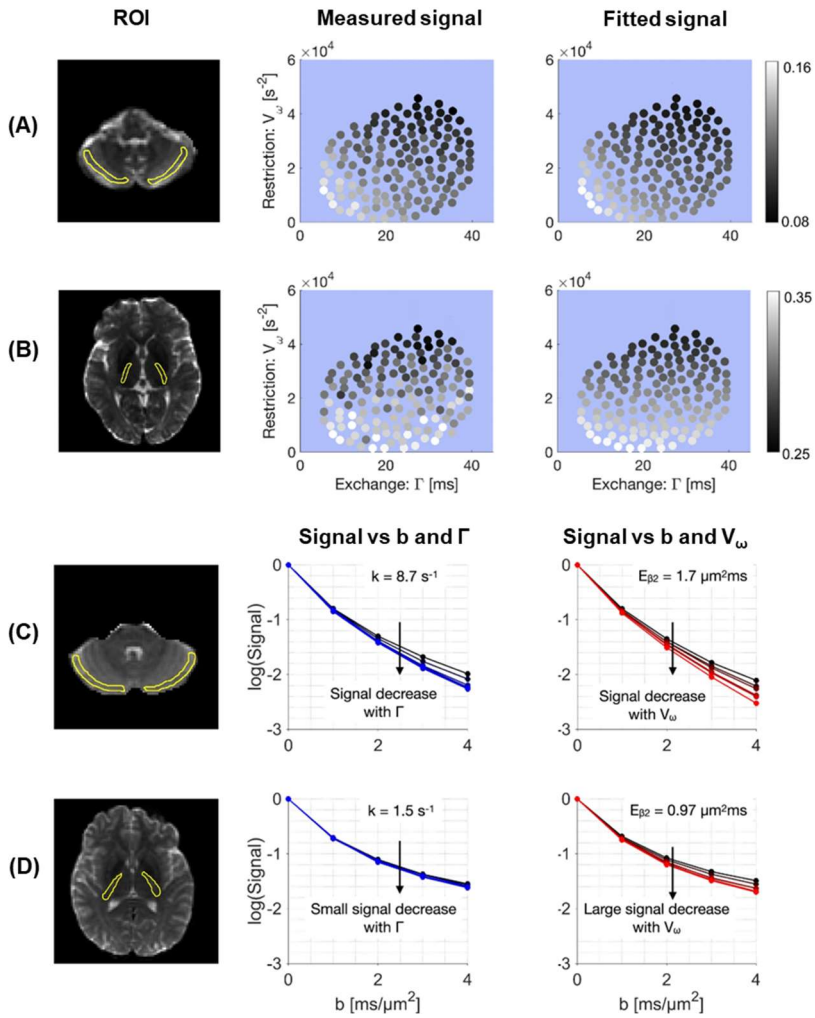

Figure 12. Disentangling restriction and exchange in the human brain. Panels A and B show signals acquired with the 300 mT/m discovery protocol at a b-value of 4 ms/μm^2, plotted in the restriction-exchange landscape. Each dot represents the signal intensity from a unique gradient waveform. In the cerebellar cortex, the signal varies along the diagonal of the landscape, indicating both restriction and exchange contribute to the time-dependence. In the internal capsule, signal variation is along the y-axis, suggesting restriction as the dominant mechanism of time-dependence. Panels C and D show signal-vs-b curves for the application protocol in the cerebellar cortex and internal capsule. The contrast patterns corroborate the results of the discovery protocol. Overall, the ResEx framework separates restriction- from exchange-driven time-dependence in the healthy brain. Figure adapted from Paper II, published by Elsevier Inc.

by the application protocol, whose contrasts in the same brain regions followed a similar pattern. These results suggest that the restriction-exchange parameters reveal distinct and independent time-dependence signatures in the human brain. This demonstrates that we have for the first time an approach for designing arbitrary gradient waveforms

specifically targeting restriction or exchange. The approach is a more flexible alternative to the diffusion time-sampling technique widely used in contemporary work measuring exchange via the kurtosis time dependence (Li et al. 2023a, 2025; Lee et al. 2025).

7.1.2 Mapping restriction and exchange in vivo

As we observed in Paper II, the restriction-exchange framework developed in Paper I allows estimation of restriction- and exchange-related parameters (Fig. 13). Exchange maps exhibited plentiful contrast, with high values indicated in grey matter compared to white matter. These results are in line with previous work reporting slow exchange in white matter due to the influence of myelin (Nilsson et al. 2013; Yang et al. 2018; Brusini et al. 2019; Bai et al. 2020). White matter exchange rates were, however, not zero, indicating some degree of intra-to-extra-axonal transport, likely at the nodes of Ranvier (Fig. 1). Furthermore, the cerebellar cortex featured relatively fast exchange, with exchange times down to 115 ms (computed as the inverse of the exchange rate). This is an interesting result, and it begs the question of what the underlying mechanism for the exchange estimates in grey matter is. Given the highly complex anatomy of the cerebellum as discussed earlier (section 3.1.4), exchange could be arising from water transport across the membranes of the granule cells, or from non-permeative water exchange between different domains of the crowded extracellular space, or between dendritic shafts and spines. Non-permeative (or geometric) exchange has been reported in recent studies (Khateri et al. 2022; Şimşek and Palombo 2024). Sensitivity to different exchange processes may also explain the discrepancy between the grey matter exchange times found in Paper II (115 ms or longer) and those reported in contemporary studies (15 ms or shorter) (Olesen et al. 2022; Jelescu et al. 2022). A later chapter of this thesis will explore this in more detail.

Note that while the exchange maps in Fig. 13 are rich in contrast, the restriction maps are rather featureless, likely due to limited leverage along the restriction-encoding axis. As discussed in section 6.4, the requirement of high b-values limits the measurement space along the restriction axis. Another, perhaps less likely, explanation is the influence of diffusion time-dependence in the extracellular space which is not accounted for by the ResEx signal representation. It should also be mentioned that the restriction maps exhibit a non-physiological anterior-posterior intensity variation, likely due to gradient non-linearities (Fig. 13).

We end on a positive note, remarking that while the data shown in Fig. 13 were acquired with a total scan time of 25 minutes, the acquisition can be down sampled to as little as 4 minutes (Paper II) without significantly degrading the quality of the results. This is important for future clinical applications where time is usually limited.

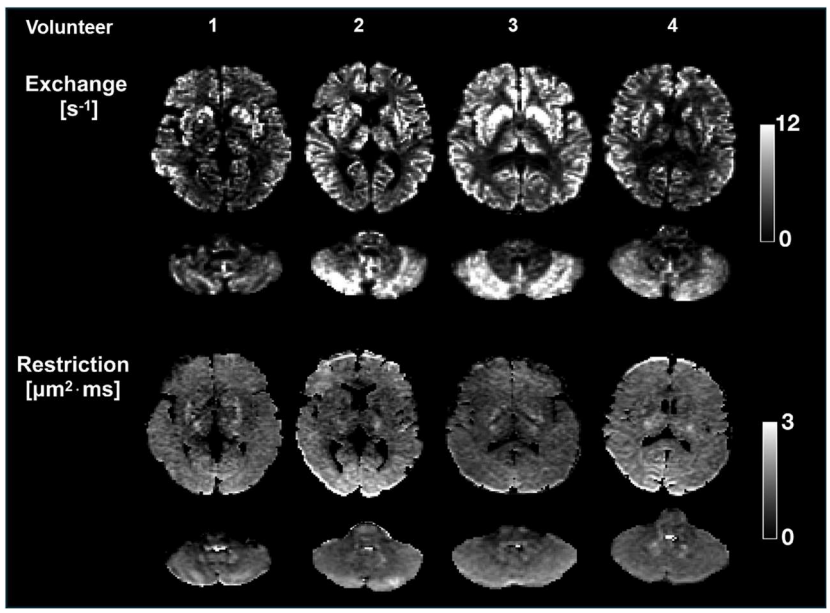

Figure 13. Exchange and restriction mapping in the healthy human brain using ResEx and free waveforms on a 300 mT/m scanner. Results are shown in four volunteers. Exchange maps are rich in contrast and show high values in white matter compared to grey matter. The cerebellar cortex features particularly fast exchange. Restriction maps generally show no contrast except for hyperintense regions around the corticospinal tract and cerebellar nuclei. Figure adapted from Paper II, published by Elsevier Inc.

7.2 Disentangling exchange and restriction in gliomas

Gliomas are the most common primary tumours of the central nervous system and are associated with a disappointing prognosis regardless of the type of intervention used to manage them (Omuro and DeAngelis 2013; Jia et al. 2023). There is growing evidence that the membrane-bound protein AQP4 plays a role in the pathophysiology of gliomas (Nico et al. 2009; Papadopoulos and Verkman 2013; Sun et al. 2020) and is upregulated compared to normal cells (Warth et al. 2005; Maugeri et al. 2016; Montgomery et al. 2020). Elevated AQP4 expression leads to an increase in membrane permeability which can be captured via water exchange measurements with dMRI. Exchange estimation with dMRI may thus improve glioma characterisation by adding complementary information beyond that already accessible with conventional imaging. Exchange in gliomas has been mapped previously using FEXI (Lampinen et al. 2017b) where the AXR was found to be higher in gliomas compared to meningiomas. In Paper

VI, we examined four glioma patients preoperatively on a clinical MRI scanner using a custom pulse sequence and the ResEx protocol shown in Fig. 6A. Due to time constraints, data were acquired using only the two exchange-encoding waveforms (1 and 2) with a total scan time of 5 minutes. Patients were labelled case 1 through 4, with cases 1–3 diagnosed with grade IV glioblastoma while case 4 had an astrocytoma.

7.2.1 Distinct time-dependence signatures revealed in gliomas

Figure 14 shows post-Gadolinium T1-weighted images for the four participants, where pronounced contrast enhancement was observed in cases 1-3 (glioblastoma), but not in case 4 (astrocytoma). Exchange-driven contrasts (signal difference between two

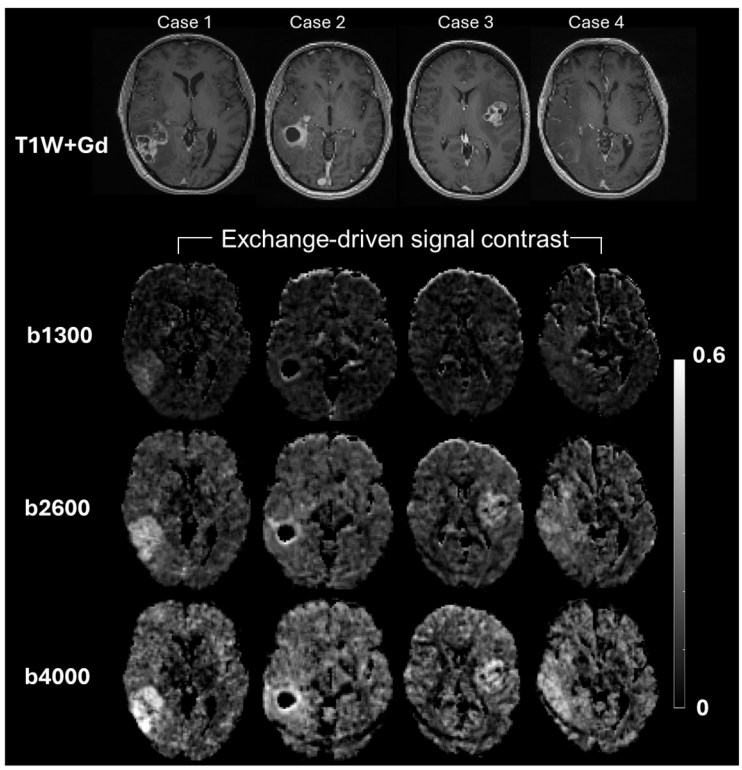

Figure 14. Disentangling restriction and exchange in gliomas. Top row shows post-Gadolinium T1-weighted images of four glioma cases (1 to 3 are glioblastomas and 4 is an astrocytoma). Lower three rows show the signal contrast between the two exchange-encoding waveforms in Fig. 6 (difference scaled by average) at increasing b-values from 1.3 to 4 ms/μm^2. Contrast enhancement is generally associated with high exchange contrast. The tumour core exhibits high exchange contrast in some cases (1) and low in others (2), and judging by the T1-weighted images, this suggests that low exchange is likely related to necrosis. Case 4 presents an interesting finding, where the exchange contrast is high even in the absence of clear Gd contrast enhancement. Note that the U-shaped signal loss in the posterior part of the brain is due to a fat artifact in the diffusion-weighted images. Figure adapted from Paper VI.

exchange-weighting waveforms scaled by their mean) showed sensitivity to the lesions, with increasing conspicuity at higher b-values. This trend suggests that the mechanism driving the contrast is a higher-order effect beyond the apparent diffusion coefficient. In all cases considered, Gd-contrast enhancement was associated with elevated exchange contrast, likely resulting from increased permeability due to either membrane disruption or increased AQP4 expression as referenced above. The tumour core gave negligible exchange effects in cases 2 and 3, possibly due to its necrotic nature, but large effects in others that appeared less necrotic (case 1), indicating that exchange is likely related to the degree of necrosis. In the astrocytoma (case 4), elevated exchange contrast was observed in the left hemisphere, despite the absence of Gd-contrast enhancement. These observations suggest that exchange contrast may reflect microstructural changes not captured by conventional T1-weighted imaging. Remarkably, the discussion so far has only concerned signals, without modelling or parameter estimation, demonstrating the immense utility of the restriction-exchange framework developed in this thesis.

7.2.2 Mapping exchange in gliomas

The exchange contrast patterns in Fig. 14 were corroborated, as expected, by the parameter estimates in Fig. 15. Explorative region-of-interest analyses separately evaluating the oedematous, core and enhancing tumour regions showed that the exchange rate can distinguish between the three microstructures. Furthermore, the analysis revealed distinct patterns for cases 1 and 2: while the core exhibited highest exchange rates in case 1, it had the lowest in case 2. Exchange estimates lay between 0 and 10 s^{-1}, which aligns with *in vivo* measurements from Paper II. Overall, while generalisation from such small samples must be made with caution, we believe that these results illustrate the potential of exchange estimation with dMRI for the characterisation of gliomas.

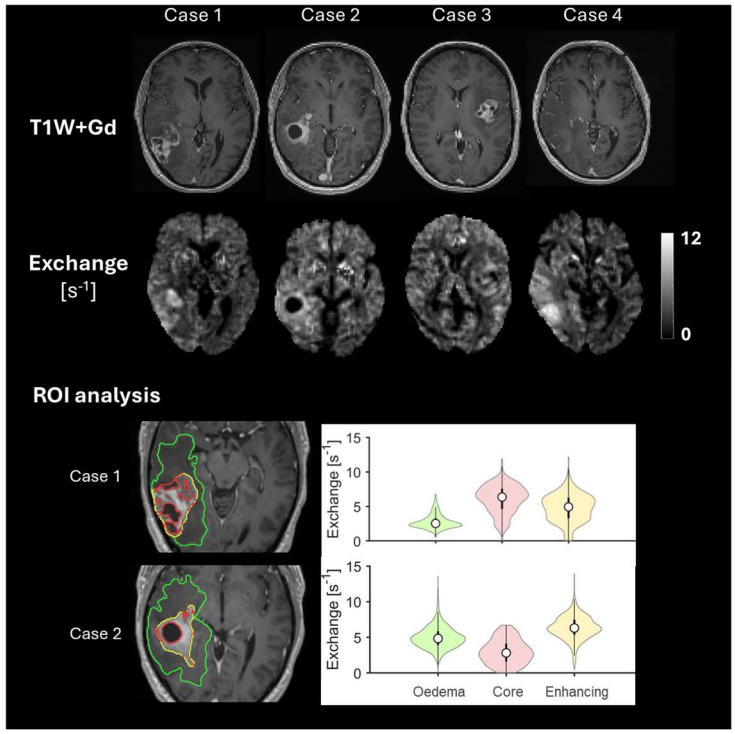

Figure 15. Exchange mapping in gliomas using ResEx with free waveforms on an 80 mT/m system. Top row shows post-Gd T1- weighted images. Exchange maps show similar patterns to those observed in the contrast maps in Fig. 14. ROI analysis focusing on oedema, the core and the enhancing tumour show distinct patterns for the exchange rate in cases 1 and 2. Figure adapted from Paper VI.

7.3 Interpreting in vivo exchange estimates: what are we measuring?

Previous chapters alluded to the challenge of interpreting dMRI exchange estimates in living brain tissue, owing to the multiple potential mechanisms behind the observed contrasts. In Paper V, following previous work (Palombo et al. 2018, 2020a; Chakwizira et al. 2024; Palombo and Şimşek 2024; Şimşek and Palombo 2024), we explored the plausibility of geometric exchange between dendritic shafts and spines as an explanation for grey matter exchange estimates. To this end, synthetic Monte Carlo simulation substrates mimicking dendrites with varying spine densities were designed (Fig. 16) and mixed with extracellular water. The dendrites and spines were made permeable to allow water transport both between shafts and spines (geometric exchange) and between dendrites and the extracellular space (permeative exchange).

Simulated signals were analysed using two diffusion methods: FWF for exchange estimation using ResEx and DDE for microscopic kurtosis estimation using CTI.

7.3.1 Dendritic spines may explain in vivo exchange estimates

We observed that dendritic spines and permeative exchange have opposite effects on the mean diffusivity and kurtosis estimated with both ResEx and CTI: spines reduce the diffusivity and increase kurtosis, while permeative exchange increases diffusivity and reduces kurtosis (Fig. 16). More importantly, both spines and permeative exchange increase ResEx exchange estimates. CTI-estimated intra-compartmental kurtosis also increases with both modes of exchange, since it is based on the same contrast as ResEx. This implies that geometric and permeative exchange imprint the same exchange signature on the signal, making the relationship non-trivial between *in vivo* exchange estimates from dMRI and membrane permeability.

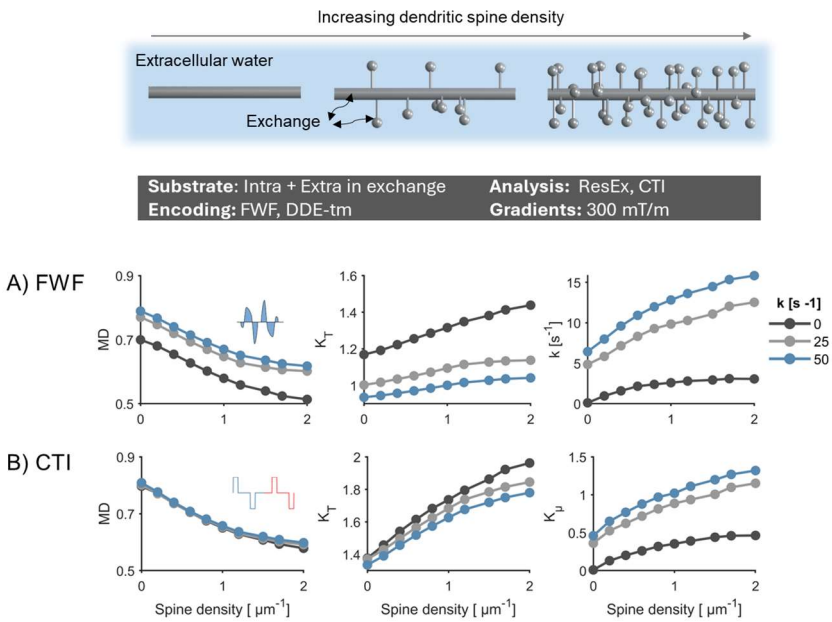

Figure 16. Influence of geometric exchange in dendritic spines on dMRI measures. Results are shown for acquisition protocols designed for a 300 mT/m MRI system. The case $k = 0$ represents diffusion within dendrites mixed with 20% extracellular water, while $k = 25$ and $k = 50$ s^{-1} represent the same configuration with intercompartmental exchange at the respective rates. For FWF (A), mean diffusivity (MD) and kurtosis are shown at the longest simulated Γ. Introducing permeative exchange consistently increases MD, reduces kurtosis, and elevates the measured exchange rate across all spine densities. For CTI (B), MD and total kurtosis are reported from the SDE acquisition. While MD remains largely unaffected by exchange, total kurtosis decreases with increasing k, and microscopic kurtosis reflects sensitivity to both permeative exchange and dendritic spine density. The key takeaway is that diffusion MRI-derived exchange estimates are modulated by both permeative and non-permeative exchange mechanisms. Figure adapted from Paper V.

7.3.2 Diffusion MRI: a potential probe of dendritic spine density

The tMGE framework we developed in Paper IV enables the estimation of an exchange-independent intra-compartmental kurtosis (termed "transient" kurtosis) and the exchange rate, provided that the temporal dynamics of the former proceed on a substantially shorter timescale than the latter. The substrate considered in Fig. 16 potentially satisfies this condition, with the spines providing the cross-sectional variance that gives rise to intra-compartmental kurtosis (Henriques et al. 2021).

We explored this possibility in Paper V and observed that, indeed, tMGE can disentangle geometric contributions from permeative exchange, successfully isolating the two mechanisms (Fig. 17). Notably, transient kurtosis reflected dendritic spine density while remaining insensitive to permeative exchange, whereas the exchange parameter specifically captured permeative exchange and was unaffected by spine density. Note that while the mean diffusivity and total kurtosis also display sensitivity to spine density and insensitivity to the exchange rate (Fig. 17), we anticipate the transient kurtosis to be more specific to spines.

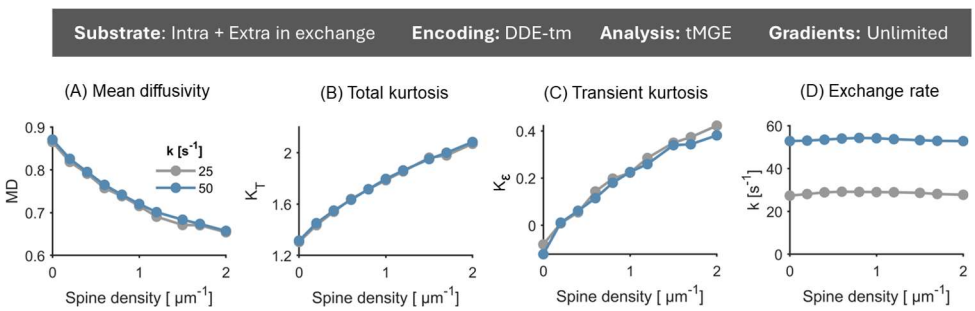

Figure 17. Dissociating permeative from geometric exchange. Simulated signals were generated using a multi–mixing time DDE protocol and analysed using tMGE. The substrate modelled diffusion in dendrites mixed with 20% extracellular water, with intercompartmental exchange rates of k=25 and k=50 s^{-1}. Panels A and B demonstrate that both mean diffusivity (MD) and kurtosis vary with spine density but are unaffected by permeative exchange. Similarly, transient kurtosis (C) increases with spine density yet remains independent of permeative exchange. In contrast, the estimated exchange rate (D) increases with permeative exchange but is insensitive to spine density. These results highlight the potential of tMGE to disentangle the effects of dendritic spines from those of permeative exchange in diffusion MRI. Figure adapted from Paper V.

This finding is particularly exciting: beyond enabling more robust estimates of intercompartmental exchange, tMGE offers a parameter that is selectively sensitive to dendritic spine density. Given that spine density plays a key role in learning, development, and a range of brain disorders (Penzes et al. 2011), the prospect of reliably mapping it non-invasively with dMRI opens up transformative possibilities for neuroscience research and clinical applications.

8 Conclusions and future work

Time-dependent dMRI and the processes giving rise to the observed contrasts are complex. Gaining an understanding of the problem is a multi-step process, and this thesis has paved the way for multiple such steps. From an overarching perspective, this thesis has presented a set of tools—combining both theory and experimental design—to disentangle multiple contrasts: exchange and restricted diffusion, exchange and anisotropy as well as exchange and intra-compartmental kurtosis.

Restricted diffusion and exchange were dissociated by leveraging free gradient waveforms, which allowed the design of experiments selectively sensitive to both phenomena. The approach—implemented on a high-performance MRI scanner—successfully separated restriction- from exchange-driven contrasts in the healthy brain and enabled independent estimation of parameters related to both. Applications in gliomas on a clinical MRI system revealed substantial exchange-driven contrasts in the lesions, indicating potential for tumour characterisation. Furthermore, the approach proved capable of resolving imaging-gradient-induced biases in FEXI, enabling more reliable AXR estimation.

Finally, to decipher the mechanisms underlying *in vivo* exchange estimates, the interplay between dendritic spine-driven geometric exchange and permeative exchange was numerically investigated. The results indicate that both geometric and permeative exchange influence dMRI exchange estimates. An approach to separate the two effects was proposed, yielding unconfounded estimates of permeative exchange as well as a method for potentially mapping spine density.

The conclusions from each contribution included in this thesis were as follows:

I. Restricted diffusion and exchange are disentangled using theory accounting for both phenomena and compatible with free gradient waveforms. The restriction- and exchange-encoding properties of any waveform can be described by scalar quantities, providing a method for designing protocols to separate the two effects. Free waveforms provide a wider restriction-exchange measurement space than SDE, but the space is heavily limited by hardware.

II. The ResEx framework with free waveforms isolates distinct contrasts driven by restriction and exchange in the healthy human brain. Exchange is faster in grey matter than in white matter. Exchange is particularly fast in the cerebellar cortex, hinting at non-permeative transport mechanisms.

III. AXR estimation with FEXI suffers crusher gradient-induced bias in the presence of restricted diffusion, when imaging using thin slices. Based on ResEx, FEXI was successfully adjusted by varying the pulse timings to keep the restriction sensitivity fixed when varying the mixing time, to remove the bias.

IV. Intra-compartmental kurtosis as measured by CTI is sensitive to both the transient kurtosis and intercompartmental exchange. Theory accounting for both, combined with multiple-mixing time DDE data, separates the two. The theory also allows exchange estimation in the presence of anisotropy.

V. Geometric exchange between dendritic shafts and spines has the same imprint on the dMRI signal as permeative exchange. An approach to separate them using DDE with multiple mixing times was proposed. Simulations indicate the ability to map dendritic spine density independent of permeative exchange.

VI. The ResEx framework reveals notable exchange-driven contrasts in gliomas on a clinical scanner, capturing both inter-tumoural and intra-tumoural heterogeneity. Exchange potentially adds information beyond that accessible with conventional imaging.

In conclusion, this thesis presents a powerful set of techniques to interrogate brain tissue and extract specific and biologically meaningful information. Combined with the emerging high-performance MRI scanners, these advancements position us well for the future of microstructure imaging with dMRI.

Future work will explore *in vivo* dendritic spine mapping with dMRI and its potential applications in neurodegenerative and neuropsychiatric diseases. Additionally, further studies on gliomas using a high-performance MRI scanner will be conducted to better understand the role of exchange in glioma pathology.

Acknowledgements

I want to first thank my supervisors Markus Nilsson, Filip Szczepankiewicz, and Linda Knutsson. It has been a privilege to work with you. Markus, thank you for your tireless support and seemingly endless insights that have been so valuable for me throughout my PhD journey. Filip, you are a legend; thank you for your thoroughness, guidance and friendship. Linda, you inspire me; thank you for your mentorship and for being there when I needed your advice.

Next, I would like to thank Ronnie Wirestam. You introduced me to the world of MRI with your world-class lectures and it has always been a pleasure to work with you. Crister Ceberg, thank you for your great supervision when I took an interest in medical physics. Katarina Sjögreen Gleisner, thank you for your support during my PhD.

I'm very grateful to all my co-authors and collaborators. Special thanks to Ante Zhu and Tom Foo for the collaboration on our MAGNUS work (and for hosting me in Niskayuna), C-F Westin for your support and mentorship, Marco Palombo and Kadir Şimşek for an enjoyable collaboration, Samo Lasič for talks about all things MRI and beyond, Alexis Reymbaut for fun with autocorrelation functions, Pia Sundgren for your central role in our clinical research, and Frederik Testud for your support.

Many thanks to the MR Physics group at Lund University, including past and present colleagues. Linda Wennberg for help with our clinical studies, Titti Owman for the venue for my defence, Ivan Rashid for your magic with the Alienware, Malwina Molendowska for your friendship and support, Sajad Mohammed Ali for being a brother, Björn Lampinen for friendly discussions, Lara Langensee and Geraline Vis for fun coffee breaks, Jimmy Lätt, Cornelia Säll, Jan Brabec, João de Almeida Martins, Theodor Rumetshofer, Anina Seidemo, Anna Lundberg and everyone else.

I also want to thank my beautiful family: my daughters Amanda and Alicia, my son Alex Michael and my lovely and supportive wife, Andrea. You have always managed to put a smile on my face even in the toughest of times. Thank you.

Finally, and most importantly, I want to thank God. At the end of the day, *all* my achievements are credited to You. Thank You for the gift of nature, whose beautiful complexity grants us the joy of scientific inquiry.

References

Aboitiz, F., Scheibel, A.B., Fisher, R.S. & Zaidel, E. 1992. Fiber composition of the human corpus callosum. Brain Research. 598(1): 143–153.

Agre, P. & Kozono, D. 2003. Aquaporin water channels: molecular mechanisms for human diseases. FEBS letters. 555(1): 72–78.

Ahlgren, A., Knutsson, L., Wirestam, R., Nilsson, M., Ståhlberg, F., Topgaard, D. & Lasič, S. 2016. Quantification of microcirculatory parameters by joint analysis of flow-compensated and non-flow-compensated intravoxel incoherent motion (IVIM) data. NMR in Biomedicine. 29(5): 640–649.

Albers, G.W. 1999. Expanding the window for thrombolytic therapy in acute stroke. The potential role of acute MRI for patient selection. Stroke. 30(10): 2230–2237.

Alexander, D.C., Dyrby, T.B., Nilsson, M. & Zhang, H. 2019. Imaging brain microstructure with diffusion MRI: practicality and applications. NMR in Biomedicine. 32(4): e3841.

Alexander, D.C., Hubbard, P.L., Hall, M.G., Moore, E.A., Ptito, M., Parker, G.J.M. & Dyrby, T.B. 2010. Orientationally invariant indices of axon diameter and density from diffusion MRI. NeuroImage. 52(4): 1374–1389.

Allen, N.J. & Lyons, D.A. 2018. Glia as Architects of Central Nervous System Formation and Function. Science (New York, N.Y.). 362(6411): 181–185.

Alves, R., Henriques, R.N., Kerkelä, L., Chavarrías, C., Jespersen, S.N. & Shemesh, N. 2022. Correlation Tensor MRI deciphers underlying kurtosis sources in stroke. NeuroImage. 247: 118833.

Andersen, K.W., Lasič, S., Lundell, H., Nilsson, M., Topgaard, D., Sellebjerg, F., Szczepankiewicz, F., Siebner, H.R., Blinkenberg, M. & Dyrby, T.B. 2020. Disentangling white-matter damage from physiological fibre orientation dispersion in multiple sclerosis. Brain Communications. 2(2): fcaa077.

Åslund, I., Nowacka, A., Nilsson, M. & Topgaard, D. 2009. Filter-exchange PGSE NMR determination of cell membrane permeability. Journal of Magnetic Resonance. 200(2): 291–295.

Assaf, Y. & Basser, P.J. 2005. Composite hindered and restricted model of diffusion (CHARMED) MR imaging of the human brain. NeuroImage. 27(1): 48–58.

Assaf, Y., Blumenfeld-Katzir, T., Yovel, Y. & Basser, P.J. 2008. Axcaliber: A method for measuring axon diameter distribution from diffusion MRI. Magnetic Resonance in Medicine. 59(6): 1347–1354.

Assaf, Y., Freidlin, R.Z., Rohde, G.K. & Basser, P.J. 2004. New modeling and experimental framework to characterize hindered and restricted water diffusion in brain white matter. Magnetic Resonance in Medicine. 52(5): 965–978.

Bączyńska, E., Pels, K.K., Basu, S., Włodarczyk, J. & Ruszczycki, B. 2021. Quantification of Dendritic Spines Remodeling under Physiological Stimuli and in Pathological Conditions. International Journal of Molecular Sciences. 22(8): 4053.

Badaut, J., Ashwal, S., Adami, A., Tone, B., Recker, R., Spagnoli, D., Ternon, B. & Obenaus, A. 2011. Brain water mobility decreases after astrocytic aquaporin-4 inhibition using RNA interference. Journal of Cerebral Blood Flow & Metabolism. 31(3): 819–831.

Bai, R., Li, Z., Sun, C., Hsu, Y.-C., Liang, H. & Basser, P. 2020. Feasibility of filter-exchange imaging (FEXI) in measuring different exchange processes in human brain. NeuroImage. 219: 117039.

Bai, R., Springer Jr., C.S., Plenz, D. & Basser, P.J. 2018. Fast, Na+/K+ pump driven, steady-state transcytolemmal water exchange in neuronal tissue: A study of rat brain cortical cultures. Magnetic Resonance in Medicine. 79(6): 3207–3217.

Barazany, D., Basser, P.J. & Assaf, Y. 2009. In vivo measurement of axon diameter distribution in the corpus callosum of rat brain. Brain. 132(5): 1210–1220.

Basser, P.J., Mattiello, J. & LeBihan, D. 1994. MR diffusion tensor spectroscopy and imaging. Biophysical Journal. 66(1): 259–267.

Basser, P.J. & Pajevic, S. 2003. A normal distribution for tensor-valued random variables: applications to diffusion tensor MRI. IEEE Transactions on Medical Imaging. 22(7): 785–794.

Beaulieu, C. 2002. The basis of anisotropic water diffusion in the nervous system - a technical review. NMR in biomedicine. 15(7–8): 435–455.

Borgnia, M., Nielsen, S., Engel, A. & Agre, P. 1999. Cellular and Molecular Biology of the Aquaporin Water Channels. Annual Review of Biochemistry. 68(Volume 68, 1999): 425–458.

Brabec, J., Friedjungová, M., Vašata, D., Englund, E., Bengzon, J., Knutsson, L., Szczepankiewicz, F., Westen, D. van, Sundgren, P.C. & Nilsson, M. 2023. Meningioma microstructure assessed by diffusion MRI: An investigation of the source of mean diffusivity and fractional anisotropy by quantitative histology. NeuroImage : Clinical. 37: 103365.

Braitenberg, V. & Schüz, A. 1998. *Cortex: Statistics and Geometry of Neuronal Connectivity*. Berlin, Heidelberg: Springer.

Brusini, L., Menegaz, G. & Nilsson, M. 2019. Monte Carlo Simulations of Water Exchange Through Myelin Wraps: Implications for Diffusion MRI. IEEE transactions on medical imaging. 38(6): 1438–1445.

Burcaw, L.M., Fieremans, E. & Novikov, D.S. 2015. Mesoscopic structure of neuronal tracts from time-dependent diffusion. NeuroImage. 114: 18–37.

Cai, T.X., Benjamini, D., Komlosh, M.E., Basser, P.J. & Williamson, N.H. 2018. Rapid detection of the presence of diffusion exchange. Journal of Magnetic Resonance. 297: 17–22.

Cai, T.X., Williamson, N.H., Ravin, R. & Basser, P.J. 2022. Disentangling the Effects of Restriction and Exchange With Diffusion Exchange Spectroscopy. Frontiers in Physics. 10.

Cai, T.X., Williamson, N.H., Ravin, R. & Basser, P.J. 2024. The Diffusion Exchange Ratio (DEXR): A minimal sampling of diffusion exchange spectroscopy to probe exchange, restriction, and time-dependence. Journal of Magnetic Resonance. 366: 107745.

Cajal, S.R. 1924. *Estructura de los centros nerviosos de las aves (1888)*. Jiménez y Molina.

Callaghan, P.T. 1991. *Principles of Nuclear Magnetic Resonance Microscopy*. Oxford: Oxford University Press.

Callaghan, P.T. 1995. Pulsed-Gradient Spin-Echo NMR for Planar, Cylindrical, and Spherical Pores under Conditions of Wall Relaxation. Journal of Magnetic Resonance, Series A. 113(1): 53–59.

Callaghan, P.T. 1997. A Simple Matrix Formalism for Spin Echo Analysis of Restricted Diffusion under Generalized Gradient Waveforms. Journal of Magnetic Resonance. 129(1): 74–84.

Callaghan, P.T. 2011a. *Translational Dynamics and Magnetic Resonance: Principles of Pulsed Gradient Spin Echo NMR*. OUP Oxford.

Callaghan, P.T. 2011b. Restricted diffusion. Translational Dynamics and Magnetic Resonance: Principles of Pulsed Gradient Spin Echo NMR, 0. Oxford University Press.

Callaghan, P.T., Coy, A., Halpin, T.P.J., MacGowan, D., Packer, K.J. & Zelaya, F.O. 1992. Diffusion in porous systems and the influence of pore morphology in pulsed gradient spin-echo nuclear magnetic resonance studies. The Journal of Chemical Physics. 97(1): 651–662.

Callaghan, P.T. & Furó, I. 2004. Diffusion-diffusion correlation and exchange as a signature for local order and dynamics. The Journal of Chemical Physics. 120(8): 4032–4038.

Callaghan, P.T. & Komlosh, M.E. 2002. Locally anisotropic motion in a macroscopically isotropic system: displacement correlations measured using double pulsed gradient spin-echo NMR. Magnetic Resonance in Chemistry. 40(13): S15–S19.

Caprihan, A., Wang, L.Z. & Fukushima, E. 1996. A Multiple-Narrow-Pulse Approximation for Restricted Diffusion in a Time-Varying Field Gradient. Journal of Magnetic Resonance, Series A. 118(1): 94–102.

Catani, M., Howard, R.J., Pajevic, S. & Jones, D.K. 2002. Virtual in vivo interactive dissection of white matter fasciculi in the human brain. NeuroImage. 17(1): 77–94.

Chakwizira, A., Lasič, S., Reymbaut, A., Westin, C.-F., Szczepankiewicz, F. & Nilsson, M. 2022. Characterisation of restricted diffusion and exchange using the velocity autocorrelation function. London, UK.

Chakwizira, A., Şimşek, K., Palombo, M., Szczepankiewicz, F., Knutsson, L. & Nilsson, M. 2024. Water exchange as measured by diffusion MRI with free gradient waveforms: A potential biomarker of dendritic spine morphology. Proceedings of ISMRM. Singapore.

Chakwizira, A., Szczepankiewicz, F., Knutsson, L. & Nilsson, M. 2021. Probing restricted diffusion and water exchange with free gradient waveforms: Addressing the need for a compartment model. Proceedings of ISMRM.

Chan, K.-S., Ma, Y., Lee, H., Marques, J.P., Olesen, J.L., Coelho, S., Novikov, D.S., Jespersen, S.N., Huang, S.Y. & Lee, H.-H. 2025. In vivo human neurite

exchange time imaging at 500 mT/m diffusion gradients. Imaging Neuroscience.

Chen, L., Liu, M., Bao, J., Xia, Y., Zhang, J., Zhang, L., Huang, X. & Wang, J. 2013. The Correlation between Apparent Diffusion Coefficient and Tumor Cellularity in Patients: A Meta-Analysis. PLOS ONE. 8(11): e79008.

Chenevert, T.L., Stegman, L.D., Taylor, J.M., Robertson, P.L., Greenberg, H.S., Rehemtulla, A. & Ross, B.D. 2000. Diffusion magnetic resonance imaging: an early surrogate marker of therapeutic efficacy in brain tumors. Journal of the National Cancer Institute. 92(24): 2029–2036.

Clark, D.L., Boutros, N.N. & Mendez, M.F. 2010. *The Brain and Behavior: An Introduction to Behavioral Neuroanatomy*. Cambridge University Press.

Coelho, S., Pozo, J.M., Jespersen, S.N., Jones, D.K. & Frangi, A.F. 2019. Resolving degeneracy in diffusion MRI biophysical model parameter estimation using double diffusion encoding. Magnetic Resonance in Medicine. 82(1): 395–410.

Consalez, G.G., Goldowitz, D., Casoni, F. & Hawkes, R. 2021. Origins, Development, and Compartmentation of the Granule Cells of the Cerebellum. Frontiers in Neural Circuits. 14.

Cory, D.G. 1990. Measurement of translational displacement probabilities by NMR: An indicator of compartmentation. Magnetic Resonance in Medicine. 14(3): 435–444.

Crank, J. 1975. *The Mathematics of Diffusion*. Oxford: Oxford University Press.

Does, M.D., Parsons, E.C. & Gore, J.C. 2003. Oscillating gradient measurements of water diffusion in normal and globally ischemic rat brain. Magnetic Resonance in Medicine. 49(2): 206–215.

Douglass, D.C. & McCall, D.W. 1958. Diffusion in Paraffin Hydrocarbons. The Journal of Physical Chemistry. 62(9): 1102–1107.

Drobnjak, I., Siow, B. & Alexander, D.C. 2010. Optimizing gradient waveforms for microstructure sensitivity in diffusion-weighted MR. Journal of Magnetic Resonance. 206(1): 41–51.

Duffy, D.G. 2001. *Green's Functions with Applications*. Boca Raton, Fla: Chapman and Hall/CRC.

Edgar, J.M. & Griffiths, I.R. 2009. Chapter 5 - White Matter Structure: A Microscopist's View. Diffusion MRI, 74–103. San Diego: Academic Press.

Eriksson, S., Elbing, K., Söderman, O., Lindkvist-Petersson, K., Topgaard, D. & Lasič, S. 2017. NMR quantification of diffusional exchange in cell suspensions with relaxation rate differences between intra and extracellular compartments. PLOS ONE. 12(5): e0177273.

Eriksson, S., Lasič, S., Nilsson, M., Westin, C.-F. & Topgaard, D. 2015. NMR diffusion-encoding with axial symmetry and variable anisotropy: Distinguishing between prolate and oblate microscopic diffusion tensors with unknown orientation distribution. The Journal of Chemical Physics. 142(10): 104201.

Fan, Q., Eichner, C., Afzali, M., Mueller, L., Tax, C.M.W., Davids, M., Mahmutovic, M., Keil, B., Bilgic, B., Setsompop, K., Lee, H.-H., Tian, Q., Maffei, C., Ramos-Llordén, G., Nummenmaa, A., Witzel, T., Yendiki, A., Song, Y.-Q., Huang, C.-C., Lin, C.-P., Weiskopf, N., Anwander, A., Jones, D.K., Rosen, B.R., Wald, L.L. & Huang, S.Y. 2022. Mapping the human connectome using diffusion MRI at 300 mT/m gradient strength: Methodological advances and scientific impact. NeuroImage. 254: 118958.

Fan, Q., Nummenmaa, A., Witzel, T., Zanzonico, R., Keil, B., Cauley, S., Polimeni, J.R., Tisdall, D., Van Dijk, K.R.A., Buckner, R.L., Wedeen, V.J., Rosen, B.R. & Wald, L.L. 2014. Investigating the Capability to Resolve Complex White Matter Structures with High b-Value Diffusion Magnetic Resonance Imaging on the MGH-USC Connectom Scanner. Brain Connectivity. 4(9): 718–726.

Fick, A. 1855. Ueber Diffusion. Annalen der Physik. 170(1): 59–86.

Fieremans, E., Burcaw, L.M., Lee, H.-H., Lemberskiy, G., Veraart, J. & Novikov, D.S. 2016. In vivo observation and biophysical interpretation of time-dependent diffusion in human white matter. NeuroImage. 129: 414–427.

Fieremans, E., Jensen, J.H. & Helpern, J.A. 2011. White matter characterization with diffusional kurtosis imaging. NeuroImage. 58(1): 177–188.

Fieremans, E., Novikov, D.S., Jensen, J.H. & Helpern, J.A. 2010. Monte Carlo study of a two-compartment exchange model of diffusion. NMR in biomedicine. 23(7): 711–724.

Foo, T.K.F., Tan, E.T., Vermilyea, M.E., Hua, Y., Fiveland, E.W., Piel, J.E., Park, K., Ricci, J., Thompson, P.S., Graziani, D., Conte, G., Kagan, A., Bai, Y., Vasil, C., Tarasek, M., Yeo, D.T.B., Snell, F., Lee, D., Dean, A., DeMarco, J.K., Shih, R.Y., Hood, M.N., Chae, H. & Ho, V.B. 2020. Highly efficient head-only magnetic field insert gradient coil for achieving simultaneous high gradient amplitude and slew rate at 3.0T (MAGNUS) for brain microstructure imaging. Magnetic Resonance in Medicine. 83(6): 2356–2369.

Galbán, C.J., Hoff, B.A., Chenevert, T.L. & Ross, B.D. 2017. Diffusion MRI in early cancer therapeutic response assessment. NMR in biomedicine. 30(3).

Ghazi, N., Coelho, S., Shemesh, N. & Jespersen, S.N. 2024. Tensor encoded diffusion weighting improves model parameter estimation of SMEX/NEXI. Proceedings of the ISMRM. Singapore.

Goveas, J., O'Dwyer, L., Mascalchi, M., Cosottini, M., Diciotti, S., De Santis, S., Passamonti, L., Tessa, C., Toschi, N. & Giannelli, M. 2015. Diffusion-MRI in neurodegenerative disorders. Magnetic Resonance Imaging. 33(7): 853–876.

Grebenkov, D.S. 2007. Multiple correlation function approach: rigorous results for simple geometries. Diffusion Fundamentals. 5.

Hahn, E.L. 1950. Spin Echoes. Physical Review. 80(4): 580–594.

Henriques, R.N., Jespersen, S.N. & Shemesh, N. 2020. Correlation tensor magnetic resonance imaging. NeuroImage. 211: 116605.

Henriques, R.N., Jespersen, S.N. & Shemesh, N. 2021. Evidence for microscopic kurtosis in neural tissue revealed by correlation tensor MRI. Magnetic Resonance in Medicine. 86(6): 3111–3130.

Hildebrand, C., Remahl, S., Persson, H. & Bjartmar, C. 1993. Myelinated nerve fibres in the CNS. Progress in Neurobiology. 40(3): 319–384.

Horsfield, M.A., Barker, G.J. & McDonald, W.I. 1994. Self-diffusion in CNS tissue by volume-selective proton NMR. Magnetic Resonance in Medicine. 31(6): 637–644.

Howes, O.D., Cummings, C., Chapman, G.E. & Shatalina, E. 2023. Neuroimaging in schizophrenia: an overview of findings and their implications for synaptic changes. Neuropsychopharmacology. 48(1): 151–167.

Huang, S.Y., Witzel, T., Keil, B., Scholz, A., Davids, M., Dietz, P., Rummert, E., Ramb, R., Kirsch, J.E., Yendiki, A., Fan, Q., Tian, Q., Ramos-Llordén, G., Lee, H.-H., Nummenmaa, A., Bilgic, B., Setsompop, K., Wang, F., Avram, A.V., Komlosh, M., Benjamini, D., Magdoom, K.N., Pathak, S., Schneider, W., Novikov, D.S., Fieremans, E., Tounekti, S., Mekkaoui, C., Augustinack, J., Berger, D., Shapson-Coe, A., Lichtman, J., Basser, P.J., Wald, L.L. & Rosen, B.R. 2021. Connectome 2.0: Developing the next-generation ultra-high gradient strength human MRI scanner for bridging studies of the micro-, meso- and macro-connectome. NeuroImage. 243: 118530.

Hui, E.S., Fieremans, E., Jensen, J.H., Tabesh, A., Feng, W., Bonilha, L., Spampinato, M.V., Adams, R. & Helpern, J.A. 2012. Stroke assessment with diffusional kurtosis imaging. Stroke. 43(11): 2968–2973.

Ianuş, A., Jespersen, S.N., Serradas Duarte, T., Alexander, D.C., Drobnjak, I. & Shemesh, N. 2018. Accurate estimation of microscopic diffusion anisotropy and its time dependence in the mouse brain. NeuroImage. 183: 934–949.

Jackson, R.J., Fuller, G.N., Abi-Said, D., Lang, F.F., Gokaslan, Z.L., Shi, W.M., Wildrick, D.M. & Sawaya, R. 2001. Limitations of stereotactic biopsy in the initial management of gliomas. Neuro-Oncology. 3(3): 193–200.

Jalnefjord, O. & Björkman-Burtscher, I.M. 2024. Comparison of methods for intravoxel incoherent motion parameter estimation in the brain from flow-compensated and non-flow-compensated diffusion-encoded data. Magnetic Resonance in Medicine. 92(1): 303–318.

Jelescu, I.O., Palombo, M., Bagnato, F. & Schilling, K.G. 2020. Challenges for biophysical modeling of microstructure. Journal of Neuroscience Methods. 344: 108861.

Jelescu, I.O., Skowronski, A. de, Geffroy, F., Palombo, M. & Novikov, D.S. 2022. Neurite Exchange Imaging (NEXI): A minimal model of diffusion in gray matter with inter-compartment water exchange. NeuroImage. 256: 119277.

Jelescu, I.O., Veraart, J., Fieremans, E. & Novikov, D.S. 2016a. Degeneracy in model parameter estimation for multi-compartmental diffusion in neuronal tissue. NMR in biomedicine. 29(1): 33–47.

Jelescu, I.O., Zurek, M., Winters, K.V., Veraart, J., Rajaratnam, A., Kim, N.S., Babb, J.S., Shepherd, T.M., Novikov, D.S., Kim, S.G. & Fieremans, E. 2016b. In vivo quantification of demyelination and recovery using compartment-specific diffusion MRI metrics validated by electron microscopy. NeuroImage. 132: 104–114.

Jensen, J.H. 2024. Diffusional kurtosis time dependence and the water exchange rate for the multi-compartment Kärger model. Magnetic Resonance in Medicine. 91(3): 1122–1135.

Jensen, J.H. & Helpern, J.A. 2010. MRI quantification of non-Gaussian water diffusion by kurtosis analysis. NMR in biomedicine. 23(7): 698–710.

Jensen, J.H., Helpern, J.A., Ramani, A., Lu, H. & Kaczynski, K. 2005. Diffusional kurtosis imaging: The quantification of non-gaussian water diffusion by means

of magnetic resonance imaging. Magnetic Resonance in Medicine. 53(6): 1432–1440.

Jespersen, S.N., Bjarkam, C.R., Nyengaard, J.R., Chakravarty, M.M., Hansen, B., Vosegaard, T., Østergaard, L., Yablonskiy, D., Nielsen, N.C. & Vestergaard-Poulsen, P. 2010. Neurite density from magnetic resonance diffusion measurements at ultrahigh field: comparison with light microscopy and electron microscopy. NeuroImage. 49(1): 205–216.

Jespersen, S.N., Kroenke, C.D., Østergaard, L., Ackerman, J.J.H. & Yablonskiy, D.A. 2007. Modeling dendrite density from magnetic resonance diffusion measurements. NeuroImage. 34(4): 1473–1486.

Jespersen, S.N., Lundell, H., Sønderby, C.K. & Dyrby, T.B. 2013. Orientationally invariant metrics of apparent compartment eccentricity from double pulsed field gradient diffusion experiments. NMR in Biomedicine. 26(12): 1647–1662.

Jespersen, S.N., Olesen, J.L., Hansen, B. & Shemesh, N. 2018. Diffusion time dependence of microstructural parameters in fixed spinal cord. NeuroImage. 182: 329–342.

Jespersen, S.N., Olesen, J.L., Ianuş, A. & Shemesh, N. 2019. Effects of nongaussian diffusion on "isotropic diffusion" measurements: An ex-vivo microimaging and simulation study. Journal of Magnetic Resonance. 300: 84–94.

Jia, Y., Xu, S., Han, G., Wang, B., Wang, Z., Lan, C., Zhao, P., Gao, M., Zhang, Y., Jiang, W., Qiu, B., Liu, R., Hsu, Y.-C., Sun, Y., Liu, C., Liu, Y. & Bai, R. 2023. Transmembrane water-efflux rate measured by magnetic resonance imaging as a biomarker of the expression of aquaporin-4 in gliomas. Nature Biomedical Engineering. 7(3): 236–252.

Jiang, X., Devan, S.P., Xie, J., Gore, J.C. & Xu, J. 2022. Improving MR cell size imaging by inclusion of transcytolemmal water exchange. NMR in Biomedicine. 35(12): e4799.

Jiang, R., Du, F.-Z., He, C., Gu, M., Ke, Z.-W. & Li, J.-H. 2014. The value of diffusion tensor imaging in differentiating high-grade gliomas from brain metastases: a systematic review and meta-analysis. PloS One. 9(11): e112550.

Jiang, X., Li, H., Xie, J., McKinley, E.T., Zhao, P., Gore, J.C. & Xu, J. 2017. In vivo imaging of cancer cell size and cellularity using temporal diffusion spectroscopy. Magnetic resonance in medicine. 78(1): 156–164.

Jiang, X., Li, H., Xie, J., Zhao, P., Gore, J.C. & Xu, J. 2016. Quantification of cell size using temporal diffusion spectroscopy. Magnetic Resonance in Medicine. 75(3): 1076–1085.

Jiang, P.C., Yu, T.Y., Perng, W.C. & Hwang, L.P. 2001. Pore-to-pore hopping model for the interpretation of the pulsed gradient spin echo attenuation of water diffusion in cell suspension systems. Biophysical Journal. 80(6): 2493–2504.

Jones, D.K. 2010. *Diffusion MRI*. Oxford University Press.

Kampen, N.G. van. 2007. *Stochastic Processes in Physics and Chemistry*. Amsterdam ; Boston: Elsevier.

Kandel, E.R. 2013. *Principles of Neural Science, Fifth Edition*. McGraw Hill Professional.

Kärger, J. 1985. NMR self-diffusion studies in heterogeneous systems. Advances in Colloid and Interface Science. 23: 129–148.

Kärger, J., Pfeifer, H. & Heink, W. 1988. Principles and Application of Self-Diffusion Measurements by Nuclear Magnetic Resonance. Advances in Magnetic and Optical Resonance, 1–89. Academic Press.

Khateri, M., Reisert, M., Sierra, A., Tohka, J. & Kiselev, V.G. 2022. What does FEXI measure? NMR in Biomedicine. 35(12): e4804.

Kiselev, V. 2010. The Cumulant Expansion: An Overarching Mathematical Framework For Understanding Diffusion NMR.

Kiselev, V.G. 2017. Fundamentals of diffusion MRI physics. NMR in Biomedicine. 30(3): e3602.

Koch, M.A. & Finsterbusch, J. 2011. Towards compartment size estimation in vivo based on double wave vector diffusion weighting. NMR in biomedicine. 24(10): 1422–1432.

Kuchel, P.W. & Durrant, C.J. 1999. Permeability Coefficients from NMR q-Space Data: Models with Unevenly Spaced Semi-permeable Parallel Membranes. Journal of Magnetic Resonance. 139(2): 258–272.

Lampinen, B., Szczepankiewicz, F., Mårtensson, J., Westen, D. van, Hansson, O., Westin, C.-F. & Nilsson, M. 2020a. Towards unconstrained compartment modeling in white matter using diffusion-relaxation MRI with tensor-valued diffusion encoding. Magnetic Resonance in Medicine. 84(3): 1605–1623.

Lampinen, B., Szczepankiewicz, F., Mårtensson, J., Westen, D. van, Sundgren, P.C. & Nilsson, M. 2017a. Neurite density imaging versus imaging of microscopic anisotropy in diffusion MRI: A model comparison using spherical tensor encoding. NeuroImage. 147: 517–531.

Lampinen, B., Szczepankiewicz, F., Westen, D. van, Englund, E., C Sundgren, P., Lätt, J., Ståhlberg, F. & Nilsson, M. 2017b. Optimal experimental design for filter exchange imaging: Apparent exchange rate measurements in the healthy brain and in intracranial tumors. Magnetic Resonance in Medicine. 77(3): 1104–1114.

Lampinen, B., Zampeli, A., Björkman-Burtscher, I.M., Szczepankiewicz, F., Källén, K., Compagno Strandberg, M. & Nilsson, M. 2020b. Tensor-valued diffusion MRI differentiates cortex and white matter in malformations of cortical development associated with epilepsy. Epilepsia. 61(8): 1701–1713.

Lasic, S., Jespersen, S.N., Lundell, H., Nilsson, M., Dyrby, T.B. & Topgaard, D. 2016. Apparent Exchange Rate in Multi-compartment Anisotropic Tissue. Proceedings of the ISMRM. Singapore.

Lasič, S., Lundell, H., Topgaard, D. & Dyrby, T.B. 2018. Effects of imaging gradients in sequences with varying longitudinal storage time-Case of diffusion exchange imaging. Magnetic Resonance in Medicine. 79(4): 2228–2235.

Lasič, S., Nilsson, M., Lätt, J., Ståhlberg, F. & Topgaard, D. 2011. Apparent exchange rate mapping with diffusion MRI. Magnetic Resonance in Medicine. 66(2): 356–365.

Lasič, S., Oredsson, S., Partridge, S.C., Saal, L.H., Topgaard, D., Nilsson, M. & Bryskhe, K. 2016. Apparent exchange rate for breast cancer characterization. NMR in Biomedicine. 29(5): 631–639.

Lätt, J., Nilsson, M., Westen, D. van, Wirestam, R., Ståhlberg, F. & Brockstedt, S. 2009. Diffusion-weighted MRI measurements on stroke patients reveal water-exchange mechanisms in sub-acute ischaemic lesions. NMR in Biomedicine. 22(6): 619–628.

Lawrenz, M., Koch, M.A. & Finsterbusch, J. 2010. A tensor model and measures of microscopic anisotropy for double-wave-vector diffusion-weighting experiments with long mixing times. Journal of Magnetic Resonance. 202(1): 43–56.

Le Bihan, D. 2003. Looking into the functional architecture of the brain with diffusion MRI. Nature Reviews. Neuroscience. 4(6): 469–480.

Le Bihan, D., Breton, E., Lallemand, D., Grenier, P., Cabanis, E. & Laval-Jeantet, M. 1986. MR imaging of intravoxel incoherent motions: application to diffusion and perfusion in neurologic disorders. Radiology. 161(2): 401–407.

Le Bihan, D., Mangin, J.F., Poupon, C., Clark, C.A., Pappata, S., Molko, N. & Chabriat, H. 2001. Diffusion tensor imaging: concepts and applications. Journal of magnetic resonance imaging: JMRI. 13(4): 534–546.

Lebel, C. & Deoni, S. 2018. The Development of Brain White Matter Microstructure. NeuroImage. 182: 207–218.

Lee, H.-H., Fieremans, E. & Novikov, D.S. 2018. What dominates the time dependence of diffusion transverse to axons: Intra- or extra-axonal water? NeuroImage. 182: 500–510.

Lee, H.-H., Novikov, D.S., Fieremans, E. & Huang, S.Y. 2025. Revealing membrane integrity and cell size from diffusion kurtosis time dependence. Magnetic Resonance in Medicine. 93(3): 1329–1347.

Lee, H.-H., Papaioannou, A., Novikov, D.S. & Fieremans, E. 2020. In vivo observation and biophysical interpretation of time-dependent diffusion in human cortical gray matter. NeuroImage. 222: 117054.

Li, C., Fieremans, E., Novikov, D.S., Ge, Y. & Zhang, J. 2023a. Measuring water exchange on a preclinical MRI system using filter exchange and diffusion time dependent kurtosis imaging. Magnetic Resonance in Medicine. 89(4): 1441–1455.

Li, Z., Liang, C., He, Q., Feiweier, T., Hsu, Y.-C., Li, J. & Bai, R. 2025. Comparison of water exchange measurements between filter-exchange imaging and diffusion time-dependent kurtosis imaging in the human brain. Magnetic Resonance in Medicine.

Li, Z., Pang, Z., Cheng, J., Hsu, Y.-C., Sun, Y., Özarslan, E. & Bai, R. 2022. The direction-dependence of apparent water exchange rate in human white matter. NeuroImage. 247: 118831.

Li, B.-Z., Sumera, A., Booker, S.A. & McCullagh, E.A. 2023b. Current Best Practices for Analysis of Dendritic Spine Morphology and Number in Neurodevelopmental Disorder Research. ACS Chemical Neuroscience. 14(9): 1561–1572.

Liewald, D., Miller, R., Logothetis, N., Wagner, H.-J. & Schüz, A. 2014. Distribution of axon diameters in cortical white matter: an electron-microscopic study on three human brains and a macaque. Biological Cybernetics. 108(5): 541–557.

Ludwig, D., Laun, F.B., Ladd, M.E., Bachert, P. & Kuder, T.A. 2021. Apparent exchange rate imaging: On its applicability and the connection to the real exchange rate. Magnetic Resonance in Medicine. 86(2): 677–692.

Lundell, H., Nilsson, M., Dyrby, T.B., Parker, G.J.M., Cristinacce, P.L.H., Zhou, F.-L., Topgaard, D. & Lasič, S. 2019. Multidimensional diffusion MRI with spectrally modulated gradients reveals unprecedented microstructural detail. Scientific Reports. 9(1): 9026.

Mabray, M.C. & Cha, S. 2016. Advanced MR Imaging Techniques in Daily Practice. Neuroimaging Clinics of North America. 26(4): 647–666.

Mattiello, J., Basser, P.J. & Le Bihan, D. 1997. The b matrix in diffusion tensor echo-planar imaging. Magnetic Resonance in Medicine. 37(2): 292–300.

Maugeri, R., Schiera, G., Di Liegro, C.M., Fricano, A., Iacopino, D.G. & Di Liegro, I. 2016. Aquaporins and Brain Tumors. International Journal of Molecular Sciences. 17(7): 1029.

Meerwall, E. von & Ferguson, R.D. 1981. Interpreting pulsed-gradient spin–echo diffusion experiments with permeable membranes. The Journal of Chemical Physics. 74(12): 6956–6959.

Meier, C., Dreher, W. & Leibfritz, D. 2003. Diffusion in compartmental systems. I. A comparison of an analytical model with simulations. Magnetic Resonance in Medicine. 50(3): 500–509.

Mitra, P.P. 1995. Multiple wave-vector extensions of the NMR pulsed-field-gradient spin-echo diffusion measurement. Physical Review B. 51(21): 15074–15078.

Mitra, P.P., Sen, P.N. & Schwartz, L.M. 1993. Short-time behavior of the diffusion coefficient as a geometrical probe of porous media. Physical Review B. 47(14): 8565–8574.

Mitra, P.P., Sen, P.N., Schwartz, L.M. & Le Doussal, P. 1992. Diffusion propagator as a probe of the structure of porous media. Physical Review Letters. 68(24): 3555–3558.

Montgomery, M.K., Kim, S.H., Dovas, A., Zhao, H.T., Goldberg, A.R., Xu, W., Yagielski, A.J., Cambareri, M.K., Patel, K.B., Mela, A., Humala, N., Thibodeaux, D.N., Shaik, M.A., Ma, Y., Grinband, J., Chow, D.S., Schevon, C., Canoll, P. & Hillman, E.M.C. 2020. Glioma-Induced Alterations in Neuronal Activity and Neurovascular Coupling during Disease Progression. Cell Reports. 31(2): 107500.

Mori, S. & Barker, P.B. 1999. Diffusion magnetic resonance imaging: its principle and applications. The Anatomical Record. 257(3): 102–109.

Moseley, M. 2002. Diffusion tensor imaging and aging – a review. NMR in Biomedicine. 15(7–8): 553–560.

Moseley, M.E., Cohen, Y., Kucharczyk, J., Mintorovitch, J., Asgari, H.S., Wendland, M.F., Tsuruda, J. & Norman, D. 1990. Diffusion-weighted MR imaging of anisotropic water diffusion in cat central nervous system. Radiology. 176(2): 439–445.

Mougel, E., Valette, J. & Palombo, M. 2024. Investigating exchange, structural disorder, and restriction in gray matter via water and metabolites diffusivity and kurtosis time-dependence. Imaging Neuroscience. 2: 1–14.

Moutal, N., Nilsson, M., Topgaard, D. & Grebenkov, D. 2018. The Kärger vs bi-exponential model: Theoretical insights and experimental validations. Journal of Magnetic Resonance. 296: 72–78.

Nayak, L. & Reardon, D.A. 2017. High-grade Gliomas. Continuum (Minneapolis, Minn.). 23(6, Neuro-oncology): 1548–1563.

Neuman, C.H. 1974. Spin echo of spins diffusing in a bounded medium. The Journal of Chemical Physics. 60(11): 4508–4511.

Nguyen, T.M., Thomas, L.A., Rhoades, J.L., Ricchi, I., Yuan, X.C., Sheridan, A., Hildebrand, D.G.C., Funke, J., Regehr, W.G. & Lee, W.-C.A. 2021. Structured connectivity in the cerebellum enables noise-resilient pattern separation. 2021.11.29.470455.

Nico, B., Mangieri, D., Tamma, R., Longo, V., Annese, T., Crivellato, E., Pollo, B., Maderna, E., Ribatti, D. & Salmaggi, A. 2009. Aquaporin-4 contributes to the resolution of peritumoural brain oedema in human glioblastoma multiforme after combined chemotherapy and radiotherapy. European Journal of Cancer (Oxford, England: 1990). 45(18): 3315–3325.

Nilsson, M., Alerstam, E., Wirestam, R., Sta˚hlberg, F., Brockstedt, S. & Lätt, J. 2010. Evaluating the accuracy and precision of a two-compartment Kärger model using Monte Carlo simulations. Journal of Magnetic Resonance. 206(1): 59–67.

Nilsson, M., Englund, E., Szczepankiewicz, F., Westen, D. van & Sundgren, P.C. 2018. Imaging brain tumour microstructure. NeuroImage. 182: 232–250.

Nilsson, M., Lasič, S., Drobnjak, I., Topgaard, D. & Westin, C.-F. 2017. Resolution limit of cylinder diameter estimation by diffusion MRI: The impact of gradient waveform and orientation dispersion. NMR in Biomedicine. 30(7): e3711.

Nilsson, M., Lätt, J., Nordh, E., Wirestam, R., Ståhlberg, F. & Brockstedt, S. 2009. On the effects of a varied diffusion time in vivo: is the diffusion in white matter restricted? Magnetic Resonance Imaging. 27(2): 176–187.

Nilsson, M., Lätt, J., Westen, D. van, Brockstedt, S., Lasič, S., Ståhlberg, F. & Topgaard, D. 2013. Noninvasive mapping of water diffusional exchange in the human brain using filter-exchange imaging. Magnetic Resonance in Medicine. 69(6): 1572–1580.

Nilsson, M., Szczepankiewicz, F., Brabec, J., Taylor, M., Westin, C.-F., Golby, A., Westen, D. van & Sundgren, P.C. 2020. Tensor-valued diffusion MRI in under 3 minutes: an initial survey of microscopic anisotropy and tissue heterogeneity in intracranial tumors. Magnetic Resonance in Medicine. 83(2): 608–620.

Ning, L., Gagoski, B., Szczepankiewicz, F., Westin, C.-F. & Rathi, Y. 2020. Joint RElaxation-Diffusion Imaging Moments to Probe Neurite Microstructure. IEEE transactions on medical imaging. 39(3): 668–677.

Ning, L., Nilsson, M., Lasič, S., Westin, C.-F. & Rathi, Y. 2018. Cumulant expansions for measuring water exchange using diffusion MRI. The Journal of Chemical Physics. 148(7): 074109.

Novello, L., Henriques, R.N., Ianuş, A., Feiweier, T., Shemesh, N. & Jovicich, J. 2022. In vivo Correlation Tensor MRI reveals microscopic kurtosis in the human brain on a clinical 3T scanner. NeuroImage. 254: 119137.

Novikov, D.S., Fieremans, E., Jespersen, S.N. & Kiselev, V.G. 2019. Quantifying brain microstructure with diffusion MRI: Theory and parameter estimation. NMR in Biomedicine. 32(4): e3998.

Novikov, D.S., Jensen, J.H., Helpern, J.A. & Fieremans, E. 2014. Revealing mesoscopic structural universality with diffusion. Proceedings of the National Academy of Sciences. 111(14): 5088–5093.

Novikov, D.S., Kiselev, V.G. & Jespersen, S.N. 2018. On modeling. Magnetic Resonance in Medicine. 79(6): 3172–3193.

Ohene, Y., Harris, W.J., Powell, E., Wycech, N.W., Smethers, K.F., Lasič, S., South, K., Coutts, G., Sharp, A., Lawrence, C.B., Boutin, H., Parker, G.J.M., Parkes, L.M. & Dickie, B.R. 2023. Filter exchange imaging with crusher gradient

modelling detects increased blood–brain barrier water permeability in response to mild lung infection. Fluids and Barriers of the CNS. 20: 25.

Olesen, J.L., Østergaard, L., Shemesh, N. & Jespersen, S.N. 2022. Diffusion time dependence, power-law scaling, and exchange in gray matter. NeuroImage. 251: 118976.

Omuro, A. & DeAngelis, L.M. 2013. Glioblastoma and other malignant gliomas: a clinical review. JAMA. 310(17): 1842–1850.

Ostrom, Q.T., Bauchet, L., Davis, F.G., Deltour, I., Fisher, J.L., Langer, C.E., Pekmezci, M., Schwartzbaum, J.A., Turner, M.C., Walsh, K.M., Wrensch, M.R. & Barnholtz-Sloan, J.S. 2014. The epidemiology of glioma in adults: a 'state of the science' review. Neuro-Oncology. 16(7): 896–913.

Özarslan, E. & Basser, P.J. 2008. Microscopic anisotropy revealed by NMR double pulsed field gradient experiments with arbitrary timing parameters. The Journal of Chemical Physics. 128(15): 154511.

Palombo, M., Gallea, C., Genovese, G., Lehericy, S., Branzoli, F. & Şimşek, K. 2020a. Characterizing the fine microstructure of cerebellar and cerebral cortex non-invasively with metabolite diffusion-weighted MRS. Proceedings of the ISMRM.

Palombo, M., Ianus, A., Guerreri, M., Nunes, D., Alexander, D.C., Shemesh, N. & Zhang, H. 2020b. SANDI: A compartment-based model for non-invasive apparent soma and neurite imaging by diffusion MRI. NeuroImage. 215: 116835.

Palombo, M., Ligneul, C., Hernandez-Garzon, E. & Valette, J. 2018. Can we detect the effect of spines and leaflets on the diffusion of brain intracellular metabolites? NeuroImage. 182: 283–293.

Palombo, M. & Şimşek, K. 2024. Towards quantifying Gray Matter "micro-connectivity": the measurable impact of dendritic spines on metabolite diffusion. Proceedings of the ISMRM. Singapore.

Panagiotaki, E., Walker-Samuel, S., Siow, B., Johnson, S.P., Rajkumar, V., Pedley, R.B., Lythgoe, M.F. & Alexander, D.C. 2014. Noninvasive Quantification of Solid Tumor Microstructure Using VERDICT MRI. Cancer Research. 74(7): 1902–1912.

Papadopoulos, M.C. & Verkman, A.S. 2013. Aquaporin water channels in the nervous system. Nature Reviews. Neuroscience. 14(4): 265–277.

Penzes, P., Cahill, M.E., Jones, K.A., VanLeeuwen, J.-E. & Woolfrey, K.M. 2011. Dendritic spine pathology in neuropsychiatric disorders. Nature Neuroscience. 14(3): 285–293.

Perge, J.A., Koch, K., Miller, R., Sterling, P. & Balasubramanian, V. 2009. How the optic nerve allocates space, energy capacity, and information. The Journal of Neuroscience: The Official Journal of the Society for Neuroscience. 29(24): 7917–7928.

Pfeuffer, J., Flögel, U., Dreher, W. & Leibfritz, D. 1998. Restricted diffusion and exchange of intracellular water: theoretical modelling and diffusion time dependence of 1H NMR measurements on perfused glial cells. NMR in Biomedicine. 11(1): 19–31.

Phillips, R., Kondev, J., Theriot, J. & Garcia, H.G. 2012. *Physical Biology of the Cell*. New York: Garland Science.

Powell, E., Ohene, Y., Battiston, M., Dickie, B.R., Parkes, L.M. & Parker, G.J.M. 2023. Blood-brain barrier water exchange measurements using FEXI: Impact of modeling paradigm and relaxation time effects. Magnetic Resonance in Medicine. 90(1): 34–50.

Preston, G.M., Carroll, T.P., Guggino, W.B. & Agre, P. 1992. Appearance of water channels in Xenopus oocytes expressing red cell CHIP28 protein. Science (New York, N.Y.). 256(5055): 385–387.

Price, W.S. 1997. Pulsed-field gradient nuclear magnetic resonance as a tool for studying translational diffusion: Part 1. Basic theory. Concepts in Magnetic Resonance. 9(5): 299–336.

Price, W.S. 2009. *NMR Studies of Translational Motion: Principles and Applications*. Cambridge: Cambridge University Press.

Price, W.S., Barzykin, A.V., Hayamizu, K. & Tachiya, M. 1998. A Model for Diffusive Transport through a Spherical Interface Probed by Pulsed-Field Gradient NMR. Biophysical Journal. 74(5): 2259–2271.

Purves, D., Augustine, G.J., Fitzpatrick, D., Katz, L.C., LaMantia, A.-S., McNamara, J.O. & Williams, S.M. 2001. Neuroglial Cells. Neuroscience. 2nd edition. Sinauer Associates.

Raab, P., Hattingen, E., Franz, K., Zanella, F.E. & Lanfermann, H. 2010. Cerebral Gliomas: Diffusional Kurtosis Imaging Analysis of Microstructural Differences. Radiology. 254(3): 876–881.

Reuss, L. 2012. Water Transport Across Cell Membranes. eLS. John Wiley & Sons, Ltd.

Reynaud, O. 2017. Time-Dependent Diffusion MRI in Cancer: Tissue Modeling and Applications. Frontiers in Physics. 5: 58.

Reynaud, O., Winters, K.V., Hoang, D.M., Wadghiri, Y.Z., Novikov, D.S. & Kim, S.G. 2016. Pulsed and oscillating gradient MRI for assessment of cell size and Extracellular space (POMACE) in mouse gliomas. NMR in biomedicine. 29(10): 1350–1363.

Romano, A., D'Andrea, G., Minniti, G., Mastronardi, L., Ferrante, L., Fantozzi, L.M. & Bozzao, A. 2009. Pre-surgical planning and MR-tractography utility in brain tumour resection. European Radiology. 19(12): 2798–2808.

Runge, K., Cardoso, C. & Chevigny, A. de. 2020. Dendritic Spine Plasticity: Function and Mechanisms. Frontiers in Synaptic Neuroscience. 12.

Sagi, Y., Tavor, I., Hofstetter, S., Tzur-Moryosef, S., Blumenfeld-Katzir, T. & Assaf, Y. 2012. Learning in the fast lane: new insights into neuroplasticity. Neuron. 73(6): 1195–1203.

Scholz, J., Klein, M.C., Behrens, T.E.J. & Johansen-Berg, H. 2009. Training induces changes in white-matter architecture. Nature Neuroscience. 12(11): 1370–1371.

Scott, J.N., Brasher, P.M.A., Sevick, R.J., Rewcastle, N.B. & Forsyth, P.A. 2002. How often are nonenhancing supratentorial gliomas malignant? A population study. Neurology. 59(6): 947–949.

Sen, P.N. 2004. Time-dependent diffusion coefficient as a probe of geometry. Concepts in Magnetic Resonance Part A. 23A(1): 1–21.

Setsompop, K., Kimmlingen, R., Eberlein, E., Witzel, T., Cohen-Adad, J., McNab, J.A., Keil, B., Tisdall, M.D., Hoecht, P., Dietz, P., Cauley, S.F., Tountcheva, V., Matschl, V., Lenz, V.H., Heberlein, K., Potthast, A., Thein, H., Van Horn, J., Toga, A., Schmitt, F., Lehne, D., Rosen, B.R., Wedeen, V. & Wald, L.L. 2013. Pushing the limits of in vivo diffusion MRI for the Human Connectome Project. NeuroImage. 80: 220–233.

Shemesh, N., Jespersen, S.N., Alexander, D.C., Cohen, Y., Drobnjak, I., Dyrby, T.B., Finsterbusch, J., Koch, M.A., Kuder, T., Laun, F., Lawrenz, M., Lundell, H., Mitra, P.P., Nilsson, M., Özarslan, E., Topgaard, D. & Westin, C.-F. 2016. Conventions and nomenclature for double diffusion encoding NMR and MRI. Magnetic Resonance in Medicine. 75(1): 82–87.

Shemesh, N., Özarslan, E., Komlosh, M.E., Basser, P.J. & Cohen, Y. 2010. Gleaning new microstructural information from double-PFG NMR and MRI. NMR in biomedicine. 23(7): 757–780.

Shin, H.-G., Li, X., Heo, H.-Y., Knutsson, L., Szczepankiewicz, F., Nilsson, M. & Zijl, P.C.M. van. 2024. Compartmental anisotropy of filtered exchange imaging (FEXI) in human white matter: What is happening in FEXI? Magnetic Resonance in Medicine. 92(2): 660–675.

Şimşek, K. & Palombo, M. 2024. Diffusion in dendritic spines: impact on permeative exchange estimation with time-dependent diffusion-weighted MRI. Proceedings of the ISMRM. Singapore.

Sønderby, C.K., Lundell, H.M., Søgaard, L.V. & Dyrby, T.B. 2014. Apparent exchange rate imaging in anisotropic systems. Magnetic Resonance in Medicine. 72(3): 756–762.

Sotak, C.H. 2002. The role of diffusion tensor imaging in the evaluation of ischemic brain injury - a review. NMR in biomedicine. 15(7–8): 561–569.

Stanisz, G.J., Wright, G.A., Henkelman, R.M. & Szafer, A. 1997. An analytical model of restricted diffusion in bovine optic nerve. Magnetic Resonance in Medicine. 37(1): 103–111.

Stejskal, E.O. & Tanner, J.E. 1965. Spin Diffusion Measurements: Spin Echoes in the Presence of a Time-Dependent Field Gradient. The Journal of Chemical Physics. 42(1): 288–292.

Stepišnik, J. 1993. Time-dependent self-diffusion by NMR spin-echo. Physica B: Condensed Matter. 183(4): 343–350.

Sun, D.-P., Lee, Y.-W., Chen, J.-T., Lin, Y.-W. & Chen, R.-M. 2020. The Bradykinin-BDKRB1 Axis Regulates Aquaporin 4 Gene Expression and Consequential Migration and Invasion of Malignant Glioblastoma Cells via a Ca2+-MEK1-ERK1/2-NF-κB Mechanism. Cancers. 12(3): 667.

Sundgren, P.C., Dong, Q., Gómez-Hassan, D., Mukherji, S.K., Maly, P. & Welsh, R. 2004. Diffusion tensor imaging of the brain: review of clinical applications. Neuroradiology. 46(5): 339–350.

Szczepankiewicz, F., Sjölund, J., Dall'Armellina, E., Plein, S., Schneider, J.E., Teh, I. & Westin, C.-F. 2021a. Motion-compensated gradient waveforms for tensor-valued diffusion encoding by constrained numerical optimization. Magnetic Resonance in Medicine. 85(4): 2117–2126.

Szczepankiewicz, F., Westen, D. van, Englund, E., Westin, C.-F., Ståhlberg, F., Lätt, J., Sundgren, P.C. & Nilsson, M. 2016. The link between diffusion MRI and tumor heterogeneity: Mapping cell eccentricity and density by diffusional variance decomposition (DIVIDE). NeuroImage. 142: 522–532.

Szczepankiewicz, F., Westin, C.-F. & Nilsson, M. 2021b. Gradient waveform design for tensor-valued encoding in diffusion MRI. Journal of Neuroscience Methods. 348: 109007.

Tanner, J.E. 1978. Transient diffusion in a system partitioned by permeable barriers. Application to NMR measurements with a pulsed field gradient. The Journal of Chemical Physics. 69(4): 1748–1754.

Tax, C.M.W., Szczepankiewicz, F., Nilsson, M. & Jones, D.K. 2020. The dot-compartment revealed? Diffusion MRI with ultra-strong gradients and spherical tensor encoding in the living human brain. NeuroImage. 210: 116534.

Topgaard, D. 2025. Validity of the Gaussian phase distribution approximation for analysis of isotropic diffusion encoding applied to restricted diffusion in a cylinder. Magnetic Resonance Letters.: 200196.

Torrey, H.C. 1956. Bloch Equations with Diffusion Terms. Physical Review. 104(3): 563–565.

Trapp, B.D. & Kidd, G.J. 2004. Chapter 1 - Structure of the Myelinated Axon. Myelin Biology and Disorders, 3–27. San Diego: Academic Press.

Uhl, Q., Pavan, T., Molendowska, M., Jones, D.K., Palombo, M. & Jelescu, I.O. 2024. Quantifying human gray matter microstructure using neurite exchange imaging (NEXI) and 300 mT/m gradients. Imaging Neuroscience. 2: 1–19.

Van Cauter, S., Veraart, J., Sijbers, J., Peeters, R.R., Himmelreich, U., De Keyzer, F., Van Gool, S.W., Van Calenbergh, F., De Vleeschouwer, S., Van Hecke, W. & Sunaert, S. 2012. Gliomas: Diffusion Kurtosis MR Imaging in Grading. Radiology. 263(2): 492–501.

Veraart, J., Fieremans, E. & Novikov, D.S. 2019. On the scaling behavior of water diffusion in human brain white matter. NeuroImage. 185: 379–387.

Veraart, J., Nunes, D., Rudrapatna, U., Fieremans, E., Jones, D.K., Novikov, D.S. & Shemesh, N. 2020. Noninvasive quantification of axon radii using diffusion MRI. eLife. 9: e49855.

Verkman, A.S., Hara-Chikuma, M. & Papadopoulos, M.C. 2008. Aquaporins--new players in cancer biology. Journal of Molecular Medicine (Berlin, Germany). 86(5): 523–529.

Voogd, J. & Glickstein, M. 1998. The anatomy of the cerebellum. Trends in Neurosciences. 21(9): 370–375.

Warth, A., Mittelbronn, M. & Wolburg, H. 2005. Redistribution of the water channel protein aquaporin-4 and the K+ channel protein Kir4.1 differs in low- and high-grade human brain tumors. Acta Neuropathologica. 109(4): 418–426.

Westin, C.-F., Knutsson, H., Pasternak, O., Szczepankiewicz, F., Özarslan, E., Westen, D. van, Mattisson, C., Bogren, M., O'Donnell, L.J., Kubicki, M., Topgaard, D. & Nilsson, M. 2016. Q-space trajectory imaging for multidimensional diffusion MRI of the human brain. NeuroImage. 135: 345–362.

Westin, C.-F., Szczepankiewicz, F., Pasternak, O., Özarslan, E., Topgaard, D., Knutsson, H. & Nilsson, M. 2014. Measurement Tensors in Diffusion MRI: Generalizing the Concept of Diffusion Encoding. Medical Image Computing and Computer-Assisted Intervention – MICCAI 2014, 209–216. Cham: Springer International Publishing.

Williamson, N.H., Ravin, R., Cai, T.X., Benjamini, D., Falgairolle, M., O'Donovan, M.J. & Basser, P.J. 2020. Real-time measurement of diffusion exchange rate in biological tissue. Journal of magnetic resonance (San Diego, Calif. : 1997). 317: 106782.

Wu, X., He, Q., Yin, Y., Tan, S., Zhang, B., Li, W., Hsu, Y.-C., Xue, R. & Bai, R. 2024. Relaxation-exchange magnetic resonance imaging (REXI): a non-invasive imaging method for evaluating trans-barrier water exchange in the choroid plexus. Fluids and Barriers of the CNS. 21: 94.

Yablonskiy, D.A. & Sukstanskii, A.L. 2010. Theoretical models of the diffusion weighted MR signal. NMR in Biomedicine. 23(7): 661–681.

Yang, D.M., Huettner, J.E., Bretthorst, G.L., Neil, J.J., Garbow, J.R. & Ackerman, J.J.H. 2018. Intracellular water preexchange lifetime in neurons and astrocytes. Magnetic Resonance in Medicine. 79(3): 1616–1627.

Zhang, J., Lemberskiy, G., Moy, L., Fieremans, E., Novikov, D.S. & Kim, S.G. 2021. Measurement of cellular-interstitial water exchange time in tumors based on diffusion-time-dependent diffusional kurtosis imaging. NMR in biomedicine. 34(6): e4496.

Zhang, Y., Wang, Y., Li, Z., Wang, Z., Cheng, J., Bai, X., Hsu, Y.-C., Sun, Y., Li, S., Shi, J., Sui, B. & Bai, R. 2023. Vascular-water-exchange MRI (VEXI) enables the detection of subtle AXR alterations in Alzheimer's disease without MRI contrast agent, which may relate to BBB integrity. NeuroImage. 270: 119951.